SURFACE PROCESSING OF NANOPOROUS LOW DIELECTRIC CONSTANT THIN FILMS

LIU JUN

NATIONAL UNIVERSITY OF SINGAPORE

2004

SURFACE PROCESSING OF NANOPOROUS LOW DIELECTRIC CONSTANT THIN FILMS

LIU JUN

(B.Sci., Peking University)

A THESIS SUBMITTED

FOR THE DEGREE OF MASTER OF SCIENCE

DEPARTMENT OF CHEMISTRY

INSITUTE OF MATERIALS RESEARCH AND ENGINEERING

NATIONAL UNIVERSITY OF SINGAPORE

2004

To my parents Chaobei Liu and Hanling Wu

ACKNOWLEDGMENT

I would like to express my sincere gratitude to my supervisors, Dr. Kian Ping Loh and Dr. Dongzhi Chi, whose expertise, guidance, and faith in my abilities provided full support throughout the course of this research. I am also grateful to our research team members Weide Wang and Lei Wang for their important contributions to this thesis work.

I am also very thankful to Mei Ying (Doreen) Lai, Siew Lang Teo, Sue Yin Chow and Chow Khim Tan for their consistent help in the experimental works. Special thanks go to Professor David W. Gidley and Professor Albert F. Yee for their help in performing PALS tests and analyzing the results on pore-sealing efficiency.

I am grateful for the financial support provided by the Institute of Materials Research and Engineering (IMRE), the Agency for Science, Technology and Research (ASTAR), as well as the Department of Chemistry at the National University of Singapore.

Last, but far from least, I am indebted to my parents Chaobei Liu, Hanling Wu, my girlfriend, other family members and lifelong friends, who gave me their continuous understanding and support throughout the course of my school years.

TABLE OF CONTENTS

DEDICATION ••**ii**

ACKNOWLEDGMENT••**iii**

LIST OF FIGURES ••**vii**

LIST OF TABLES ••**xi**

ABSTRACT••**xii**

CHAPTER

1. MOTIVATION AND OBJECTIVES……..…………………...1

1.1. Overview…………………………………………………………...1

1.2. Nanoporous Low-*k* Thin films………………………………………5

1.2.1 Promising porous low-*k* materials

1.2.2 Classification and Properties of porous low-*k* thin films

1.2.3 Fabrication of porous low-*k* films

1.2.4 Characterization of pore-sealing on porous low-*k* films

1.3. Multilevel Metallization for Integrated Circuits……………………..16

1.4. Porous Low-*k* Materials Damascene Integration Process…………...21

1.4.1 Single-Damascene Integration Process

1.4.2 Dual-Damascene Integration Process

1.4.3 Porous low-*k* materials Damascene Integration Issues

1.5. Thesis Objectives……..……..……..23

2. EXPERIMENTAL SECTION……...26

2.1. Surface Plasma Treatment……..26

2.2. Dielectric Films Trench Patterning……....27

2.3. BN Thin Film Deposition……....29

2.4. Characterization Techniques…….30

2.4.1 Chemical Composition Characterization

2.4.2 Morphology Measurement

2.4.3 Electrical Characterization

2.4.4 Positron Annihilation Lifetime Spectroscopy (PALS)

3. ZIRKON LK2200 FILMS PORE-SEALING BY NH_3 PLASMA TREATMENT……...……47

3.1. Introduction…….……..47

3.2. Experimental Section……48

3.3. Results and Discussion……..49

3.3.1 Pore-sealing efficiency of NH_3 plasma treatment

3.3.2 Chemical composition characterization

3.3.3 Morphology characterization

3.3.4 Beneficial effect against Cu diffusion

3.3.5 Zirkon LK2200 Film Trench Patterning

3.4. Conclusion…….……..63

4. FORMING IN-SITU COPPER DIFFUSION BARRIER BY NH_3 PLASMA TREATMENT ON LKD……64

4.1. Introduction……64

4.2. Experimental Section…….65

4.3. Results and Discussion……...67

4.3.1 Thermal stability of LKD5109

4.3.2 Characterization of the LKD chemical structure after plasma treatment

4.3.3 Relative dielectric constant measurement

4.3.4 Evaluation of barrier performance of the plasma modified surface layer against Cu diffusion

4.3.5 PALS characterization

4.4. Conclusion……...……87

5. EVALUATION of PECVD DEPOSITED BORON NITRIDE as Cu DIFFUSION BARRIER on POROUS LOW-*k* MATERIALS……89

5.1. Introduction……..…….....89

5.2. Experimental Section……..……...90

5.3. Results and Discussion……..……...……..93

5.3.1 Structural and compositional characterization

5.3.2 Electrical Measurement

5.3.3 Barrier performance against Cu diffusion

5.3.4 BN trench patterning

5.4. Conclusion…….105

6. CONCLUSION and FUTURE WORK…….106

LIST OF FIGURES

Figures

Figure 1.1 Via-first dual damascene processing steps----------3

Figure 1.2 Structure of elementary units of SSQ dielectric materials----------7

Figure 1.3 Ladder structure of Hydrogen silsesquioxane ----------8

Figure 1.4 Cage structure of Hydrogen silsesquioxane----------8

Figure 1.5 Ladder structure of Methyl silsesquioxane----------9

Figure 1.6 Fabrication Process of Porous LKD low-*k* film----------10

Figure 1.7 An example of porous low-*k* film fabrication through burning out a thermally labile component in a composite film----------14

Figure 1.8 Positronium behavior in porous films----------16

Figure 1.9 Interconnect fabrication approaches----------20

Figure 1.10 Trench-first dual-damascene integration process----------23

Figure 2.1 Mask Pattern for Photolithography----------28

Figure 2.2 MIS structure for SIMS experimental demonstration of barrier performance----------32

Figure 2.3 Process steps of preparing samples for TEM characterization----------33

Figure 2.4 Circuit models for MIS device in accumulation and admittance by a C-V measurement----------35

Figure 2.5 nMOS Metal-Oxide-Semiconductor capacitor----------36

Figure 2.6 Interface charge in accumulation, depletion and inversion status----------37

Figure 2.7 Metal/insulator/semiconductor structure for BN/LKD stack C-V measurement----------38

Figure 2.8 Metal-insulator-semiconductor structure for LKD C-V measurement-----39

Figure 2.9 Metal-insulator-semiconductor structure for I-V measurement----------39

Figure 2.10 Positron and Ps interactions with condensed matter----------41

Figure 2.11 Schematic of the Depth-Profiled Positron Spectrometer: System I designed for good timing resolution----------44

Figure 2.12 Schematic of the new slow positron beam: System II designed for high rate of events----------45

Figure 3.1 Ps vacuum intensity in the PT films. A pair of unprocessed porous and Si-capped porous films is examined for comparison----------52

Figure 3.2 Carbon depth profile of non-processed and PT low-*k* samples----------53

Figure 3.3 CN depth profile of non-processed and PT low-*k* samples----------53

Figure 3.4 FTIR spectrums of Zirkon 2200 after different PT processes----------54

Figure 3.5 FTIR Peak area ratio of I_{Si-O}/I_{Si-CH3} of Zirkon films after different plasma treatments----------55

Figure 3.6 Raman spectroscopy of non-processed and plasma treated low-*k* films---56

Figure 3.7 AFM of unprocessed and PT processed Zirkon low-*k* films----------57

Figure 3.8 Cross-sectional TEM figures of processed Zirkon films----------59

Figure 3.9 Proposed mechanism of Plasma treatment on the porous low-*k* film------60

Figure 3.10 SIMS depth profile of Cu/MSQ/Si stack after 1 hour thermal annealing at 400^{o}C in N_2 ambient----------61

Figure 3.11 Cross-section SEM of the Zirkon film after RIE etching----------62

Figure 3.12 SEM of the MSQ surface after Etching----------63

Figure 4.1 FTIR spectrum of LKD film after one hour thermal stress at 300^{o}C, 400^{o}C, 500^{o}C and 600^{o}C----------68

Figure 4.2 FTIR peak area ratio of Si-O-Si stretching peak to Si-CH_3 stretching peak after thermal stress----------69

Figure 4.3 Relative dielectric constant of LKD before and after 1 hour thermal stressing----------70

Figure 4.4 FTIR spectra for as-cured LKD film, 3s NH_3 plasma treated LKD film, 10s NH_3 plasma treated LKD film, 30s NH_3 plasma treated LKD film and 60s NH_3 plasma treated film----------71

Figure 4.5 Raman spectrums of as-received LKD and LKD after different time NH_3 plasma treatment----------72

Figure 4.6 Si-C/Si-O peak ratios obtained from a series of FTIR spectra for as-cured LKD films receiving various time of plasma treatment. C-H/Si-O peak ratios obtained from a series of Raman spectra for as-cured LKD films after different time NH_3 plasma treatment. Note that the $I_{Si-C/Si-O}$ and $I_{C-H/Si-O}$ for as-cured films prior to any plasma treatments are used as standard and set at 1----------73

Figure 4.7 SIMS depth profiles of LKD films: (a) As-received LKD5109, (b) LKD after 30s NH_3 plasma treatment and (c) LKD after 60s NH3 plasma treatment-------75

Figure 4.8 XPS spectra of N1s with and without NH_3 plasma treatment on LKD films ----------76

Figure 4.9 Capacitance-voltage curves of thermal SiO_2 for C-V measurement system calibration----------77

Figure 4.10 C-V curves of LKD thin films before and after plasma treatment--------79

Figure 4.11 Relative dielectric constant of as-cured LKD film and LKD films receiving various time of plasma treatment----------80

Fig 4.12 Leakage current density-voltage curves of Cu/LKD film/Si structure without thermal annealing, (a) to (e) representing the I-V curve of LKD as, PT 3s, PT 10s, PT 30s and PT 60s LKD, respectively----------81

Fig 4.13 Leakage current density-voltage curves of Cu/LKD film/Si structure after 1 hour thermal annealing at 400^{o}C----------82

Figure 4.14 Secondary ion mass spectroscopy for as-cured LKD and LKD film after 60s plasma treatment with Cu-electrode after being subjected to thermal stress at 400^{o}C for 1 hour----------83

Figure 4.15 Ps mesopre lifetime vs. Ps implant energy in as-received and plasma treated LKD films----------85

Figure 4.16 Ps Vacuum signal intensity vs. Ps implant energy in as-received and plasma treated LKD films----------86

Figure 4.17 Fraction of densified pores as a function of positron implantation depth using energies of 1, 3 and 5 keV----------87

Figure 5.1 Metal-Insulator-Semiconductor structure for C-V measurement----------78

Figure 5.2 Raman spectrum of as-received LKD film and the low-k film after microwave CVD BN deposited on it at 400^{o}C----------80

Figure 5.3 FTIR spectrum of as-received LKD, microwave plasma CVD deposited BN on low-*k* film and RF plasma deposited BN on low-k material at 400^{o}C----------81

Figure 5.4 SIMS depth profile of as-received LKD film----------82

Figure 5.5 SIMS depth profile of microwave plasma CVD deposited BN on LKD film at 400^{o}C----------83

Figure 5.6 SIMS depth profile of RF plasma CVD deposited BN on LKD film at 400^{o}C----------84

Figure 5.7 *Left:* C-V curve of MPCVD BN on Si. *Right:* Relative dielectric constants: a. MPCVD deposited BN on p type Si (100), b. MPCVD deposited BN on LKD film and c. RF-CVD deposited BN on LKD film----------86

Figure 5.8 SIMS depth profile of Cu/MPCVD-BN/LKD/Si structure annealing at 400^{o}C in N_2 ambient for 1 hour----------87

Figure 5.9 XSEM of MPCVD deposited BN on LKD at 400^{o}C----------87

Figure 5.10 Microscope image of the surface after photo resist development---------88

Figure 5.11 XSEM of photo resist developed on BN film----------89

Figure 5.12 Low-Magnification XSEM of patterned BN film after photo resist stripping and residue cleaning----------90

Figure 5.13 High-magnification XSEM of patterned BN film after photo resist stripping and residue cleaning----------90

LIST OF TABLES

Tables

Table 1.1 Characteristic numbers for future technology nodes relating to dimensions and material characteristics from ITRS 2002 roadmap (MPU Interconnect Technology-Near-term) ----------2

Table 3.1 PALS characterization of Zirkon LK2200 films with and without Si-capping----------50

Table 3.2 PALS characterization of Zirkon LK2200 films after different time plasma treatment----------51

Table 4.1 PALS Results for as-received 400 nm-thick LKD without PT process-----84

ABSTRACT

In this work, several kinds of surface processing have been carried out on MSQ-based porous low-*k* films in resolving some key issues in the low-*k* materials and copper damascene integration. Nanoporous low-*k* films were treated by using low frequency NH_3 plasma in order to form a surface densified layer, which can effectively seal the porous films. The plasma treatment process has been optimized and applied for two kinds of low-*k* films. Both the sealing efficiency and the barrier performance against Cu diffusion have been evaluated after the plasma treatment.

Hexagonal Boron Nitride (*h*-BN) films have also been deposited on porous low-*k* film to develop a new type of low-*k* dielectric barrier against Cu diffusion. Both Microwave Plasma CVD (2.45 GHz) and Radio-frequency plasma atom beam deposition (13.56 MHz) were applied for the *h*-BN deposition in order to evaluate the compatibility of the two plasma processes with the nanoporous films.

Keywords:

Low-*k*, **Porosity**, **Plasma treatment**, **Densified layer**, **Diffusion Barrier** and **BN**.

CHAPTER 1

MOTIVATION AND OBJECTIVES

1.1. Overview

Since 1970, the Integrated Circuits (ICs) have doubled their speed every 18 months on average as predicted by Moore's law [Moore, 1965]. This has been achieved by the continuous efforts in device miniaturization [1]. As the integrated circuits scaled down to sub-100nm level, the impact of RC delay (wire resistance R and capacitance C) will undoubtedly increase. For a certain feature size, the RC signal delay is determined by interconnect metals and dielectrics. Compared to the previous generation Al/SiO_2 interconnects technology, Cu has become the current metallization material of choice due to its lower resistance. The low resistance of copper has to be allied to low relative dielectric constant (k) material for the overall reduction of RC signal delay. Power consumption is the other major concern for IC interconnections because of the ever increasing frequencies and higher densities. Low-k dielectrics will significantly lower the dynamic power dissipation [2].

TABLE 1.1 Characteristic numbers for future technology nodes relating to dimensions and material characteristics from ITRS 2002 roadmap (MPU Interconnect Technology Near-term).

Year of Production	2001	2002	2003	2004	2005	2006	2007
DRAM 1/2 Pitch (nm)	130	115	100	90	80	70	65
MPU/ASIC 1/2 Pitch (nm)	150	130	107	90	80	70	65
MPU Printed Gate Length (nm)	90	75	65	53	45	40	35
MPU Physical Gate Length (nm)	65	53	45	37	32	28	25
Local Wiring A/R (for Cu)	1.6	1.6	1.6	1.7	1.7	1.7	1.7
Interconnect RC delay 1mm line (ps)	86	121	176	198	256	303	342
Line length where τ= RC delay (um)	137	106	80	70	57	50	44
Intermediate wiring dual Damascene A/R	1.6/1.4	1.6/1.4	1.7/1.5	1.7/1.5	1.7/1.5	1.7/1.6	1.8/1.6
Interconnect RC delay 1mm line (ps)	53	75	101	127	155	191	198
Line length where τ= RC delay (um)	174	135	106	88	73	63	58
Global wiring dual Damascene A/R	2.0/1.8	2.0/1.8	2.1/1.9	2.1/1.9	2.2/2.0	2.2/2.0	2.2/2.0
Interconnect RC delay 1mm line (ps)	21	29	40	47	59	74	79
Line length where τ= RC delay (um)	280	216	168	163	118	100	92
IMD-effective *k* value	3.0-3.6	3.0-3.6	3.0-3.6	2.6-3.1	2.6-3.1	2.6-3.1	2.3-2.7
IMD-bulk *k* value	<2.7	<2.7	<2.7	<2.4	<2.4	<2.4	<2.1

Table 1.1 is an overview of the expected progress for technology nodes over the coming years based on the *International Technology Roadmap for Semiconductors* (ITRS) of 2002 [3]. At the 65nm node, the bulk *k* value of interconnect dielectrics is required to be lower than 2.1, as shown in Table 1.1. Referring to the Clausius-Mossotti equation: $\frac{\varepsilon_r - 1}{\varepsilon_r + 2} = \frac{1}{3\varepsilon_0} N_e \alpha_e$ (1), where ε_r = the relative permittivity at low frequencies, α_e = the electronic polarizability and N_e = the number of ions (or atoms) per unit volume exhibiting electronic polarization, *k* value is determined by molecular polarizability and the number of molecules per unit volume (film density) [2]. Since the possibility to lower molecular polarizability is limited, reducing the film density becomes an important way to develop ultra low-*k* (*k* less

than 2.2) inter metal dielectrics. Technologically, introducing pores into dielectrics has become the dominant strategy for future generation porous low-*k* materials. However, there will be many serious integration issues due to the low-density, porous nature of the ultra low dielectric constant films. For instance, porous films are not as hard, with implication for CMP and wire bonding [4, Laura Peters]. Cu may quite readily diffuse into the porous low-*k* films when integrated directly with the porous low-*k* materials in the back-end process. In addition, in a via-first integration scheme which is shown in figure 1.1, photo resist and other reactive chemicals need to be prevented from penetrating the sidewall of the via, during the trench etch in a porous low-*k* film [4]. Generally porous low-*k* dielectrics need to be sealed before further treatment so as to avoid the problems throughout back-end processing [2].

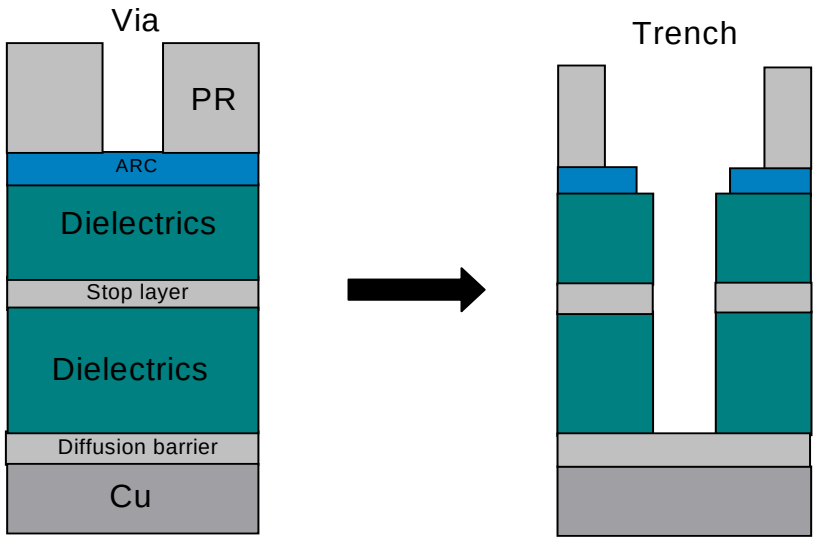

1. Via etch to diffusion barrier – SiN or SiC
2. Resist strip
3. ARC and trench lithography
4. Trench etch stop to middle stop layer
5. Resist strip
6. Nitride or carbide etch
7. Post-etch clean

Figure 1.1. Via-first dual damascene processing steps

In a more general sense, understanding of the sealing mechanisms and ability in sealing the pores is fundamental to the effective integration of porous dielectrics in the interconnect processing [6]. Currently, there are three methods for surface pores sealing: by bombarding low-*k* films with plasma; by oxidizing the surface to create Si-O-Si bonds; or by chemically polymerizing the film, producing cross-linked C-C bonds [5].

In this research, we explore three themes that are relevant to the processing and integration of nanoporous low-k materials:

(I) Controlled low-frequency plasma treatment is employed in forming a non-porous skin layer to seal the pores on the film surface. Because the dielectric properties of the ultra low-*k* films might be modified after the processing [4], the chemical structure and electrical performance of the low-*k* materials are evaluated systematically after certain plasma treatment.

(II) The formation of a non-porous skin layer on the nanoporous films by plasma treatment for blocking Cu diffusion is demonstrated in the second study. Referring to *ITRS* 2002, k_{eff} of the dielectric stack is the key to interconnection performance, the *k* values of hard masks and etch stop layers can be more critical than that of k_{ILD}.

(III) Finally, we evaluate the growth of hexagonal BN as a copper diffusion barrier on the nanoporous films. Previously, Sugino reported [7, Takashi Sugino] the excellent low-*k* properties (*k*~2.4) of amorphous BN (BCN) film grown by simple quartz furnace CVD using BCl_3 as one of the precursors. In this work we study the growth of hexagonal BN films from plasma-discharged borazine, using both

Radio-frequency and Microwave Plasmas, and evaluate the integration and processibility issues of the plasma processes with the nanoporous films. Process conditions which are required to deliver a lower overall k_{eff} stack have been identified.

1.2. Nanoporous Low-*k* Thin Films

1.2.1. Promising porous low-*k* materials

In recent years, the chemical industry has been actively engaged in bringing new materials to the market with ever deceasing *k* values in order to comply with the performance specifications provided by the microelectronics industry technology roadmap. However, so far a low dielectric constant material that can meet the processing requirements of the damascene process remains elusive. The candidate materials must possess, besides desirable properties such as low *k* value, also high thermal and mechanical stability, good adhesion to other interconnect materials, resistance to processing materials, low moisture absorption, and low cost [8]. One difficult issue has been to identify a single material which exhibits the combination of low *k* value and good thermal and mechanical stability. There is a tradeoff between low dielectric constant and high bond strength, which usually leads to good thermal-mechanical properties [9]. In general, materials with strong bonds and a high density of such bonds tend to be structurally stable. However, the strong bonds are usually very polarizable, and the material polarizability increases with the polarizable

bond density [10]. For example, the mechanical and thermal stability of SiO_2 is partly due to its dense (~2.2g/cm^3) network structure. Unfortunately, such high bond and material density in SiO_2 leads to a large molecular polarizability, and therefore leads to a high dielectric constant of 4.0 (thermal SiO_2). Organic polymeric materials often have a lower dielectric constant (2.5 to 3.5) due to the lower material density (~1.0g/cm^3) and lower individual bond polarizabilities. However, most organic materials are soft and cannot stand high thermal stressing.

As the feature size in integrated circuits shrinks to sub-100nm scale, an *ultra* low-*k* material (k<2.2) is required. Since it is difficult to achieve such a low dielectric constant in dense materials, the dominant approach is to lower material density by incorporating micropores and/or meso- into a material network. *Micropores* have diameters smaller than 2 nm, while *mesopores* have diameters between 2 and 50nm [11]. In principle, one can tune the dielectric constant by varying the film porosity. The development of porous dielectrics will substantially reduce the dielectric constant but it must have the desired thermal and mechanical properties required for the rigorous manufacturing environment.

1. 2. 2. Classification and Properties of Porous low-*k* thin films

According to their basic composition, structure and fabrication techniques, porous low-*k* films are classified into three different groups: silsesquioxane (SSQ) based porous thin films; silica based porous low-*k* materials and organic polymers.

Spin-on Silsesquioxane (SSQ) based thin films

Silsesquioxane is the elementary unit of SSQ based low-*k* materials, which are organic-inorganic polymers with the empirical formula $(R–SiO_{3/2})_n$. The most common representatives of SSQ are a ladder-type structure, and a cage structure that contains eight silicon atoms placed at the vertices of a cube (Fig. 1.2) [2]. The cage-structure is not very stable and can be decomposed to the more stable silica network. Substituents (R) on silicon can include hydrogen, alkyl, alkenyl, alkoxy, and aryl. Many silsesquioxanes have reasonable solubility in common organic solvents because of that organic substitution on Si. The organic substitutes also provide low density and low dielectric constant material, the lower *k* value of which is attributed to the low polarizability of the Si–R bond as compared to the Si–O bond in SiO_2.

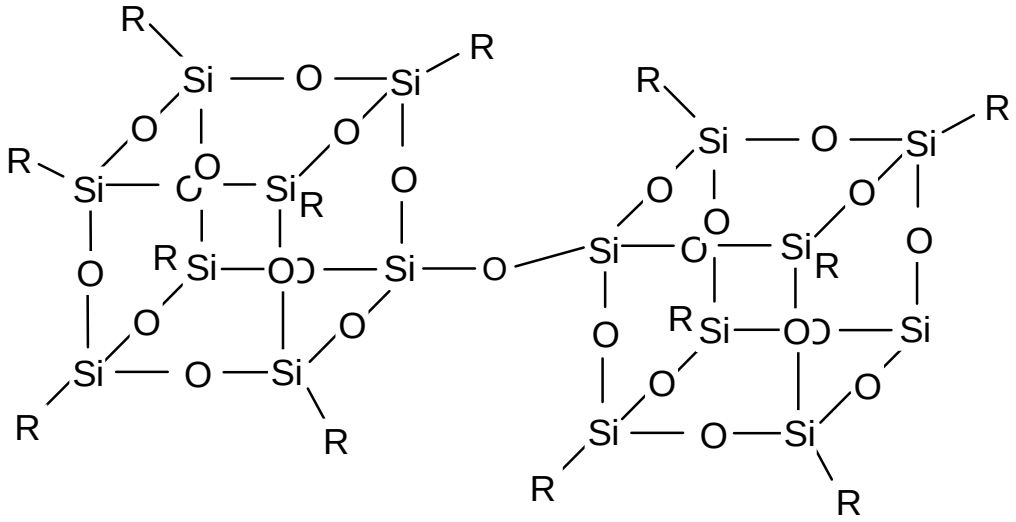

Figure 1.2. Structure of elementary units of SSQ dielectric materials

The silsesquioxane based materials for integrated circuits application are mainly hydrogen-silsesquioxane (HSQ), and methyl-silsesquioxane or $CH_3–SiO_{3/2}$ (MSQ). Hydrogen silsesquioxane (HSQ) consists of the cage and the ladder structures after

the fabrication. The ladder structure of HSQ is shown in Figure 1.3 while the cage form is shown in Figure 1.4 [6].

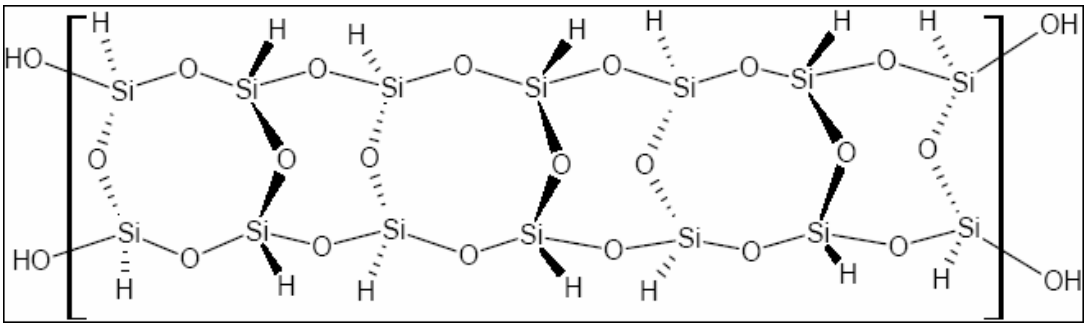

Figure 1.3. Ladder structure of Hydrogen silsesquioxane (HSQ).

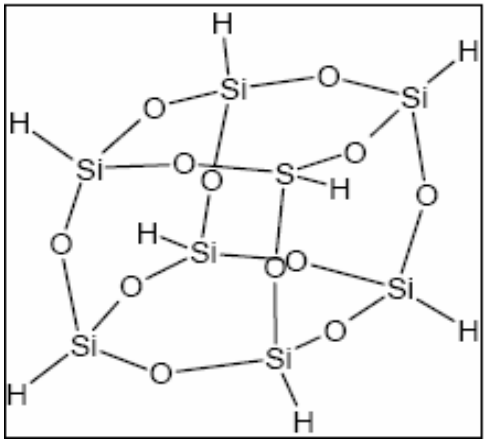

Figure 1.4. Cage structure of Hydrogen silsesquioxane (HSQ)

When the H on the Hydrogen silsesquioxane (HSQ) is replaced by organic substituent CH_3, the methyl silsesquioxane (MSQ) will be formed and the ladder structure of MSQ is shown in figure1.5.

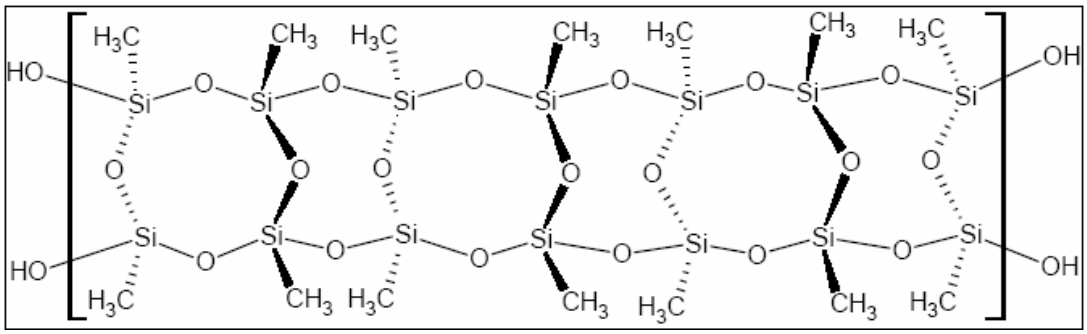

Figure 1.5. Ladder structure of Methyl silsesquioxane (MSQ).

MSQ materials have a lower dielectric constant compared with HSQ due to the larger size of the CH_3 group (2.8 and 3.0–3.2, respectively) and lower polarizability of the Si–CH_3 bond in comparison with Si–H bond. Increasing the porosity is one way to further reduce the *k* value of an existing material. The *k* value of an MSQ-based material, of which the total porosity is about 45%, has a *k* value about 2.0 [6]. The terminating groups play a water-blocking role, so that the films are normally hydrophobic. Moisture adsorbed by SSQ films can be either physisorbed, weakly bonded, or tightly bonded [12, 13]. Tight bonding can occur when a considerable amount of R groups are lost due to thermal annealing, oxidation, or plasma damage.

SSQ based porous low-k thin films are fabricated by spin-on coating technique. For example LKD low dielectric constant thin film is fabricated by spin-on, as represented in figure 1.6 [Processing steps from JSR Corp.].

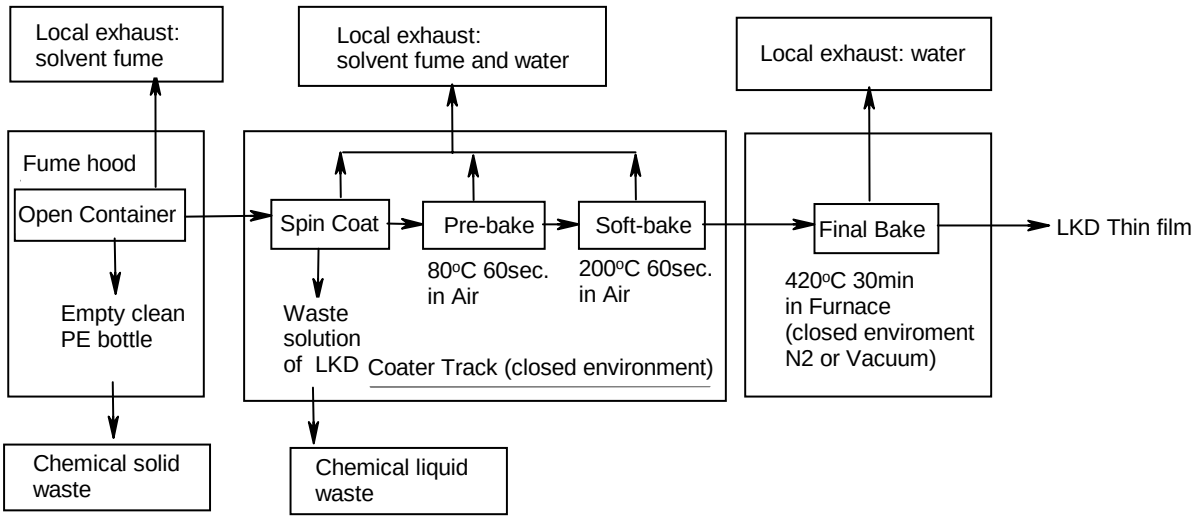

Figure 1.6. Fabrication Process of Porous LKD low-*k* film

The porous structure of SSQ-based thin films is primarily determined by the way the porosity is introduced in the films. For the sol-gel based SSQ materials, the mesopores are typically connected by meso-channels. For porogen based films, pore sizes are controlled by the size of the macroporogen. In such films the mesopores are probably connected by the constitutive porosity of the matrix materials [6, 14].

CVD deposited Silica based thin films

The silica based materials have the same basic structure as SiO_2, with a molecular structure in which each Si atom is bonded to four oxygen atoms and each oxygen atom to two silicon atoms ($SiO_{4/2}$). All kinds of silica have high chemical and thermal stability and fairly dense structures with a density between 2 and 3 g/cm^3. The high frequency dispersion of dielectric constant is related to the high polarizability of the Si–O bonds (distortion polarization). Lowering the *k* value can be achieved by replacing the Si–O bond with the less polarizable Si–F bond producing F doped silica glasses (FSG). Another approach is to dope the silicate glasses with C by introducing CH_3 groups, which also lowers the *k* value. Moreover, both fluorine and carbon increase the interatomic distances or ‘‘free volume’’ of silica which provides an additional decrease of dielectric constant.

Silica-based films have high thermal stability, which is the highest for F-doped films because of the Si-F strength (stable up to 750^{o}C, [15]). Carbon-containing bonds survive to higher temperatures than Si-H bonds (400^{o}C, [16]).

Silica-based materials can be non-porous (e.g., F doped silica), but most of them

exhibit constitutive porosity or subtractive porosity. Porous silica based low-*k* material has been developed by spin-on technique with a *k* value as low as 1.8 [17]. Pores are introduced into the silica-based low-*k* materials by either thermally removing the dopants or thermal decomposing the unstable CH_x phase during chemical vapor deposition (CVD) [18, 19].

Spin-on Organic polymers

According to the behavior of dielectric constant, organic polymers can be divided into two different groups: non-polar polymers and polar polymers. *Non-polar polymers* contain molecules with almost purely covalent bonds and consist of nonpolar C-C bonds. The dielectric constant can be evaluated by using only film density and chemical composite [20] and the dielectric constant can be independent of frequency. *Polar polymers* contain atoms of different electronegativity that give rise to an asymmetric charge distribution. Therefore polar polymers have higher dielectric loss and a dielectric constant that depends on the temperature and frequency at which they are estimated.

Most of the nonporous organic low-*k* films with sufficient thermal stability have a dielectric constant close to 2.6-2.8. The organic polymers of interest for low-*k* applications are almost hydrophobic and they adsorb only insignificant amounts of weakly bonded water. Because of the low mechanical stability and hardness, polymer low-*k* films cannot withstand some manufacturing processes such as CMP and wire bonding.

Spin-on technique is mainly employed for the fabrication of porous polymer low-*k* thin films. Some constitutive porosity presented in the film is related to the solvent extraction process and polymerization process. By using porogen, several subtractive porous organic polymers have also been synthesized [21]. Early generations of porous films have large voids (>100nm) and new generations of organic low-*k* films have a much smaller pore size of about 5nm.

1.2.3 Fabrication of porous low-*k* films

In general, the incorporation of nanopores into low-*k* films is achieved in one of the two approaches: either through evaporation of a solvent, or by burning off a thermally labile component in a composite film. “Sol-gel” is a common method, using solvent to produce porous silica thin films. In a typical sol-gel film technique [22], an alkoxysilane precusor, e.g., tetraethyorthosilicate or TEOS, along with catalysts, are dissolved in an alcohol. The solution is spin-coated onto a substrate. Chemical reactions are performed to produce a cross-linked gel network. The subsequent drying process removes the remaining solvent and a porous silica film is prepared. The porosity and pore sizes are controlled by the solid content, catalyst, pH, solvent type, and so on. Porous silica produced by the sol-gel process has open pores with extraordinarily high hydrophilic specific surface areas that favor water absorption. It usually requires surface modification during the manufacturing process to reduce the polarity [23]. Similar to the sol-gel technique, Dow Corning used a low-boiling point solvent to produce a homogeneous solution for spin coating and a high-boiling

solvent to generate porous silsesquioxane films [24]. The films prepared by such methods often have interconnected porosity as a result of the solvent evaporation path.

The other approach involves the use of thermally labile organic porogens to template the vitrification of a low-*k* material precursor [25]. IBM first developed porous methyl- silsesquioxane (shown in Figure 1.7) using a dendritic polymer, poly (ε–caprolactone)-based (PCL) material as a porogen [26]. Solutions of organic polymer mixed with low molecular weight silsesquioxane derivatives are spin-coated onto silicon wafers and heated slowly from 50°C to 430°C. In the low-temperature range (50-250°C), the silsesquioxane chains extend and crosslink to form a rigid network. Meanwhile, phase separation occurs and the PCL forms nano-domains in the MSQ matrix. Thermal decomposition of the porogen and volatilization of the resulting organic fragments occurs between 250°C and 430°C, leaving behind nanopores.

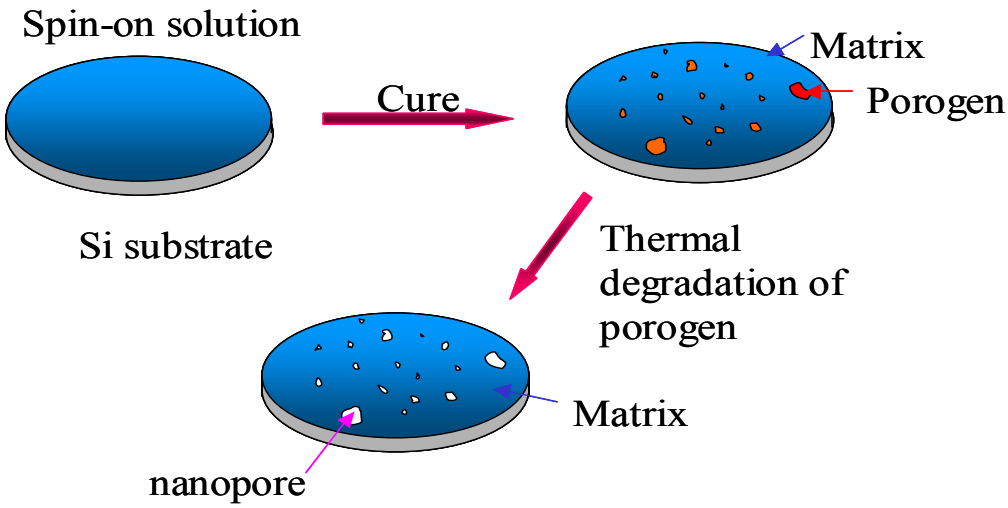

Figure 1.7. An example of porous low-*k* film fabrication through burning out a thermally labile component in a composite film

A variety of structural materials, such as block copolymers [27], surfactants [28], and organic nano-beads, have been explored as porogens in different kinds of matrices. The ability of such porogens to form nanoscopic domains in the cured matrix material is critical, since the film morphology is supposed to mimic that of the composite [29]. Porogens are chosen based on the required temperature windows for thermal decomposition, and on their ability to decompose into small, low molecular weight byproducts that can easily diffuse through the matrix. The resulting pore structure is determined by porogen structure, concentration, molecular weight and interaction with the matrix. Films with closed/isolated nano-porosity can be prepared using this composite method that involves a thermally labile porogen. Such systems can readily change from closed/isolated pore structures to interconnected/open pore structures as the porogen concentration in the composite increases.

1. 2. 4 Characterization of pore-sealing on porous low-*k* films

In order to characterize the surface sealing defects, two techniques have been studied and reported: *PALS* (Positronium Annihilation Lifetime Spectroscopy) and *EP* (Ellipsometric Porosimetry).

Positronium interactions with condensed matter and void volume are utilized for PALS characterization. As a beam of positrons is implanted into thin films, the positrons enter the solid and are quickly thermalized (several picoseconds) through collisions in the material from their initial energy of several Kev to several eV. A positron can either capture a bound molecular electron [30], or recombine with free

"spur" electrons generated by ionizing collisions to form the electron-positron bound state of positronium, Ps [31]. A small portion of positrons can diffuse back to the vacuum and may capture an electron to form "backscattered Ps" in vacuum.

The Ps atoms can exist in either the single state, with a lifetime of around 125 psec, or the triplet state (Ortho-Ps) with a lifetime of approximately 142 nsec when decaying in vacuum. After implanted into porous dielectric materials, Ortho-Ps is inherently localized in the pores and its natural lifetime will be reduced by interaction with molecular electrons during collision with the pore surface [32]. In the case of closed pores, a shorter lifetime of ortho-Ps will be expected if Ps is trapped in a smaller pore. In the case of interconnected pores, Ps can diffuse over a long distance. If pores are interconnected with one another and big enough, Ps will be easily diffuse into the surrounding vacuum, as illustrated in figure 1.8. Once the interconnected porous film is capped, PALS will be able to characterize the single lifetime which is corresponded to the average mean free path of Ps through the entire film. Beam-PALS is able to control positron implantation by varying beam acceleration energy [34] and samples can be depth-profiled by varying the mean implantation depth at different acceleration energy. In this way, PALS can characterize not only the surface sealing defect but also the thickness of dense layer.

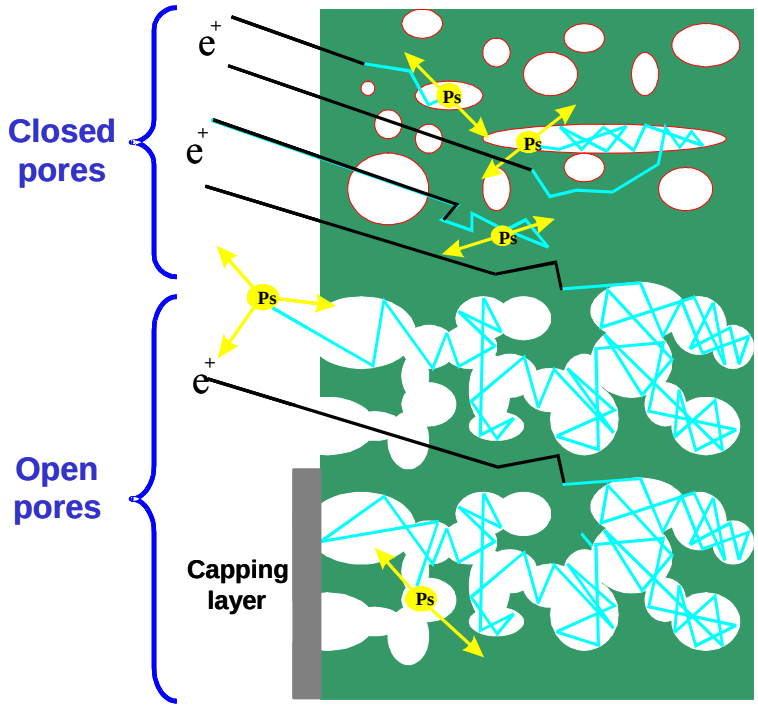

Figure 1.8. Positronium behavior in porous films [33]

In the case of EP measurement, one kind of solvent toluene is employed in the chamber to characterize the sealing performance. Once the solvent is absorbed into porous films, the ellipsometric angles will be changed. So the ellipsometric angles of the porous low-*k* film will be evaluated during the process of increasing the chamber pressure to the solvent saturation pressure at room temperature [6]. The sealing performance of the capping layer can be subsequently estimated by characterizing the elliposometric angel change when solvent pressure increases.

1.3. Multilevel Metallization for Integrated Circuits

Historically, each new generation of integrated circuits involved shrinkages of

device size. With continuous miniaturization, the metal system became a limiting factor in the number of devices that could be placed on a chip. The problem began to arise with larger circuits that used only one layer of metal for connection. Since the metal lines must be isolated from one another, the length of the metal lines became increasingly long. These long paths require additional area and cause longer signal delays. The metal will cover a large percentage of the circuit and eventually the point will be reached where the area needed to route the interconnect lines exceeds the areas required to build the devices. The packing density is said to be interconnect limited [35]. This problem can be minimized by using multiple layers of metal with the runs on one layer being orthogonal to the runs on the adjacent layers. This allows for the interconnect metal line to follow a shorter path and increases the packing density of devices in a circuit.

The multilevel metallization will also reduce the RC time delay of the interconnect system. The impact of the interconnect on the circuit speed (performance) is related to the RC time constant. The resistance of the interconnect line is: $R = \frac{\rho l}{w t_m}$ (2), where ρ = conductor volume resistivity, l = the length of interconnect, w = width of the interconnect metal and t_m = metal thickness. The capacitance of an interconnect line with a metal plate above and below the line is: $C = 2\varepsilon \frac{lw}{t_{IMD}}$ (3), where ε = relative dielectric constant, l = interconnect length, w = metal width and t_{IMD} = thickness of inter-metal dielectrics. This equation assumes the IMD thickness above the line is equal to the thickness of the IMD below the line. The product of R

and C then becomes: $RC = 2\varepsilon\rho\frac{l^2}{t_m t_{IMD}}$ (4). Referring to formula (4), the RC time delay will be greatly improved by multilevel metallization because multiple layers of interconnect allow shorter metal runs (shorter *l*).

In terms of the properties of the material in the multi-level metallization system, the metal with lower resistivity can further improve the RC delay at a certain feature size. Aluminum (Al) is the most widely used metal interconnects material during past few years, it has a low resistivity (2.65 μΩ·cm at 20^{o}C), could be etched in solutions without attack on the underlying films, and adheres well to other metals and to dielectric films. However, when the technologies move to 0.25 μm regime and beyond, alternate metallization based on metals having resistivities lower than that of Al will be needed. With its lower resistivity (bulk ρ of about 1.678 μΩ·cm at 20^{o}C), Cu is a promising replacement for Al alloys, not only in terms of speed but also in its higher electromigration and stress-induced voiding resistance. Physical vapor deposition (PVD), chemical vapor deposition (CVD) and electrochemical deposition techniques are used for Cu deposition in IC manufacturing industry currently [36].

Changes in the process integration technology are needed because of the use of Cu for interconnects. Figure 1.9 shows traditional subtractive etch scheme based on Al interconnect and Damascene schemes based on Cu interconnect. In the Cu-Damascene interconnect, dielectric trenches are patterned first, which are than filled with Cu metal and polished. The damascene structure introduces a whole new set of materials and processes distinctly different from the previous standard Al-on-silicon oxide interconnect technology. The previous technology was based on

the reactive ion etching (RIE)-based patterning of blanket *metal* films followed by dielectric deposition and planarization, as illustrated in Figure 1.9 (left). The transition to the Damascene schemes has made the process technologies required to form reliable devices very challenging [37]. In particular, there is a critical need to develop effective diffusion barrier (liner) materials that can prevent diffusion and intermixing of copper with adjacent dielectrics [38]. These must be thin layers that can conformally line the inner surfaces of the patterned dielectrics, i.e., the sidewalls and bottoms of the trenches and vias in the interconnected structure. Successful integration requires optimization of low-*k* dielectric stack with multiple processing steps like etch, lithography, metal barrier, electroplating and CMP polish of the Cu.

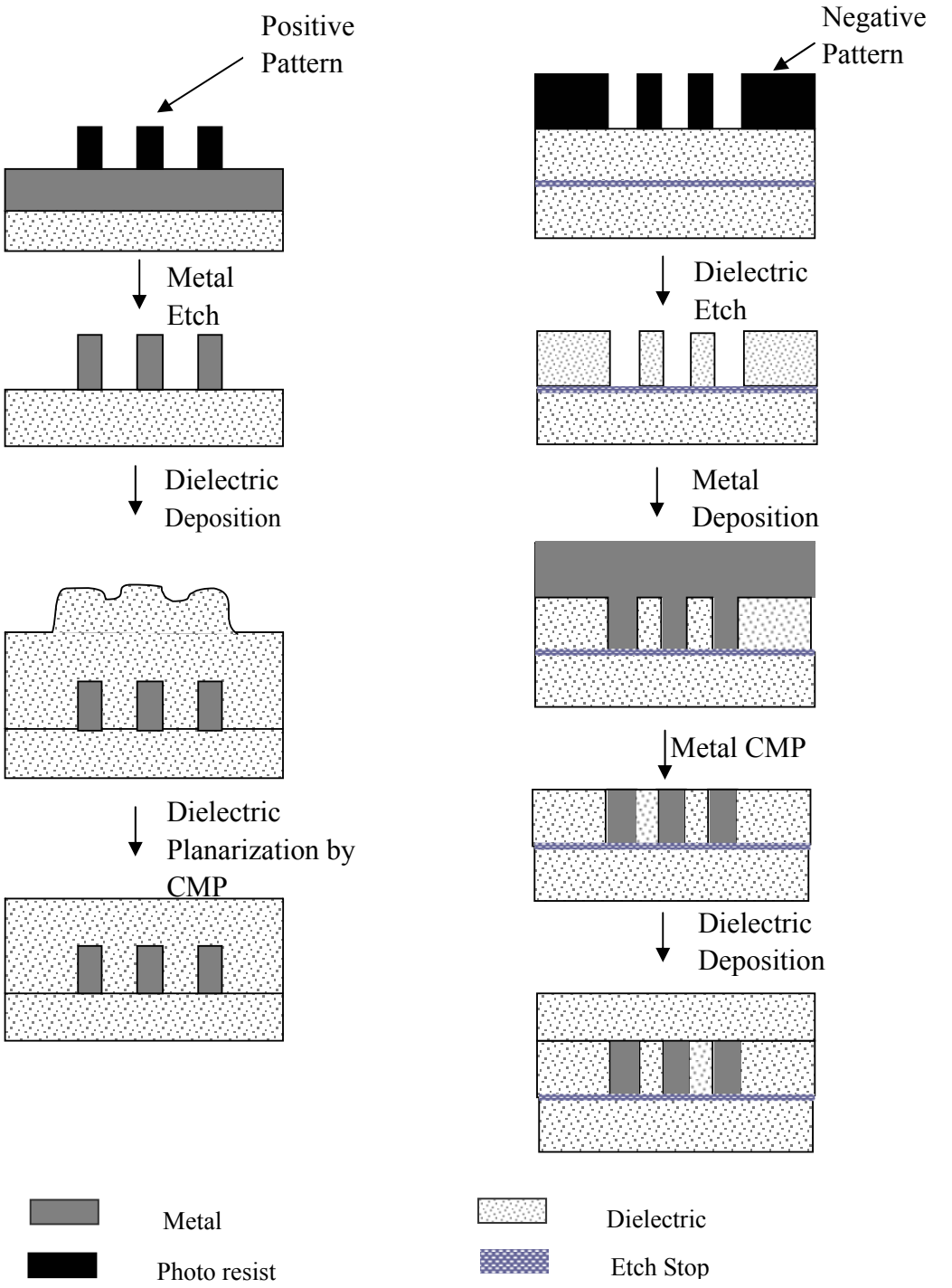

Figure 1.9. Interconnect fabrication approaches. Left: Conventional standard subtractive etch (Al as metal line); Right: Single-Damascene integration (Cu as metal line).

1.4. Porous Low-k Materials Damascene Integration Process

Compared with the conventional subtractive process for ICs interconnect, the damascene integration process is necessary for Cu/low-*k* back-end integration because of the difficulty of etching Cu. In the damascene approach to forming interconnects on ICs, a trench is cut into the dielectric layer and then filled with metal. Therefore this method has two major advantages: no etching of the metal layers is required; there is only a bottom interface for Cu, which helps to reduce overall via resistance [37]. The damascene interconnects can be formed with either a single-damascene or dual-damascene process.

1.4.1 Single-damascene Integration Process

Figure 1.9 (right) shows the typical single-damascene integration process. In the single-damascene process, the interlevel dielectric layer (ILD) is planarized after its deposition. Next, a via is patterned with a lithography step followed by the contact opening etching. Then a metal plug is formed in the opening by blanket deposition of the metal with a following CMP step. An intermetal dielectric layer (IMD) is then deposited and a second lithography step is used to form the pattern of trenches. After the trench is etched and the resist pattern is stripped, the trench is filled with metal (copper) and this metal is polished back by CMP to create a metal line embedded in a dielectric trench [38].

1.4.2 Dual-damascene Integration Process

In a dual-damascene structure, only a single metal deposition step is used to simultaneously form the metal lines and the metal in the vias. That is, both trenches and vias are formed in a single dielectric layer, after the via and trench recesses are etched. Thus, only one metal fill and one metal CMP step are required for each level of interconnect, resulting in lower process cost as compared with the single damascene process [38]. Two different fabrication sequences have been developed to produce dual-damascene structures:

1. Trench-First Dual-Damascene
2. Via-First Dual-Damascene

Figure 1.10 illustrates the trench-first dual-damascene integration process. In this sequence, the trench patterns are defined in the ILD first. The trench is then produced by etching the dielectric down to the etch-stop layer, followed by first resist layer stripping. A second resist layer is then spun on and the via-pattern-mask is used to create the openings in this resist layer-aligned to the trench that was etched previously. Figure 1.1 shows the process sequences in the via-first approach, in which vias are defined first in the ILD, followed by patterning the trenches. Then a metal deposition step is used to form metal lines and metal plugs with a following CMP step to remove excess metal [37]. The sequence is then repeated for next level of interconnect.

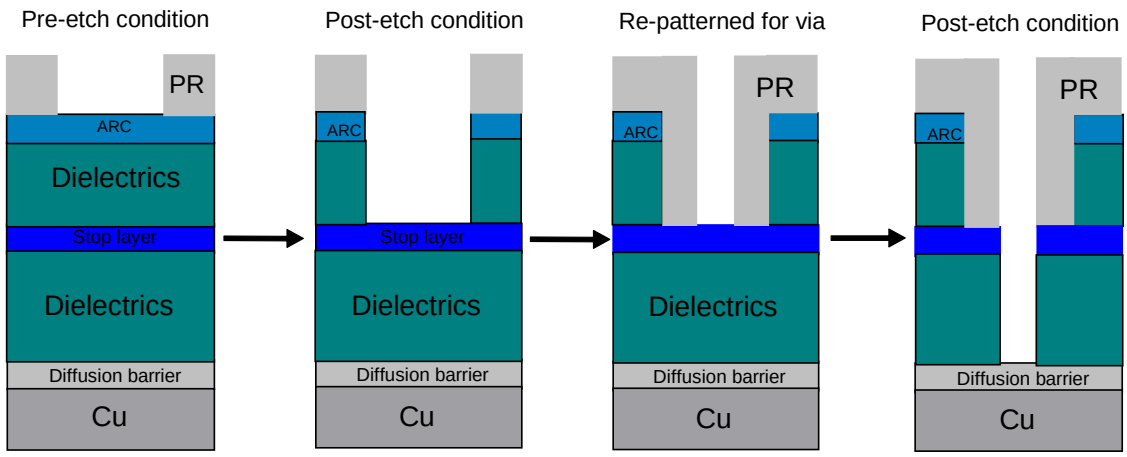

Figure 1.10. Trench-first dual-damascene integration process

1.4.3 Porous low-*k* Materials Damascene Integration Issues

Referring to the different kinds of interconnect process, there are several severe reliability and integration issues that have impeded the implementation of low-*k* dielectrics. These issues include thermally or mechanically induced cracking, poor mechanical strength, moisture absorption, chemical interactions (especially occurred during photolithography, etch/clean and dielectric/metal deposition) and poor thermal conductivity. To lower the dielectric constant to less than 2.5, pores have been introduced, which further reduces mechanical strength and may increase moisture/chemical adsorption as well [38]. In this study, we have tried to seal porous low-k materials in order to resolve the porous structure induced problems that might occurred in the etch/clean and metal deposition steps.

1.5. Thesis Objectives

In this chapter the integration of low-*k* dielectrics with copper for continuous improvement in the ICs device performance has been considered. As discussed, the

development of porous low-*k* dielectrics becomes very challenging because of various integration and reliability issues in the back-end of line process. Meanwhile, a good understanding of surface processing on porous low-*k* films is required to enhance the process compatibility in the back-end integration. For the successful integration, porous low-*k* films need to be sealed and the effective diffusion barrier with low dielectric constant needs to be formed and/or deposited on the ultra low-*k* films so as to reduce the effective *k* value of the dielectric stack. All of the above motivate the carrying out of this research.

In this work, we will focus on exploring the application of surface processing on the porous low-*k* films in resolving several key issues in the porous low-*k* materials and copper damascene integration.

In Chapter 2, the experimental methodologies for the surface processing on low-*k* materials, as well as the characterization techniques evaluating the film properties before and after the process have been introduced. Three kinds of processing, NH_3 plasma treatment, dielectrics trench etching and BN deposition on porous low-*k* films, have been illustrated respectively. Then, the characterization techniques employed in this work will be explained in four parts: chemical composition characterization, morphology measurement, electrical test and porosity evaluation.

In Chapter 3, low frequency NH_3 plasma treatment of the low-*k* film Zirkon LK2200 has been demonstrated to be an efficient process to seal the surface pores of the porous dielectrics. Firstly, the experiment parameters of the plasma treatment have been optimized in order to effectively seal the porous film with a minimal damage

which was induced by such a processing. Secondly, the chemical composition and morphology of the low-*k* films have been characterized to evaluate the properties before and after plasma processing. The formation of a densified layer has been experimentally identified. Thirdly, the copper diffusion barrier performance of the densified layer has been evaluated by using SIMS. Finally the Zirkon film is trench patterned so as to demonstrate the ability to delineate the porous films.

In chapter 4, the low frequency NH_3 plasma treatment has been applied to porous LKD 5109 film (from JSR Co. Pte. Ltd.) which is an alternative low-*k* material with a different porosity. In Chapter 4, the properties of the material are evaluated after the plasma process. The properties of the material as a Cu diffusion barrier after processing are evaluated by using SIMS and current-voltage measurement. Finally the sealing performance will be characterized by using PALS, followed by the discussion about pore sealing mechanism using plasma surface interaction.

In Chapter 5, plasma-deposited BN film has been evaluated as a copper diffusion barrier on porous low-*k* film LKD 5109. BN films are grown by Microwave Plasma (2.45 GHz) and Radio-frequency (RF) atom beam deposition (13.56 MHz) on LKD films in order to evaluate the compatibility of the two plasma processes with the physical integrity of the nanoporous films. Chemical composition and electrical properties of the dielectric stack have been characterized. BN barrier performance against Cu diffusion is then evaluated. Finally RIE system is employed to trench pattern the BN films to demonstrate the potential of BN as the capping layer.

In Chapter 6, I will make a conclusion for this study as well as the future work.

CHAPTER 2

EXPERIMENTAL SECTION

As what has been discussed in the previous chapter, three types of processing on porous low dielectric constant materials will be introduced in this chapter, namely (i) surface plasma treatment; (ii) low-*k* thin film trench patterning and (iii) BN thin film deposition. A number of characterization techniques have been employed to evaluate the properties of the low-*k* thin film properties after processing. The characterization techniques are divided into four main groups and will be discussed in the later part of this chapter.

2.1. Surface Plasma Treatment

The modification of the surface of porous films was carried out using a low frequency plasma (50.0 Hz−400.0 kHz) enhanced chemical vapor deposition (PECVD ORN 8092 from *TRION TECHNOLOGY Corp.*) system. The low-*k* films were first loaded into the PECVD chamber and then chamber pressure was pumped down to around 1.0×10^{-5} Torr. To purge the whole chamber, NH_3 gas was then led to the chamber for about 15 minutes at a flow rate of 100 sccm. Chamber temperature was increased to 300^{o}C or 400^{o}C in the ambient of NH_3. Once the temperature reached 300^{o}C or 400^{o}C, radio-frequency plasma power (150w, 100Hz) was turned on,

followed by the plasma treatment process that would last for 3s, 10s, 30s, 60s or 600s. Finally, chamber was cooled down to room temperature and the high vacuum conditions re-established.

Two kinds of MSQ based porous low-*k* material were treated by these processes: Zirkon LK2200 from Shipley and LKD 5109 from JSR.

2.2. Dielectric Films Trench Patterning

MSQ based low-*k* film Zirkon LK2200 (1.0μm in thickness) from Shipley and BN film on Si (150nm in thickness) has been patterned using the following process.

- **Photo Resist (PR) Spin-coating**

By using a spin-coater (Spincoater P6700 from *Specialty coating systems INC*), photo-resist (AZ 5214) was spun coated on the surface of the low-*k* film after spinning for 30s at a speed of 5000 rounds per minute (RPM). Then the low-*k* sample was placed into a furnace for 30mins soft baking at 90^{o}C. Employing a spin-coater, AZ 5214 was spun coated on the BN film after spinning for 45s at a speed of 6000 RPM, followed by 60s soft-bake on the hot plate at 95^{o}C.

- **Photolithography**

As illustrated in figure 2.1, a mask with a trench-pattern (from *Microelectronic Fabrication Lab, NTU*) has been used for the PR photolithography. Employing glass (transparent for visible and ultraviolet radiation) as the mask substrate, the dark part was covered by chromium, which can block radiation during photolithography process. By using contact printing (Mask Aligner from *KARL SUSS Corp.*), the exposing

radiation (wavelength 405nm, constant power 900w) was transmitted through white area (feature size 2.0um±0.3um) of the mask and certain parts of the photo resist were exposed to the radiation for 15 seconds.

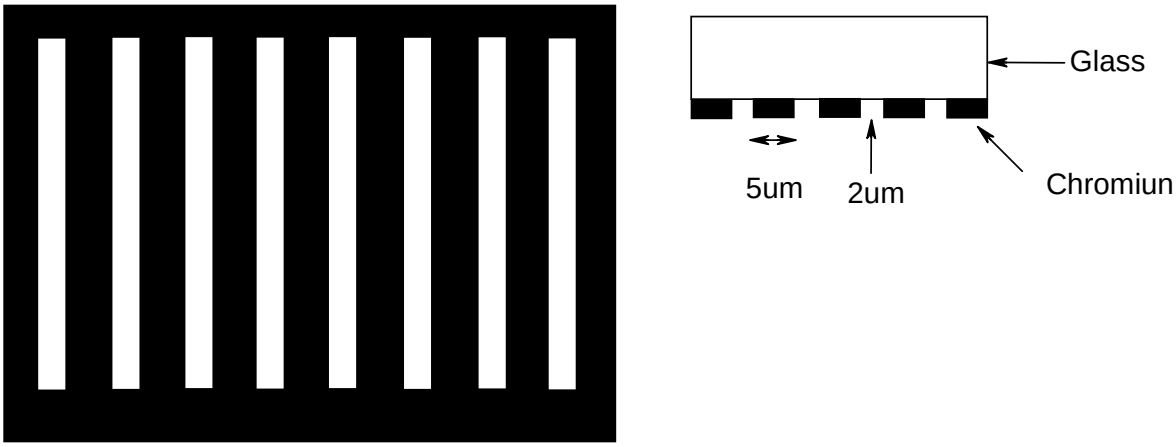

Figure 2.1. Mask Pattern for Photolithography

- **Photo Resist Development**

After photolithography, the photo resist was developed in the solution of developer AZ400k (Diluted 5 times by deionized water) for about 55 seconds, followed by 30min hard baking at 120^{o}C so as to stabilize the photo resist before plasma dry etching. Photo resist on the BN film was developed in the solution of AZ developer (diluted 2 times by deionized water), with a 5-minute hard-bake at 125^{o}C thereafter.

- **Plasma Dry Etching**

Employing RIE system (RIE Plasma lab80 Plus from *Oxford Instruments*), low-*k* samples received 7-minute dry etching at a chamber pressure of 30mTorr. Ar (50sccm) and CF_4 (50sccm) were utilized in RIE etching, with the RF plasma power of 150w, which created a DC bias voltage around 400 volts. By using the same RIE

system, 100nm BN films have been successfully patterned after 60-second dry etching at a chamber pressure of 50mTorr. Ar (30sccm) and CF_4 (50sccm) were used in RIE etching, with the RF plasma power of 250w, which created a DC bias voltage of 492v.

- **Photo Resist Stripping**

Finally the dielectric samples was immersed in acetone (Photo resist is soluble in acetone) for ultrasonic rinsing for about 5min, thus stripping the photo resist and polymer residue induced by RIE etching.

2.3. BN Thin Film Deposition

Microwave Plasma enhanced Chemical Vapor Deposition (MWPECVD)

MWPECVD (from AsTex) has been used for BN thin film growth on both silicon substrate (p type) and porous low dielectric constant material LKD 5109. Deposition processes were carried out for 4 minutes at different temperatures: 200^{o}C, 300^{o}C, 400^{o}C and 500^{o}C. The frequency of microwave enhanced plasma power was 2.45 GHz and power forwarded in process was around 400W. N_2, A single source precursor based borozine, diluted in hydrogen and nitrogen, was utilized in BN growth with the flow rates of 5 sccm, 40sccm and 20sccm for the respective gases.

Radio-frequency Plasma enhanced Chemical Vapor Deposition (RFPECVD)

RFPECVD (Oxford Applied Research) with the plasma power frequency of 13.56 MHz was also employed for BN deposition on LKD thin film by using pure borozine.

The deposition processes were carried out at around 400^{o}C for 3mins, 5mins and 7 mins. Plasma power was around 300w, chamber pressure has been lowered to 5×10^{-8} torr as the base pressure and chamber pressure in process was about 2.0×10^{-4} torr.

2.4. Characterization Techniques

The characterization techniques used in this work have been divided into four groups: chemical composition characterization, morphology measurement, electrical test and porosity evaluation.

2.4.1. Chemical Composition Characterization

1. Fourier Transform Infrared Spectroscopy (FTIR)

FTIR Spectrum 2000 (*Perkin Elmer Corp.*) has been used in characterizing the chemical structure of the low-*k* materials after different kinds of surface processing. In the IR measurement, transmission mode has been employed for low-*k* thin films chemical composition evaluation after plasma treatment, thermal annealing and thin film deposition.

2. Raman Spectroscopy

Laser Raman Microscope (from *Renishaw PLC*) has also helped to estimate the chemical structure of porous low-*k* films and it is especially efficient for a few chemical bonds without strong absorption in FTIR spectrum. The laser of the equipment can penetrate through film surface for about 1 μm; therefore the Raman

spectra obtained represent the entire chemical composition of the materials exposed to laser radiation.

3. X-ray Photoelectronic Spectroscopy (XPS)

XPS (VG ESCALAB 220i-XL Instrument) greatly helped us in characterizing the detailed chemical structure and stoichiometry of the low-*k* films. With a background pressure in the low 10^{-10} mbar range during analysis, the XPS instrument is equipped with a monochromatic Al Kα (1486.7 eV photons) and an unmonochromated Mg Kα X-ray source (1253.6 eV photons), a concentric hemispherical analyzer and a magnetic immersion lens (XL lens) to increase the sensitivity of the instrument. It successfully investigated the surface chemical composition change of porous low-*k* materials after certain plasma treatment.

4. Time-of-flight Secondary Ion Mass Spectroscopy (Tof-SIMS)

Tof-SIMS (Tof-SIMS IV) provided by ION TOF Corp. has been employed to evaluate the depth profile of chemical composition. In SIMS characterization, Ar beam of 3 keV (or 1 keV) was used for sputtering, Ga primary beam at 25 keV in energy was employed for positive analysis and Cs primary beam for negative analysis. This equipment not only helped to demonstrate the barrier performance of surface densified layer against Cu diffusion, but effectively estimated the BN thin film chemical structure on porous low-*k* films.

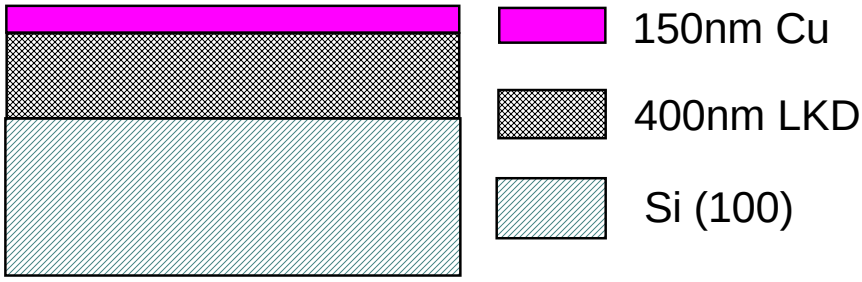

Figure 2.2. MIS structure for SIMS experimental demonstration of barrier performance

As shown in figure 2.2., around 150nm Cu has been sputtered by PVD (PVD Sputtering System from *Denton Vacuum INC*) on low-*k* dielectrics after plasma treatment, followed by one hour thermal annealing in quartz thermal furnace (Annealing Thermal Atmospheric Furnace from *Winston-Salem Corp.*) in N_2 ambient. To avoid knock-in effect in SIMS measurement, Cu layer has been etched by 26% $(NH_4)_2S_2O_8$ solution in advance, then SIMS was used to characterize the Cu depth profile in low-*k* film so as to evaluate the barrier performance.

2.4.2. Morphology Measurement

1. Atomic Force Microscope (AFM)

By using contacting mode measurement, AFM XE-100 (from PSIA) was used to evaluate the surface morphology and to analysis mean roughness of film surface after different kinds of treatment.

2. Scanning Electron Microscope (SEM)

SEM (JSM-6700FEG SEM from JEOL Corp.) was employed to measure the thickness of thin film deposited on low-*k* materials, to characterize the cross-section critical dimensions of the patterned trenches in the dielectric films and to help characterize the cross-section morphology of dielectric stacks after BN deposition.

3. Transmission Electron Microscope (TEM)

High resolution TEM (CM 300 TEM from Philips Corp.) was used for evaluating the thickness of densified layer on low-*k* films after certain plasma treatment. To prepare samples for TEM characterization, several steps have been finished, as illustrated in figure 2.3.

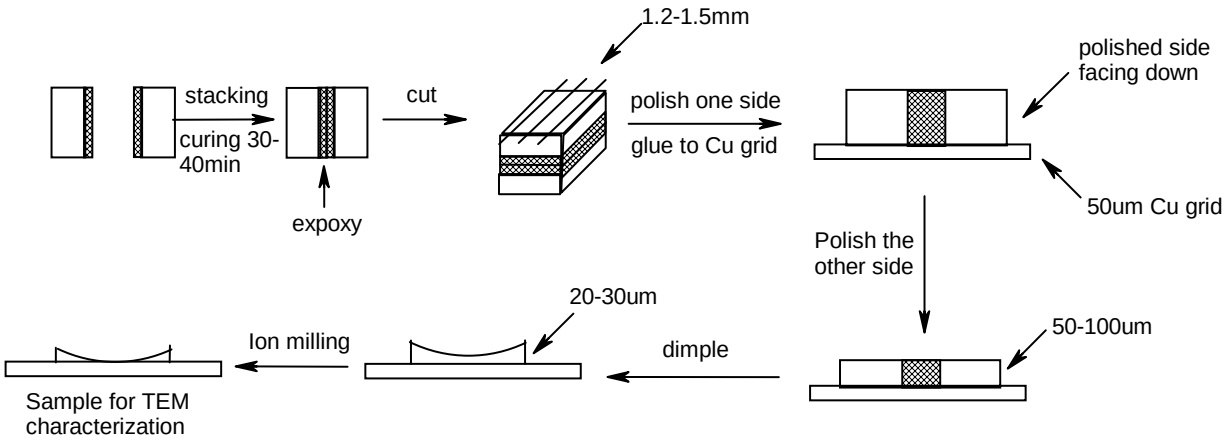

Figure 2.3. Process steps of preparing samples for TEM characterization

4. Surface Profiler

The thicknesses of deposited BN thin films and the trench depth after RIE etching have been estimated by surface profiler *(KLA-TENCHOR Corp. P-10 Surface Profiler)*.

2.4.3. Electrical Test

In this thesis, both relative dielectric constant of low-*k* films and leakage current density of Metal-Insulator-Silicon (MIS) structure after Cu integration with the porous low-*k* materials were characterized by the Advanced Computerized Semiconductor Measure System (ACSM System) from Materials Development Corporation. Metallization of the dielectric films for electrical contacts in capacitance-voltage (C-V) and leakage current-voltage (I-V) measurement was achieved by electron-beam deposition system and PVD sputtering system. Two kinds of shadow mask have been employed for metal electrodes preparation: one mask with a number of holes of 1mm^2 in area, and the other mask with holes of 1mm in diameter.

1. Capacitance-voltage Measurement (C-V measurement)

Capacitance-voltage (C-V) measurement (ACSM system) has been used to estimate the effective *k* value of the dielectrics in this study. By using the C-V measurement, the capacitance of the dielectric film can be measured, thus the *k* value of the film before and after surface processing can be calculated accordingly. As shown in figure 2.4, a typical MIS capacitor in accumulation can be modeled as the

series combination of a capacitor C_S representing the insulator capacitance and a resistor R_S representing the combination of substrate resistance, back contact resistance and cable resistance [39].

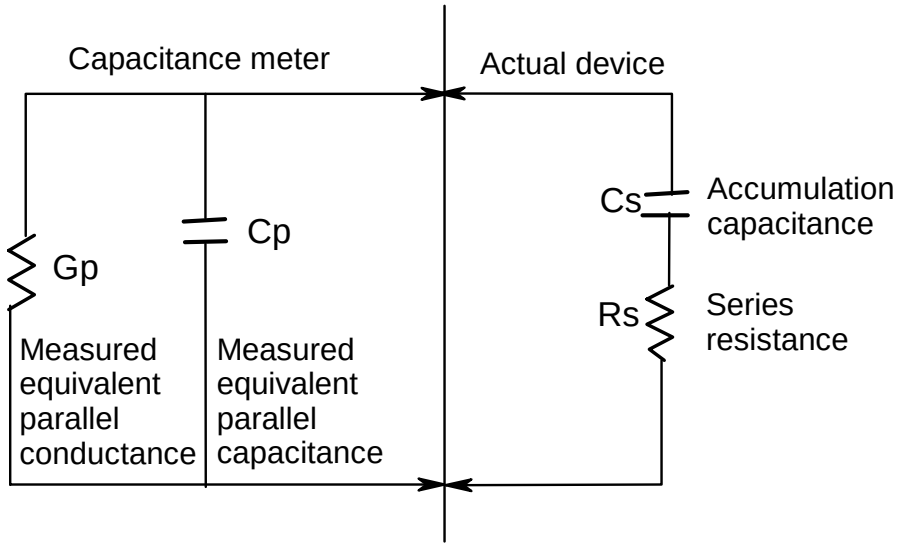

Figure 2.4. Circuit models for MIS device in accumulation and admittance by a C-V measurement

The relationship between C_P, the measured capacitance, and C_S the actual oxide capacitance, is:

$$C_p = \frac{C_s}{1 + \omega^2 R_s^{\,2} C_s^{\,2}} \qquad (5)$$

where ω = the angular frequency of ACSM measuring signal. In our C-V measurement, R_S was lower than 150Ω because of ohm back contact and C_S was less than 200PF, so $\omega R_S C_S \ll 1$. Thus, C_P equals C_S and the capacitance measured is accurate.

To introduce the basic theory for C-V measurement, the MOS capacitor will be discussed first. The MOS capacitor consists of a Metal-Oxide-Semiconductor

structure as illustrated by Figure 2.5. Shown here is the semiconductor substrate with a thin oxide layer and a top metal contact, referred to as the gate. A second metal layer forms an Ohmic contact to the back of the semiconductor, this is called the bulk contact, and it reduces the contact resistance between the test tool and the capacitor. The structure shown has a *p*-type substrate. We will refer to this as an *n*-type MOS or n-MOS capacitor since the inversion layer is the *p* type channel [40].

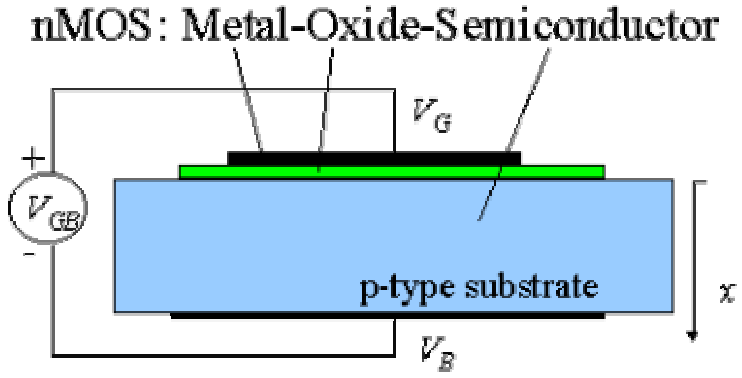

Figure 2.5. nMOS Metal-Oxide-Semiconductor capacitor.

When the gate voltage is applied to the MOS capacitor during C-V measurement, the capacitor will go through three stages with the applied voltage. These stages are accumulation, depletion and inversion. Accumulation occurs when one applies a voltage less than the flat-band voltage (appendix A) [39]. As shown in figure 2.6, the negative charge on the gate attracts holes from the substrate to the oxide-semiconductor interface. Only a small amount of band bending is needed to build up the charge accumulation so that almost all of the potential variation is within the oxide. As a voltage more positive than the flat-band voltage is applied, a negative charge builds up in the semiconductor. Initially this charge is due to the depletion of

the semiconductor starting from the oxide-semiconductor interface. The depletion layer width further increases with the increasing gate voltage. As the potential across the semiconductor increases beyond twice the bulk potential, another type of negative charge emerges at the oxide-semiconductor interface: this charge is due to minority carriers, which form a so-called inversion layer [40].

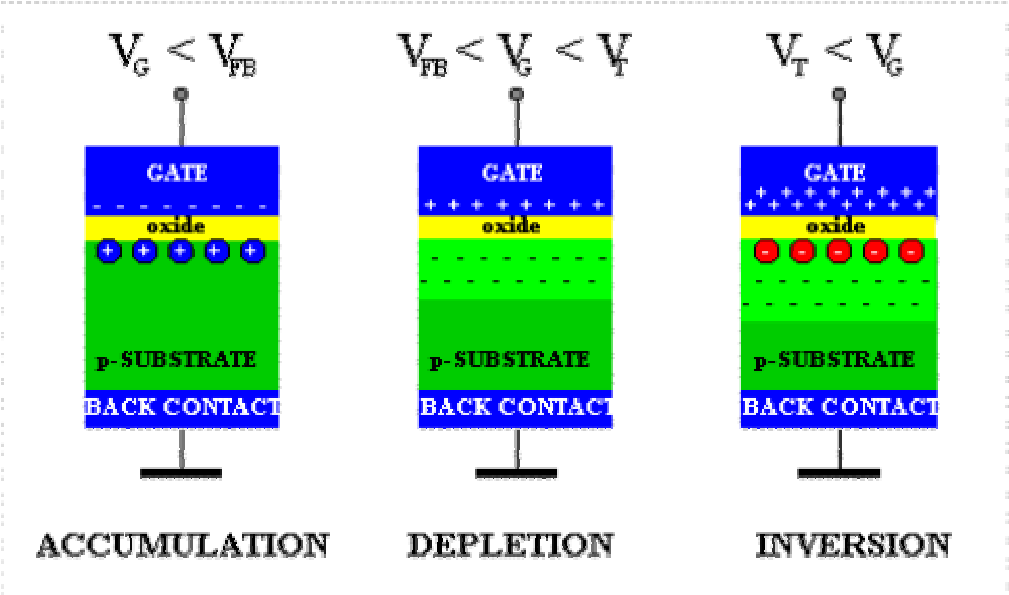

Figure 2.6. Interface charge in accumulation, depletion and inversion status.

During the C-V measurement, the MOS structure is treated as a series connection of two capacitors: the capacitance of the dielectric film and the capacitance of the depletion region. In accumulation status, there is no depletion layer and the remaining capacitor is the oxide capacitor, so the measured capacitor capacitance C equals to the oxide capacitance at accumulation status, Cox. Based on the formula $C = A\frac{K}{T_{ox}}$ (6), where C=capacitor capacitance, A=electrode area and T_{ox} = electrode spacing, the relative dielectric constant can be calculated:

$$k = \frac{T_{ox} C_{ox}}{A}$$

Where k is the relative dielectric constant of dielectrics, C_{OX} is the dielectric capacitance in the accumulation region, A refers to the area of the metal electrode of the MIS structure and T_{OX} represents thickness of insulators.

As represented in figure 2.7, Au electrodes (200nm) of $1mm^2$ in area were fabricated on BN surface by electron beam deposition (EDWARDS FL400 from *Fisher Scientific Corp.*) to form a metal/insulator/semiconductor structure of Au/BN/LKD/Si. Tungsten probe was used to contact with the Au electrodes and Au (200nm) was also developed on the backside of Si substrate so as to form ohm contact between Si and ACSM system.

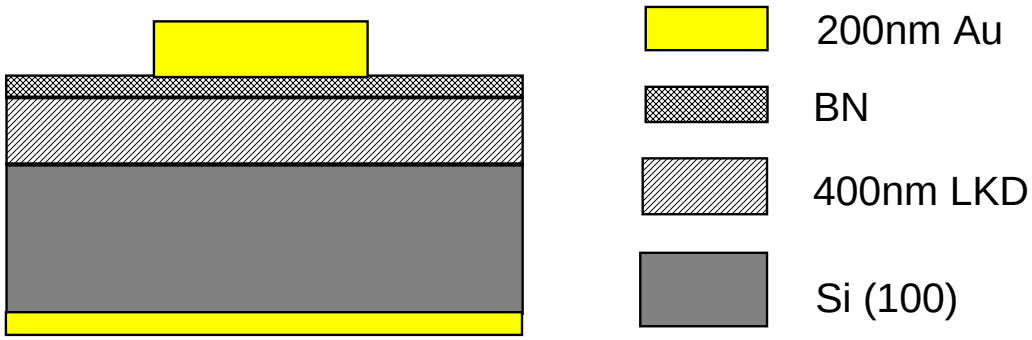

Figure 2.7. Metal/insulator/semiconductor structure for BN/LKD stack C-V measurement

By using PVD sputtering system, Au electrodes (200nm) 1mm in diameter were prepared on the surface of low-*k* materials after plasma treatment, as shown in figure 2.8. Au (200nm) was also sputtered on the backside of Si as to form ohm contact and lower the series resistance.

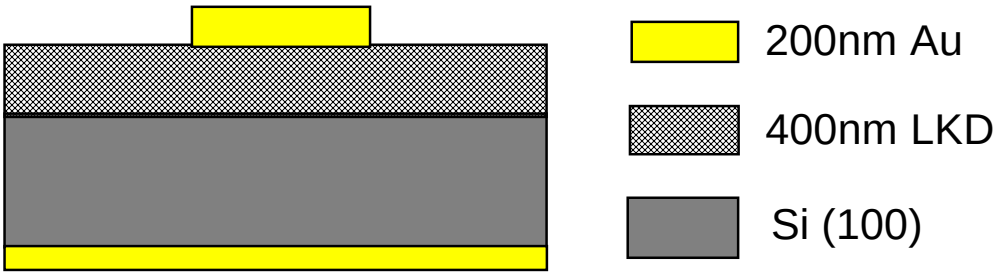

Figure 2.8. Metal-insulator-semiconductor structure for LKD C-V measurement

2. Leakage Current-Voltage Measurement (I-V measurement)

In this study, the leakage current-voltage measurement has been used to check the barrier performance against Cu diffusion through low-*k* dielectric films. As shown in figure 2.9, Cu electrodes (150nm) 1mm^2 in area were fabricated on the surface of dielectrics by using a shadow mask in PVD sputtering system. Au was developed on the backside of Si substrate to form the ohmic back contact.

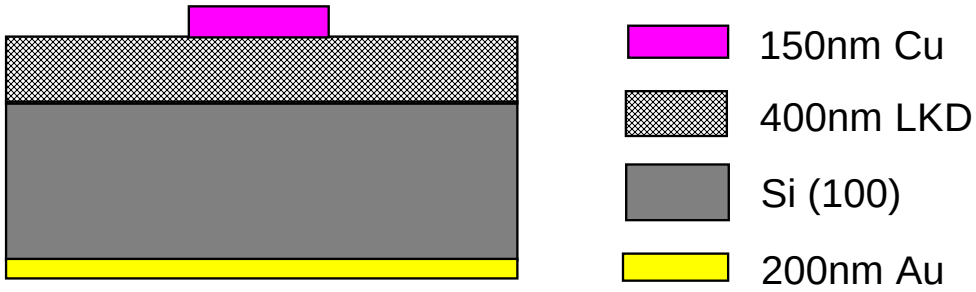

Figure 2.9. Metal-insulator-semiconductor structure for I-V measurement

The porous dielectric layers are especially susceptible to copper diffusion. After the deposition of copper and thermal annealing, I-V measurement is carried out on the MIS structure to check for leakage current. Fowler-Nordheim tunneling has been studied extensively in Metal-Oxide-Semiconductor structures where it has been

shown to be the dominant current mechanism, especially for thick oxides. The basic idea is that quantum mechanical tunneling from the adjacent conductor into the insulator limits the current through the structure. Once the carriers have tunneled into the insulator they are free to move within the valence or conduction band of the insulator. The calculation of the current is based on the WKB approximation yielding the following relation between the current density, *JFN*, and the electric field in the oxide, *Eox*: $J_{FN} = C_{FN} E_{ox}^{\ 2} \exp_{ox}(-\frac{4}{3}\frac{\sqrt{2m_{ox}^{*}}}{q\hbar}\frac{(q\phi_B)^{3/2}}{E_{ox}})$, where Φ_B =the barrier height at the conductor/insulator interface in Volt, m_{ox}^{*} =the effective mass of the insulator, J_{FN} =the current density and *Eox* =the electric field in the oxide.

To simulate the extreme process condition in IC manufacturing, the MIS structure was exposed to one hour thermal stress at 400^{o}C in N_2 ambient so as to test the barrier layer reliability. Tungsten probe was used to connect with Cu electrode and I-V characteristics were evaluated in the ACSM system.

2.4.4. Porosity Evaluation

The porosity and sealing performance of the porous low-*k* thin films after plasma treatment was evaluated using the beam-PALS measurement in the University of Michigan (Dept. of Materials Science and Engineering).

Beam-PALS is able to control positron implantation by varying beam acceleration energy [26] and samples can be depth-profiled by varying the mean implantation depth at different acceleration energy. In this way, PALS can characterize not only the surface sealing defect but also the thickness of densified layer.

A good review of positron-material interactions can be found in a paper by Schultz and Lynn [34]. Some of the processes by which positrons and Ps may interact

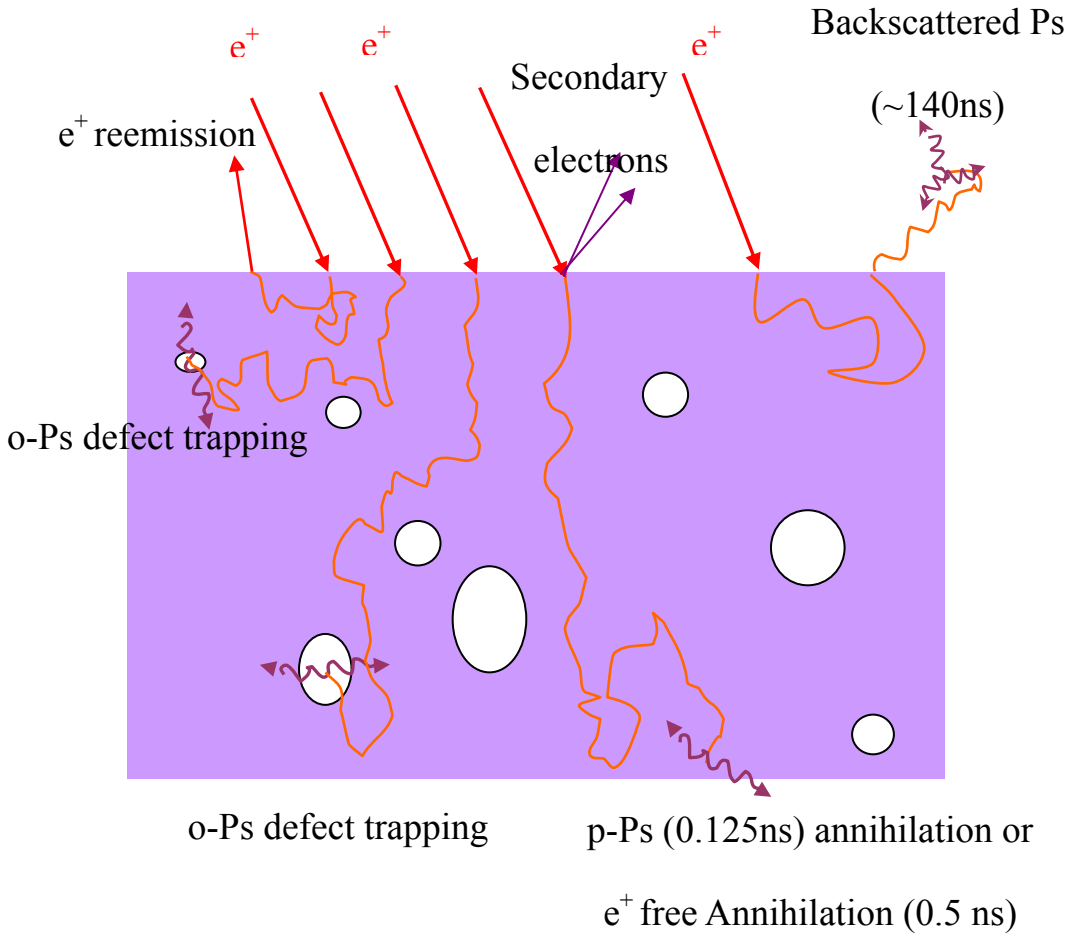

Figure 2.10. Positron and Ps interactions with condensed matter

with condensed matter are illustrated in Figure 2.10. For our purpose we will concentrate on Ps behaviors. When a beam of positrons is implanted into thin films, the positrons enter the solid where they are quickly thermalized (several picoseconds) through collisions in the material from their initial beam energy of several keV to several eV. They then diffuse through the solid. A positron can either capture a bound molecular electron [30] or recombine with free "spur" electrons generated by ionizing

collisions to form the electron-positron bound state of positronium, Ps [31]. A small fraction of positrons can diffuse back to the vacuum. They can capture an electron on the way and form "backscattered Ps" in vacuum. Note that Ps cannot be formed in the bulk of metals, as the high electron density effectively screens out the Coulomb attraction.

In insulating materials, the Ps atom may exist in either the singlet state (*para-Ps* or *p-Ps*) which decays predominantly into two gamma-rays with a lifetime of approximately 125 psec, or the triplet state (*ortho-Ps* or *o-Ps*) which in vacuum decays predominantly into three gamma-rays with a lifetime of approximately 142 nsec (such as the backscattered Ps). Within condensed matter, *ortho*-Ps prefers to localize in the pores since the binding energy of positron and electron pair increases upon entering a void. Its natural annihilation lifetime of 142 ns can be markedly reduced by interaction with molecular electrons during collisions with the pore surface. The collisionally reduced o-Ps lifetime is correlated with void size and forms the physical basis for probing pore structure with PALS.

In using PALS with thin films, an electrostatically or magnetically focused beam of several keV positrons is generated in a high vacuum system using a radioactive beta-decay source. Two electrostatically focused positron beam systems have been used for this study and they are schematically shown in Figure 2.11 and Figure 2.12.

In both systems, a 25 mCi ^{22}Na radioactive source is used to produce positrons. The positrons are projected into the moderator, which is made of a metal that possesses a negative work function for positrons. A small fraction of positrons will be

ejected back with ~1eV energy into the vacuum and become the source for the beam. Different moderator setups have been used in these two systems. A 5 μm Ni foil of the transmission style is used in System I for a better-focused beam. System II is designed for a higher rate using a tungsten vane-moderator in the reflection style [34]. In both systems the positron beam is then accelerated by electrostatic lenses and transported into the sample chamber and deflected into a target sample as shown in the inset to Figure 2.11. The beam energy can be varied between 0.25 through 6 keV in System I and up to 20 keV in System II. The final beam spot size is on the order of 1 mm diameter in System I and about 5 mm in System II.

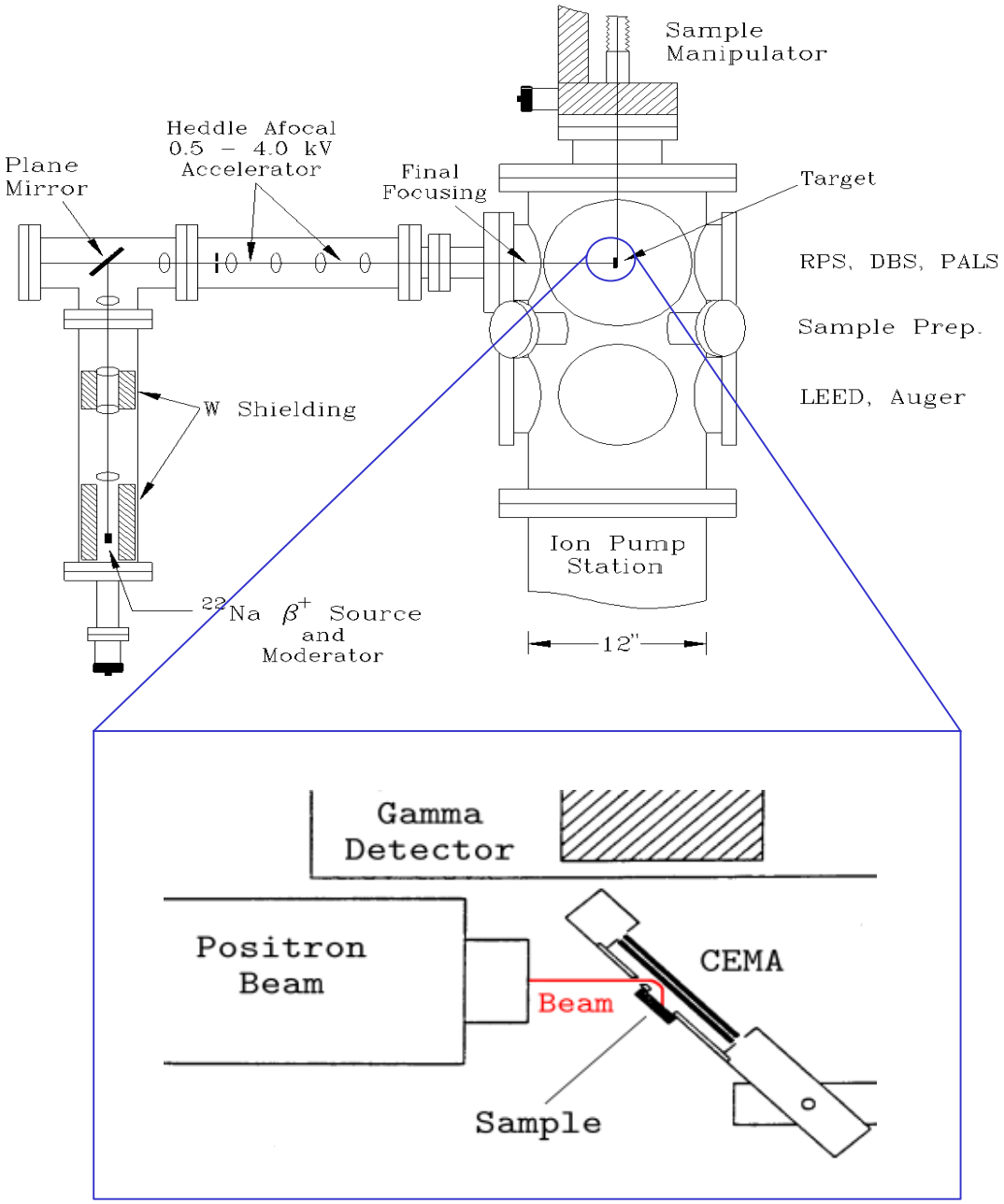

Figure 2.11. Schematic of the Depth-Profiled Positron Spectrometer: System I designed for good timing resolution

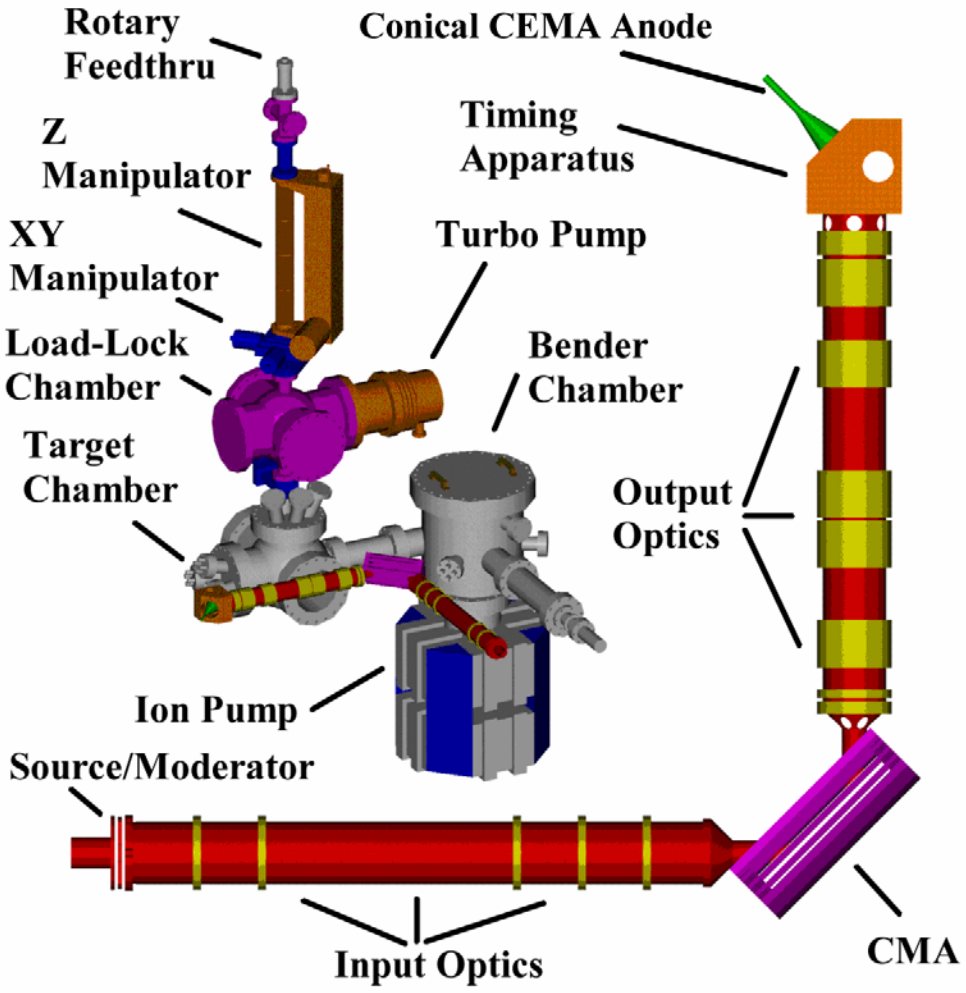

Figure 2.12. Schematic of the new slow positron beam: System II designed for high rate of events

In beam-PALS, fast coincidence timing techniques are used to measure the lifetimes of annihilating positronium [41]. The timing start signal is provided by the secondary electrons produced when the positron beam strikes the sample surface because the thermalization time of the positron (several picoseconds) is negligible compared to Ps lifetimes (several up to 140 nanoseconds). A channel electron multiplier analyzer (CEMA) plate (positive – biased) detects the secondary electrons and provides the start pulse. Typical start rates are 2000 ~ 3000 counts /second in System I and can be up to 30,000 counts/second in System II. The stop signal is provided by one of the

annihilation gamma-rays detected by plastic scintillators. Typical stop rates are about 300 counts/second in System I and are about ten times higher in System II using a 2" detector. These numbers can be at least tripled by using a 4" gamma detector. Ps lifetime for each event is then determined between the CEMA signal and the subsequent detection of an annihilation gamma ray. Fast timing electronics are very typical for PALS systems. We use Ortec 583/584 constant fraction discriminators and a Lecroy 4202/4204 time-to-digital converter with 156 picoseconds/channel resolution. Each event is then stored through a data accumulation system and eventually a lifetime histogram is generated. The system timing resolution throughout this study is normally 0.3 ns and 0.8ns, respectively for the two beams. This is sufficiently small to resolve ortho-Ps lifetimes (several tens of nanoseconds) in the mesoporous low-*k* films.

CHAPTER 3

ZIRKON LK2200 FILMS PORE-SEALING BY NH_3 PLASMA TREATMENT

As introduced in chapter 1, surface plasma treatment on porous low-*k* materials with a view in improving the diffusion barrier properties to copper will be evaluated in this chapter. The material chosen is MSQ-based porous low dielectric constant material Zirkon LK2200 ($k \approx 2.2$), supplied by Shipley Company, L. L. C.

3.1. Introduction

As device dimensions continue to shrink to 0.18 μm and below in ULSI technology, RC delay becomes the limiting factor in integrated circuit performance. Because low-*k* materials have ultra low dielectric constant (2.2 and below), they have been developed to replace conventional SiO_2.

As discussed previously in chapter 1, the pores of the ultra low-*k* films have to be sealed before further processing due to the integration and reliability issues induced by the porous structure. Different strategies for capping/sealing of porous low-*k* materials have been investigated recently. F. Iacopi and coworkers reported that mesoporous low-*k* films were effectively sealed by depositing continuous thin films of

Ta (N) on the surface of the porous dielectrics [6, 14]. In other works, they employed the deposition of Ta (N)/SiC thin films for the surface reconstruction of the porous low-*k* materials to achieve efficient pore-sealing [42]. A controlled plasma treatment process has also been reported to lead to the formation of ultra thin dense layer on *microporous* dielectric films, which shall be another attractive strategy in sealing the porous dielectrics [43, 44]. In this study, low-frequency NH_3 plasma treatment is employed for sealing the *mesoporous* low-*k* film Zirkon LK2200.

Zirkon LK2200 is a kind of MSQ-based mesoporous low-*k* material with the *k* value of 2.2. The thickness of the film is about 1.02 μm and the refractive index of the film is 1.2718. By using PALS characterization, porosity and pore size of the low-*k* film has been evaluated to be 30% and 2.7nm.

3.2. Experimental Section

In this study, low-frequency NH_3 plasma treatment has been carried out on MSQ-based Zirkon LK2200 films in order to seal the porous dielectrics. The low-*k* films have also been trench-patterned to demonstrate the ability to delineate the porous films. The low-*k* material was treated by NH_3 plasma in a PECVD reactor for a very short time. The substrate temperature was adjusted to between 300^oC-400^oC with a processing chamber pressure of 300.0 mTorr. The plasma power forwarded was 150 watts and the flow rate of NH_3 was 100.0 standard cubic centimeters per minute (sccm). Second, a Cu film of 150 nm was deposited on the low-*k* samples by PVD

sputtering system and exposed to one hour thermal stressing at 400^{o}C in N_2 ambient. The diffusivity of Cu in the porous low-*k* film was then evaluated by Time of Flight−Second Ion Mass Spectroscopy (Tof−SIMS). Finally Zirkon LK2200 was trench-patterned in RIE system to demonstrate the ability to employ the Zirkon films in the damascene interconnect scheme.

Beam-PALS has been employed to evaluate the sealing performance of low-frequency plasma treatment. Fourier transform infrared (FTIR) spectra, Raman spectroscopy and SIMS were applied to investigate the chemical structure of the porous material before and after different time NH_3 plasma treatment. Cross-section TEM successfully characterized the densified layer on the surface after plasma treatment and AFM was also used to evaluate the surface morphology after such processes. Cross-section SEM (XSEM) was used to characterize the critical dimensions of the patterned trenches in the low-*k* films after RIE etching and post-etching clean.

3.3. Results and Discussion

3.3.1. Pore-sealing efficiency of NH_3 plasma treatment

The Zirkon films have been treated by NH_3 plasma for different process time: 3s, 10s, 30s, 60s and 600s. Beam-PALS has been used to evaluate the pore-sealing efficiency of the PT process. All these processed films, along with Si-capped porous films, and unprocessed porous films which are used as control samples, were depth

profiled with beam-PALS by varying the implantation energy from 1 to 8 keV. To get the control data, Si-capped Zirkon LK2200 and unprocessed Zirkon LK2200 films have been characterized by PALS, as shown in table 3.1. Compared with the Ps intensity (in vacuum) of the uncapped film, the Ps intensity (in vacuum) of Si-capped films decreased to 1.4% and 0.9%, with the implantation energy of 5.0 KeV and 8.0 KeV.

Samples	Energy (KeV)	Mean Depth (nm-g/cm^3)	Ps lifetime (ns)	Ps Intensity	Ps Intensity in vacuum
Uncapped	2.0	85	27.2 1.6	4.9%	22.1%
	3.0	160	34.4 0.2	8.5%	21.1%
	4.0	260	37.9 1.2	8.0%	12.6%
	5.0	370	38.8 0.3	13.3%	12.7%
	8.0	780	41.8 0.5	11.3%	8.5%
Si-capped	5.0	370	47.8 1.2	5.9%	1.4%
	8.0	780	48.5 0.4	8.7%	0.9%

Table 3.1. PALS characterization of Zirkon LK2200 films with and without Si-capping.

Table 3.2 also shows the PALS data of the low-*k* samples after different PT processes. As shown in table 3.2, the Ps lifetime remains constant when the implantation energy is varied, and the intensity of Ps is comparable to Si-capped film, these evidence the formation of the densified skin layers in the plasma-treated films [32].

Samples	Energy (keV)	Ps lifetime (ns)	Ps intensity (%)	Ps intensity in vacuum (%)
10s	2	52.3	7.3	3.0
	3	52.6	9.3	2.2
	5	52.0	13.3	1.6
	8	51.4	11.7	1.1
30s	2	50.9	2.1	2.7
	3	53.1	5.7	2.1
	5	53.6	9.8	1.4
	8	53.1	9.4	1.1
60s	2	51.2	4.0	2.6
	3	52.4	7.4	2.1
	5	53.0	11.3	1.4
	8	52.4	10.6	1.1
600s	2	51.3	6.0	2.6
	3	50.8	9.7	2.0
	5	50.7	13.0	1.4
	8	50.4	11.9	1.1

Table 3.2. PALS characterization of Zirkon LK2200 films after different time plasma treatment.

Referring to the data in table 3.1 and 3.2, the intensities of Ps in the vacuum of the PT films are also plotted in figure 3.1. As illustrated in figure 3.1, all the processed films present a similar intensity of Ps in vacuum as the Si-capped film, which is much lower than the Ps intensity of non-processed porous film. This indicates that there is only backscattered Ps in the vacuum in the PT films. Hence, the pores in these porous MSQ-based films have been sealed off after plasma treatment [45]. The densified layers formed on the surfaces perform effectively as a diffusion barrier to Ps.

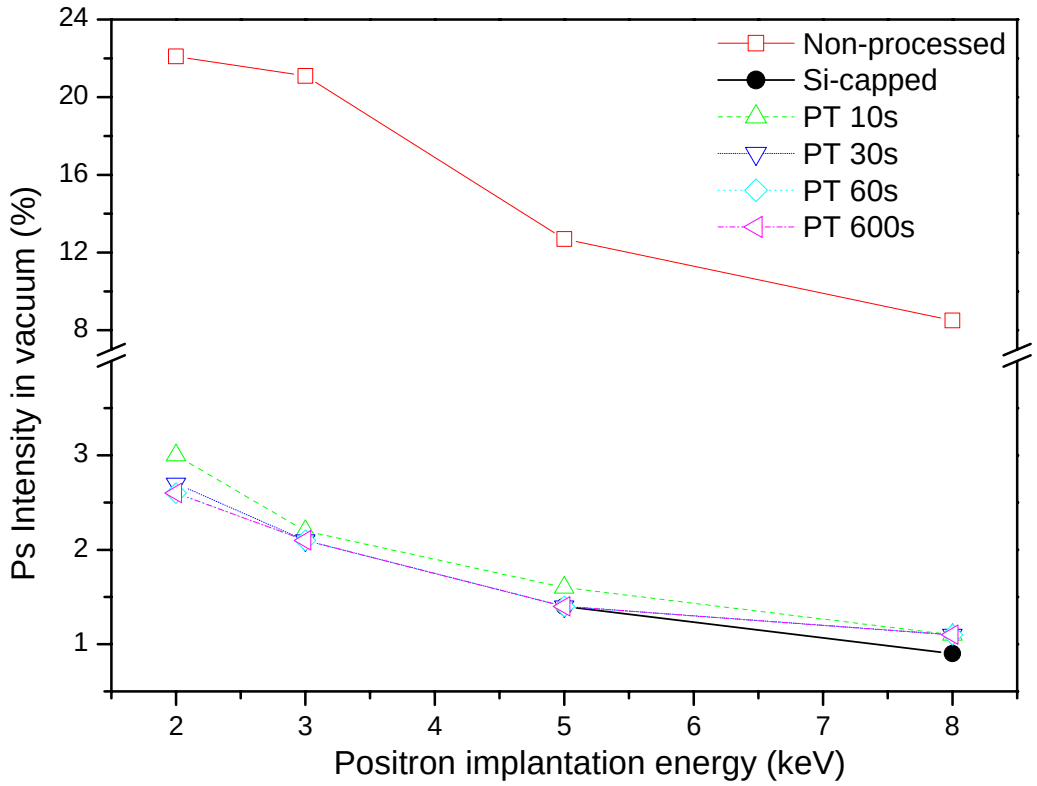

Figure 3.1. Ps vacuum intensity in the PT films. A pair of unprocessed porous and Si-capped porous films is examined for comparison.

SIMS has also been used to characterize the depth profiles of carbon and CN in the plasma treated low-*k* samples. Referring to the SIMS depth profile of carbon species (fig 3.2), carbon depletion occurred after NH_3 plasma treatment, with the depletion width of 10nm, 21nm, 56nm, 134nm and 252nm, respectively after different PT processing. The carbon depletion depth increases with prolonged plasma treatment time. Figure 3.3 shows the CN depth profile of non-processed and PT samples. According to the figure, CN concentration apparently increases in the low-*k* samples after plasma treatment, with the depth of 70nm, 95nm, 150nm and 320nm after 10s, 30s, 60s and 600s PT, respectively. Based on the PALS and SIMS characterization results, it is observed that densified layers formed after NH_3 plasma treatment, with

the formation of ultra thin carbon depletion layers on the surface of the porous low-*k* films.

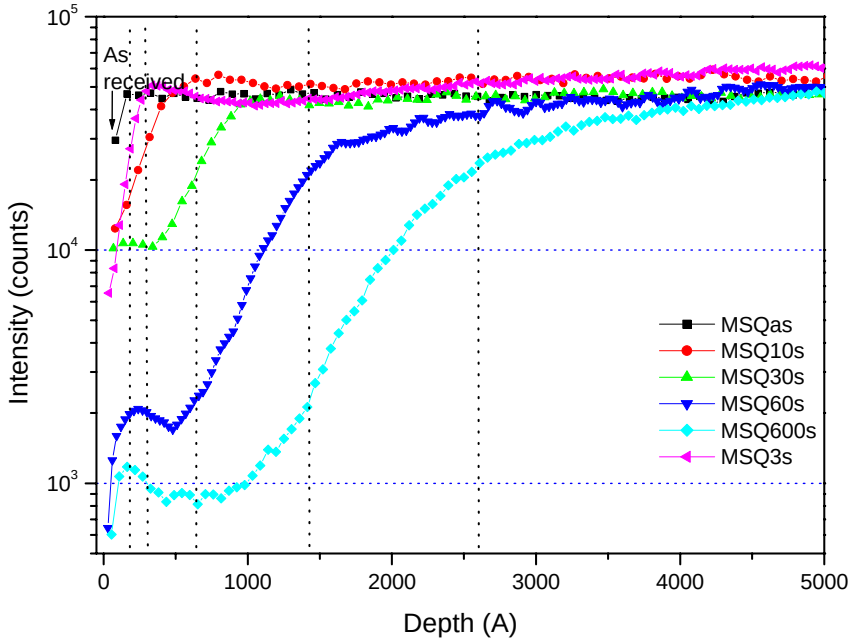

Figure 3.2. Carbon depth profile of non-processed and PT low-*k* samples.

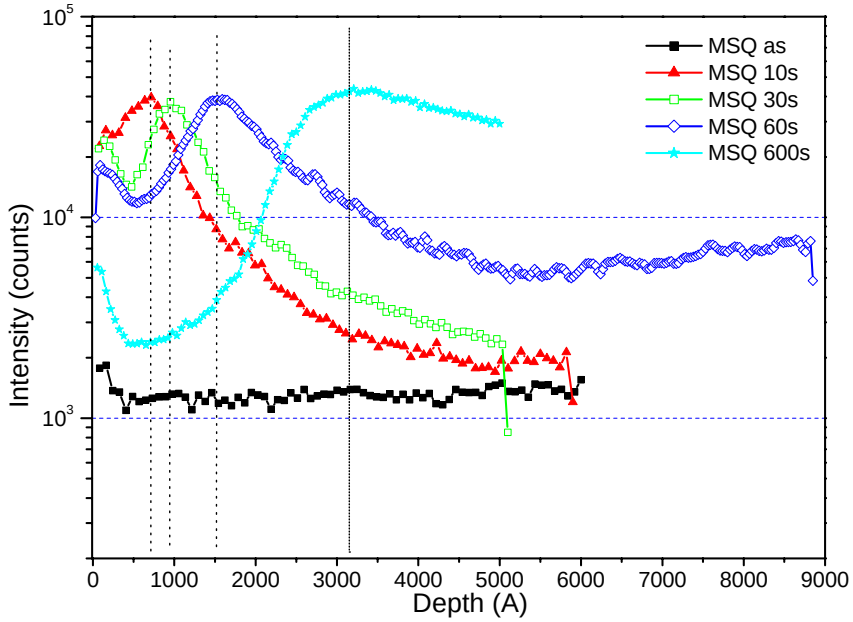

Figure 3.3. CN depth profile of non-processed and PT low-*k* samples.

Referring to the profiling data, long time plasma treatment (600s) is not applicable for the porous low-*k* film treatment because it would affect the property of the entire film.

3.3.2. Chemical composition characterization

FTIR and Raman spectroscopy have been employed to evaluate the chemical composition of the Zirkon films before and after plasma treatment.

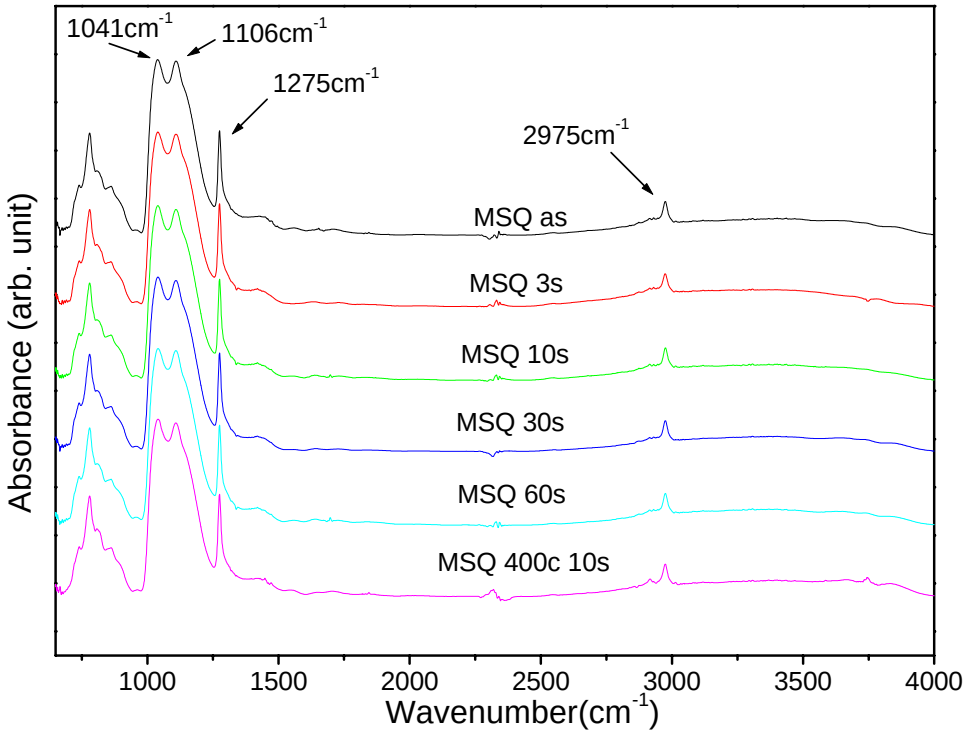

Figure 3.4. FTIR spectrums of Zirkon 2200 after different PT processes.

Figure 3.4 shows Fourier-transform infrared absorption spectra (FTIR) of the MSQ films before and after a series of NH_3 plasma treatment. As shown in the spectra, the peak at 1275cm^{-1} is attributed to Si-CH_3 stretching, the peak at 1106cm^{-1} is assigned to large angle Si-O-Si bonds in a cage structure and the peak at 1041cm^{-1} is

assigned to the stretching of smaller Si-O-Si bonds in a network structure [46-48]. It can be inferred from the FTIR measurements that the basic chemical structure of the Zirkon low-*k* material is the hybrid of the large angle and small angle Si-O-Si bonds. After the plasma treatment process, the FTIR spectra of Zirkon film did not vary from before the plasma treatment. Based on the calculation of the peak area in figure 3.4, the peak intensity of Si-CH_3 stretching has only been slightly reduced after different time plasma treatment, as illustrated in figure 3.5. The figure highlights that the ratio of the peak area (I_{Si-O}/I_{Si-CH3}) was only slightly increased from 2.17 to 2.28 after 60 s PT processing. However, a very small absorption peak at around 3500cm^{-1} is observed in the spectrum of the Zirkon film after 10s plasma treatment at 400^{o}C and the peak is assigned to Si-OH stretching. In the PT processing at 400^{o}C, plasma damage probably caused decomposition of the Si-C bonds, this induced the formation of a small fraction Si dangling bonds which absorbed moisture from air to form Si-OH bonds.

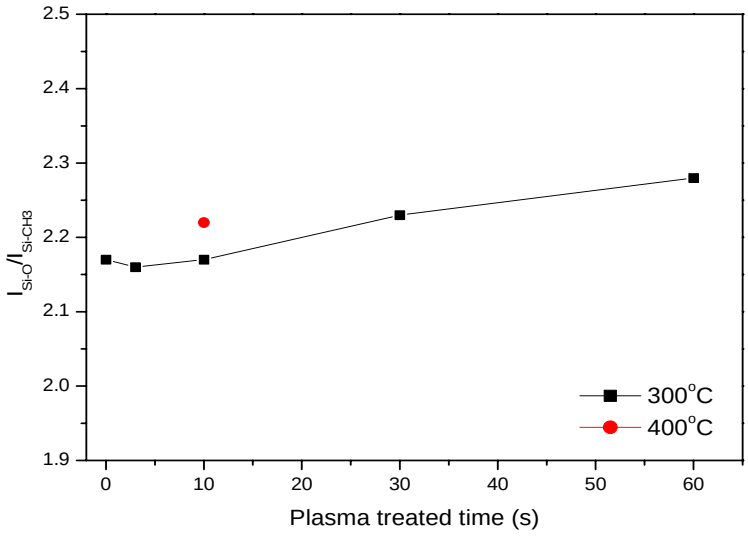

Figure 3.5. FTIR Peak area ratio of I_{Si-O}/I_{Si-CH3} of Zirkon films after different plasma treatments.

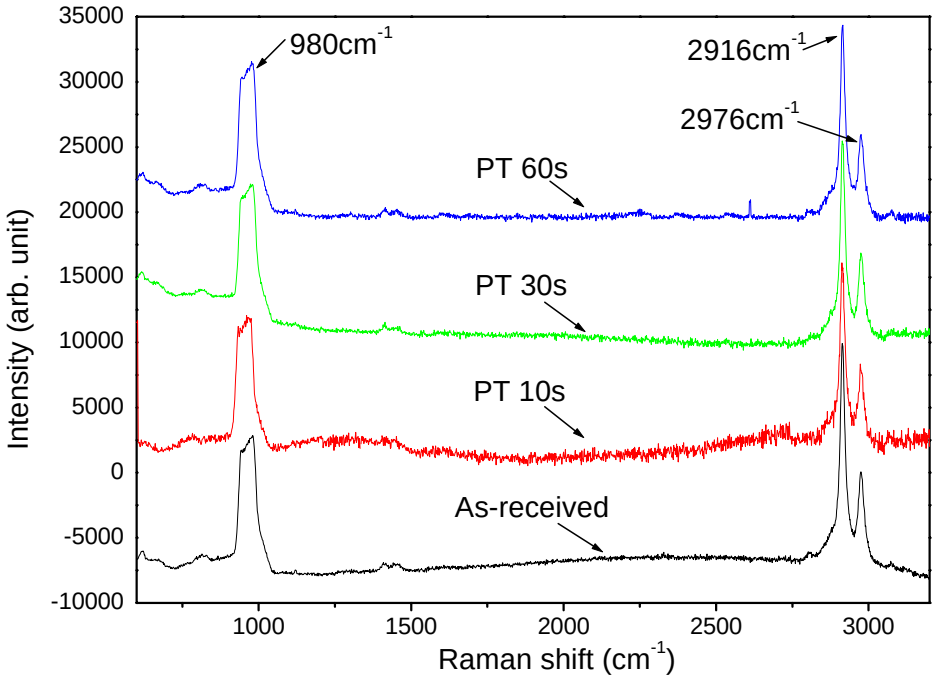

	MSQ as	PT 10s	PT 30s	PT 60s
I_{C-H}/I_{Si-O}	1.56	1.45	1.46	1.25

Figure 3.6. Raman spectroscopy of non-processed and plasma treated low-*k* films.

Raman spectroscopy was also used to characterize the change in chemical composition after plasma treatment because of the high sensitivity to C-H stretching. The peak at 980cm^{-1} in figure 3.6 is associated with the Si substrate [49]. Figure 3.6 also shows two peaks at 2916cm^{-1} and 2976cm^{-1} attributable to C-H symmetric and asymmetric stretches. Comparing the peak intensity ratio of C-H stretching to Si-O bending, the ratio of the peak intensity also slightly decreased from 1.56 to 1.46 after the short time plasma treatment, and this also helped to confirm the carbon depletion after NH_3 plasma treatment.

3.3.3. Morphology Characterization

Both AFM and TEM have been used to characterize the surface morphology and cross-section morphology of the low-*k* materials after plasma treatment. As shown in figure 3.7, the mean surface roughness of the Zirkon films decreased from 0.866 nm to 0.514 nm after 10s plasma treatment. However, the mean surface roughness was gradually increased with prolonged plasma treatment time and the mean film roughness was about 1.127nm after 600s plasma processing, which is even much higher than that of the unprocessed film. According to the AFM results, short time (less than 60s) plasma treatment reduces the surface roughness and increases the compatibility of the low-*k* films in the back-end of line technology. Prolonged plasma bombardment however will induce surface damage, resulting in much higher surface roughness.

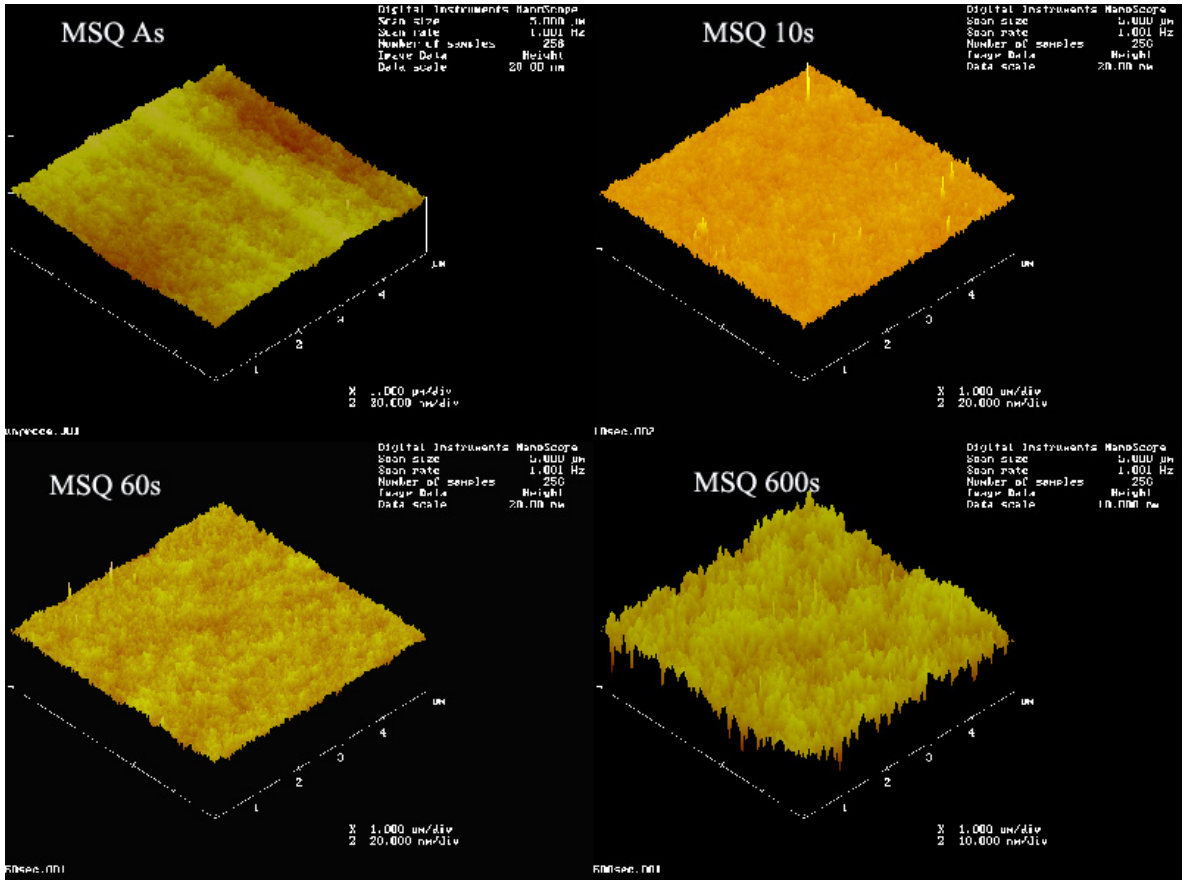

PT time (S)	0	10	60	600
Mean Roughness (nm)	0.866	0.514	0.543	1.127

Figure 3.7. AFM of unprocessed and PT processed Zirkon low-*k* films

Cross-sectional TEM identified the presence of a densified skin-layer on the surface of low-*k* materials after NH_3 plasma treatment. Figure 3.8 shows the cross-sectional TEM of the Zirkon low-*k* films after 3s, 10s, 30s and 60s NH_3 plasma treatment, respectively. Compared to the unprocessed porous films, the densified skin-layers have higher density; therefore there is a striking contrast between the surface layer and the under layer which are illustrated in the TEM figures of figure 3.8. The thickness of the densified skin-layer is 35 nm, 66 nm and 150 nm after 10 s, 30 s and 60 s plasma treatment, respectively.

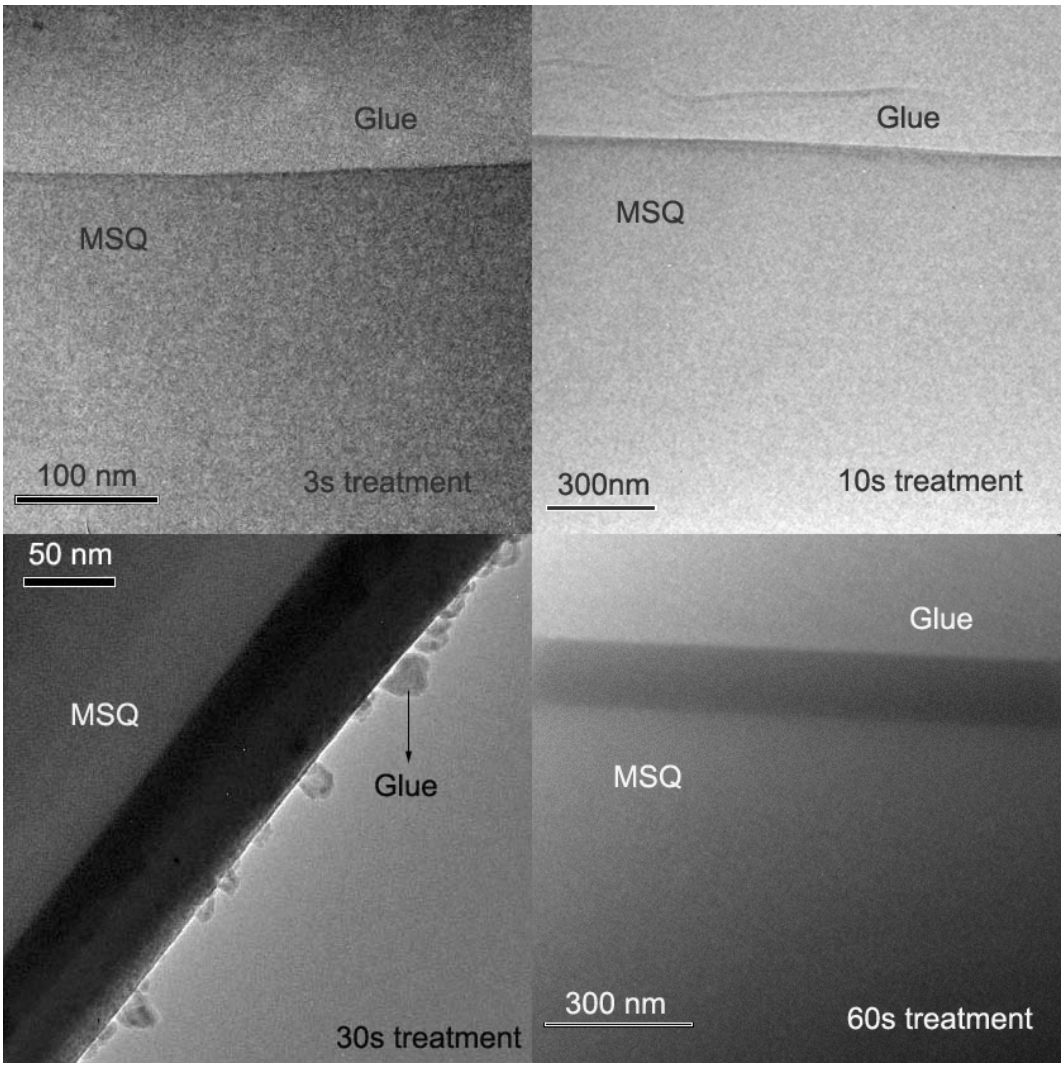

Figure 3.8. Cross-sectional TEM figures of processed Zirkon films

Based on the SIMS depth profile and the cross-sectional TEM data, a mechanism for the growth of the densified skin layer has been proposed, as shown in figure 3.9. After plasma generation, radicals and ions quickly diffuse into open meso-pores in the surface region and interact with the walls, causing the collapsing of the open nano-pores (less than 10 s). Because of the open nano-pores collapsing, there is one thin layer with almost no pores (so called densified layer) formed on the surface. After the formation of the densified layer, radicals and ions continuously diffuse through the

skin layer to form a carbon-depleted layer with properties different to the skin layer. After prolonged plasma treatment (several minutes), the thickness of the carbon depletion layer and the densified layer dramatically increased.

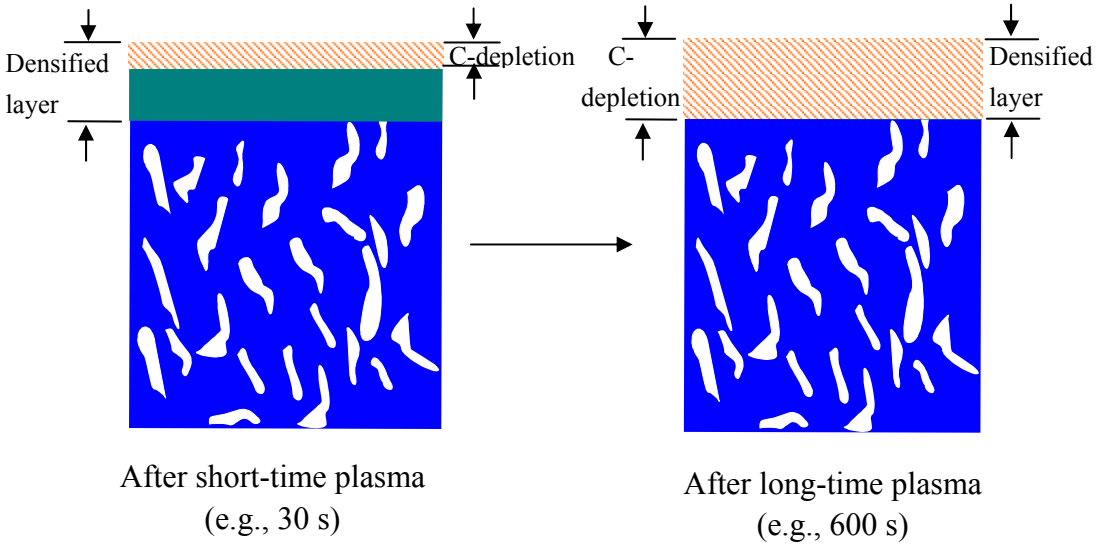

Figure 3.9. Proposed mechanism of Plasma treatment on the porous low-*k* film

3.3.4. Beneficial effect against Cu diffusion

To evaluate the properties of the densified skin layer as Cu diffusion layer, 150 nm Cu was deposited on the plasma-treated low-*k* films to form the Cu/LKD/Si stack. After 1 hour of thermal annealing at 400^{o}C, the surface Cu films were etched away by 26% $(NH_4)_2S_2O_8$ solution to prevent the knock-on effect in subsequent SIMS measurement.

As shown in SIMS depth profile of the as-received MSQ/Cu stack, the Cu intensity near the surface is very low since the Cu has been etched away by the $(NH_4)_2S_2O_8$ solution penetrating through the open pores on the film surface. However, the signal-to-noise intensity of the Cu is still higher than 10 in the depth of ~550nm,

which indicates that Cu has diffused into the porous low-*k* film after the thermal annealing. Compared to the depth profile of Cu/MSQ (as-received) stack, the Cu intensity are much higher on the film surface and the intensity decreases rapidly at greater depths, highlighting that the densified skin-layer effectively blocked the Cu during the thermal annealing. The long tail of the Cu depth with an intensity of lower than 10 is due to the limit of SIMS intensity resolution. The high intensity of copper on the surface of the PT films also indicates that the surface densified layer effectively prevented the chemical solution from penetrating into the porous film. Based on the SIMS results, the nitridation layers in the densified surface have enhanced the resistance of the post-PT Zirkon films to copper penetration.

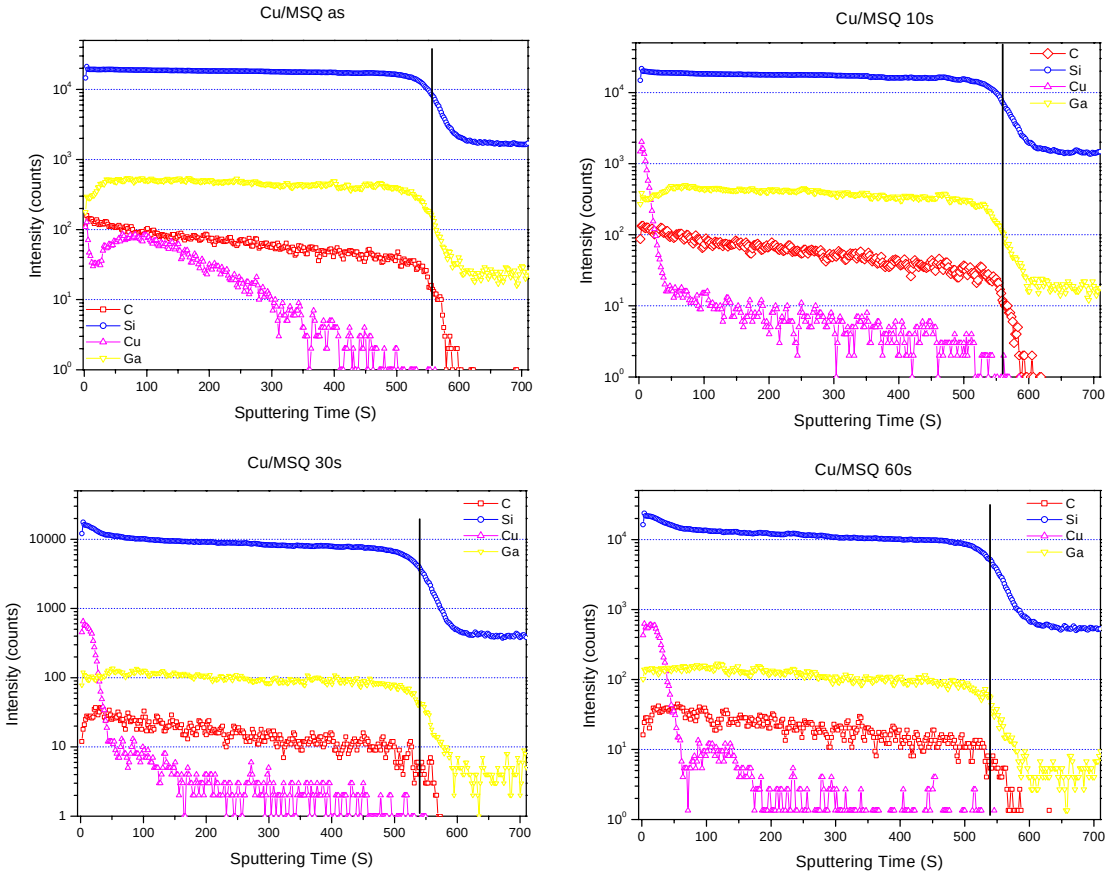

Figure 3.10. SIMS depth profile of Cu/MSQ/Si stack after 1 hour thermal annealing at 400°C in N_2 ambient.

3.3.5. Zirkon LK2200 Film Trench Patterning

In the Cu-Damascene scheme for forming interconnects, dielectric trenches are patterned first, followed by Cu deposition and CMP polishing. Successful integration requires optimization of low-*k* dielectric films with lithography and etch. To examine the process compatibility of the porous Zirkon low-*k* films, we have performed trench patterning on the low-*k* films using standard contact photolithography steps with Argon-CF_4 as the etching gas. An etch rate of about 140 nm/min could be achieved. Figure 3.11 shows successful trench formation for the porous low-*k* films indicating that the MSQ-based low-*k* material is suitable for back-end processing.

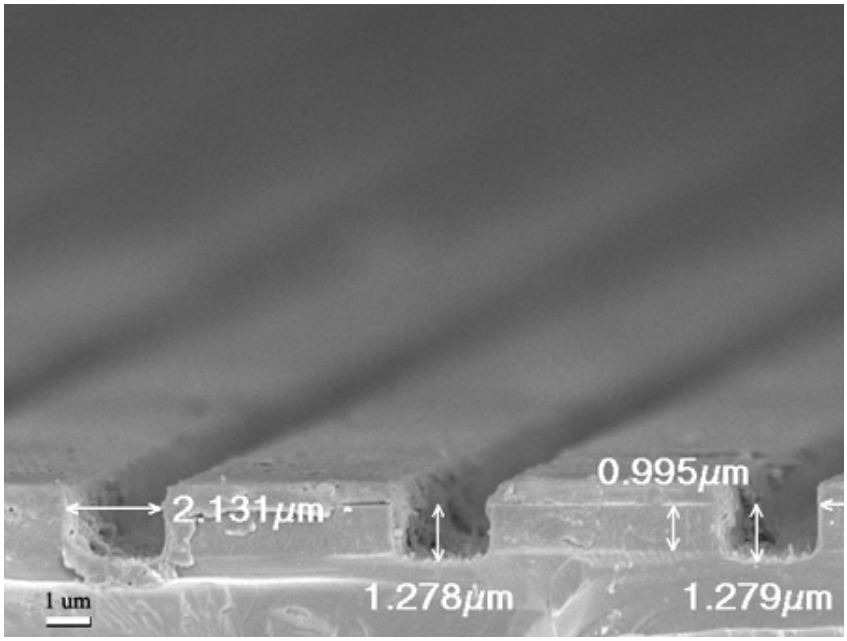

Figure 3.11. Cross-section SEM of the Zirkon film after RIE etching.

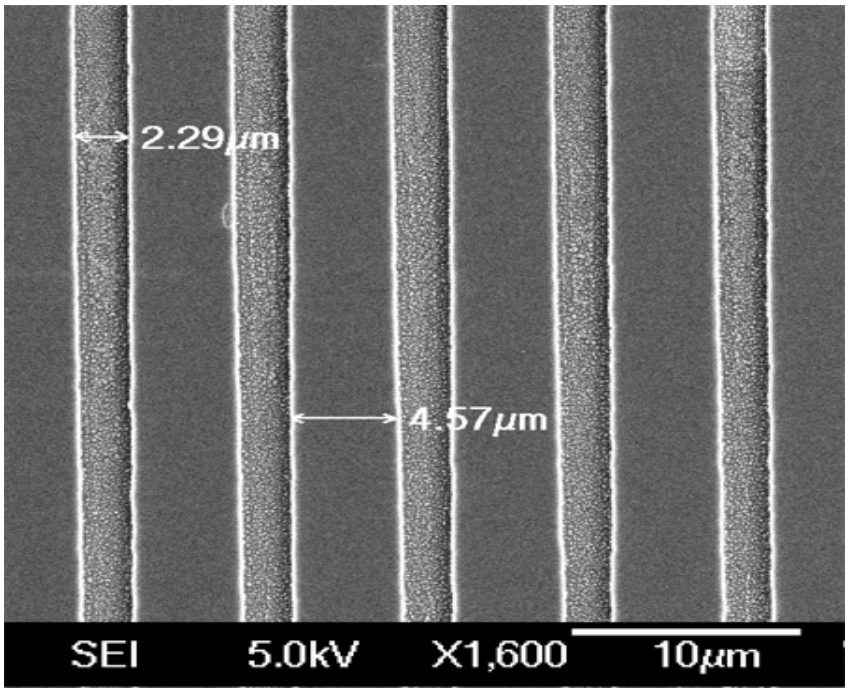

Figure 3.12. SEM of the MSQ surface after Plasma Etching.

Figure 3.12 shows the surface of the low-*k* films after RIE etching, the trench width is about 2.3 μm, which is exactly as designed.

3.4. Conclusion

In this chapter, porous low-*k* film based on Zirkon LK2200 has been successfully sealed by ammonia plasma treatment. A densified skin layer of 35 nm could be formed on the surface after ten seconds of plasma treatment, which could act effectively as copper diffusion layer.

The porous low-*k* films have also been trench patterned by using RIE etching, indicating the process compatibility of the Zirkon materials.

CHAPTER 4

FORMING IN-SITU Cu DIFFUSION BARRIER BY NH_3 PLASMA TREATMENT ON LKD POROUS LOW-K MATERIAL

In chapter 3, low frequency NH_3 plasma treatment has been found to be effective in sealing the porous Zirkon LK2200 film. In this work, we extend this study to another kind of porous low-*k* film, i.e., LKD5109 MSQ film from JSR.

4.1. Introduction

To reduce the resistance-capacitance (RC) delay time as ICs feature size scales down, the current leading candidate for the metal is Cu, and porous methyl silsesquioxane (MSQ) for dielectric insulator. However, the diffusivity of copper in porous MSQ is very high and the copper diffusion will cause dielectric failure and lead to significantly increased leakage current [54]. Therefore, an effective barrier layer is needed to prevent copper diffusion into the porous dielectrics.

As reported in chapter 3, densified layer will be formed on the surface of the *microporous* MSQ film after certain plasma treatment [32, 53]. A number of studies

have been done on the NH_3 plasma treatment of HSQ/MSQ nonporous low-k materials as well. For the NH_3 based plasma treatment, after the plasma treatment, a thin nitrided layer typically forms on the surface of the HSQ and it can act as an effective diffusion barrier for Cu/HSQ integration [50-52].

In this chapter, low-frequency NH_3 plasma treatment was applied to see if a NH_3 plasma treatment can have a similar effect on porous MSQ low film, more precisely on JSR's LKD5109 film. It is hoped that the NH_3 plasma-treated IMD film can exhibit a sufficient thermal stability against Cu diffusion, which would preclude the need to deposit additional diffusion barrier layer and therefore reduce the complexity of the back-end processes.

4.2. Experimental Section

In chapter 4, we carried out our study on a kind of MSQ-based *mesoporous* low dielectric constant (k = 2.2) material LKD5109, which was provided by JSR Corporation.

The process steps used in this work are as follows:

1. LKD solution was spun on silicon (p type) substrate. After 60s pre-baking at 80^{o}C, the wafer was soft-baked for 60s at 200^{o}C and was cured for 30min at 420^{o}C (N_2 ambient). The film thickness of LKD5109 was about 400nm.
2. To characterize the thermal stability, LKD film was annealed for 1 hour at 300^{o}C, 400^{o}C, 500^{o}C and 600^{o}C, respectively. 100 nm Cu was then deposited on the

samples exposed to thermal stress by using a shadow mask (area=1mm^2) in PVD sputtering system. Then the relative dielectric constant was measured by capacitance-voltage measurement (C-V).

3. In another set of samples, the low-*k* films were treated with NH_3 plasma in low-frequency plasma enhanced chemical vapor deposition (PECVD) system for varying plasma time with processing parameters of 300^{o}C substrate temperature, 300 mTorr work pressure, 100 SCCM NH_3 flow rate , and 150 W plasma power.
4. A 200nm thick Au film was deposited on the plasma-treated samples by PVD sputtering to form a metal-oxide-semiconductor (MOS) capacitor structure. The dielectric constant after plasma treatment was then evaluated by C-V measurement.
5. A 150 nm thick Cu film was deposited on the different samples (plasma treated and non-plasma treated samples) by PVD sputtering deposition. The diffusivity of Cu in the porous low-*k* film was evaluated by leakage current measurement and TOF-SIMS on Cu/LKD/Si stack after 1 hour thermal annealing in N_2 ambient at 400^{o}C.
6. Fourier Transform Infrared (FTIR) spectra, Raman spectroscopy and XPS were employed to characterize the chemical structure of the porous low-k films before and after NH_3 plasma treatment for different lengths of time.

4.3. Result and discussion

4.3.1. Thermal Stability of LKD 5109

Figure 4.1 compares FTIR spectra of LKD5109 films before and after thermal stress treatment. In the FTIR spectra, the absorption band at 778cm^{-1} is due to the Si-CH_3 vibration [47], the IR absorption band at 1277cm^{-1} is due to Si-CH_3 stretching and the peak at 2980cm^{-1} is due to C-H stretching in CH_3 group [55, 56]. It can be seen in Fig. 4.1 that, after one hour thermal stressing at temperatures of 500 ^{o}C or below, the peak intensity at 778cm^{-1} basically remained unchanged, while a noticeable reduction is observable after 600 ^{o}C annealing which indicates that the onset of a partial decomposition of Si-C bonds probably occurs at a temperature of around 600 ^{o}C.

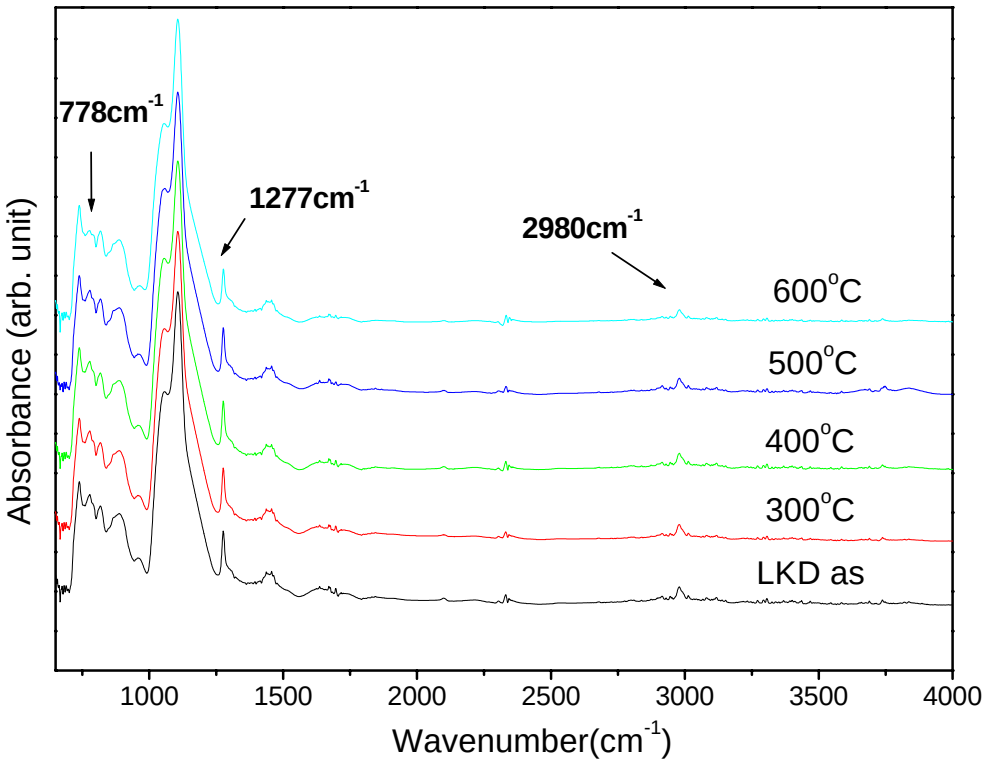

Figure 4.1. FTIR spectrum of LKD film after one hour thermal stress at 300 °C, 400 °C, 500 °C and 600 °C, respectively.

From the FTIR spectra, the peak area ratios of caged-like Si-O-Si stretching peak to Si-CH_3 stretching peak before and after different thermal stress have been deduced and plotted against annealing temperature in figure 4.2. The ratio was kept nearly unchanged up to 500°C, and then dramatically increased from 6.2 to 7.6 after thermal stress at 600°C. The Si-CH_3 bonds probably partially decomposed at 600°C, inducing the decrease in peak intensity. The intensity decrease of the peaks at 778cm^{-1} and 1277cm^{-1} only after a thermal treatment at 600 °C suggests that the chemical structure of the low-*k* films has basically remained unchanged up to 500 °C.

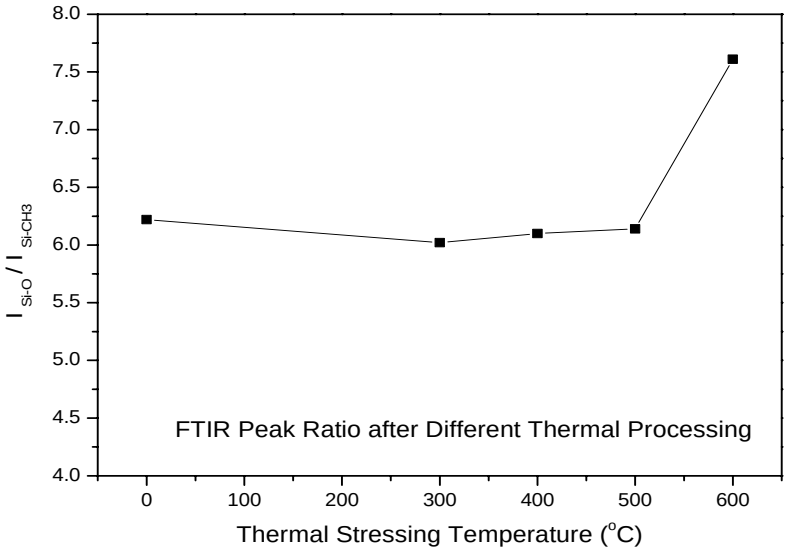

Figure 4.2. FTIR peak area ratio of Si-O-Si stretching peak to Si-CH_3 stretching peak after thermal stress.

On the other hand, the C-V measurement of LKD films has revealed only a slight increase in k value, from 2.2 to 2.4 after 500 ^oC annealing (see figure 4.3), implying a minimum chemical and structural changes up to 500 ^oC which is consistent with the FTIR result. The increase in the k value after 600 ^oC annealing is certainly due to the substantial change in chemical structure after the same temperature annealing as revealed by the FTIR measurement. Partially decomposed Si-CH_3 bonds after 600 ^oC annealing should be susceptible to moisture uptake once exposed to atmosphere [21]. Therefore, the potential processing temperature should be no higher than 500^oC for such low-*k* film.

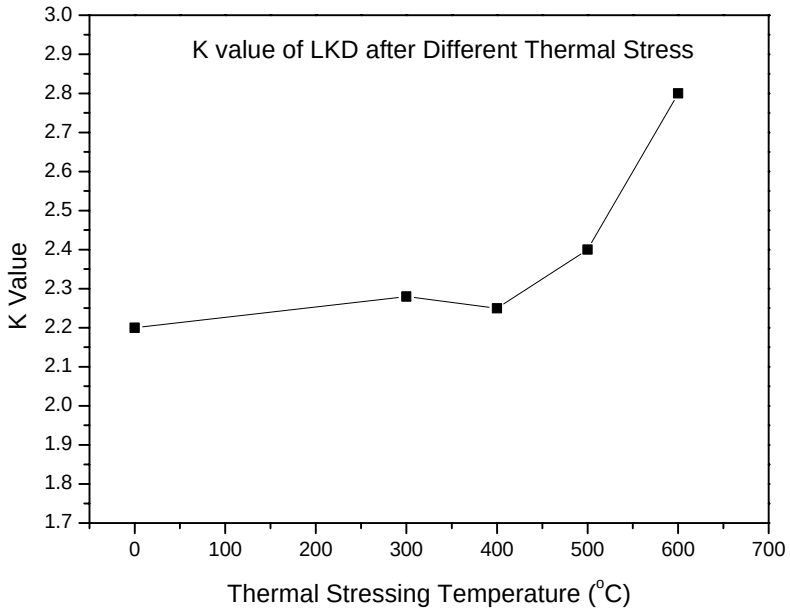

Figure 4.3. Relative dielectric constant of LKD before and after 1 hour thermal stress

Based on the results of FTIR and C-V measurement, we concluded that the chemical structure of LKD will be stable after one hour thermal stressing at a temperature lower than 500^{o}C, while a substantial thermal stress induced structural damage occurs at a higher temperature.

4.3.2. Characterization of the LKD chemical structure after Plasma Treatment

Chemical structure change of porous materials after plasma treatment has been evaluated by using FTIR, Raman Spectroscopy, X-ray photoelectron spectroscopy (XPS) and Secondary Ion Mass Spectroscopy (SIMS).

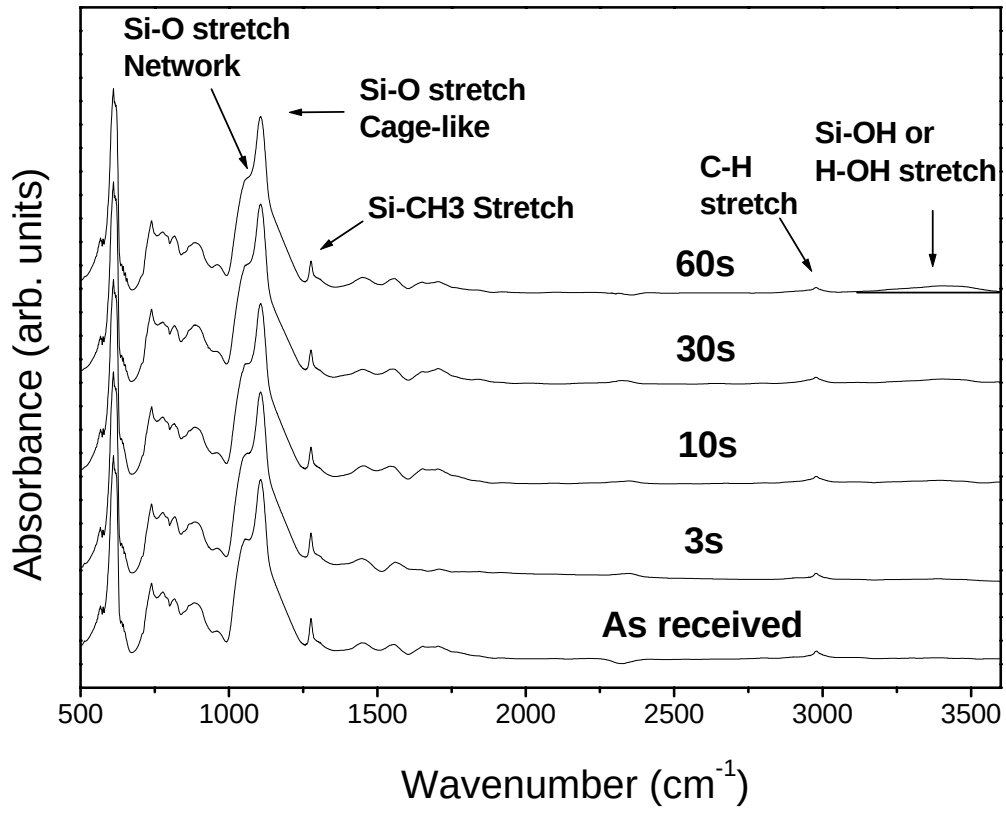

Figure 4.4. FTIR spectra for as-cured LKD film, 3s NH_3 plasma treated LKD film, 10s NH_3 plasma treated LKD film, 30s NH_3 plasma treated LKD film and 60s NH_3 plasma-treated film.

Figure 4.4 shows the Fourier-transform Infrared Absorption spectra (FTIR) of the LKD film before and after different periods of NH_3 plasma treatment. In the spectra, the peak at 815cm^{-1} is due to the Si-O bending mode in a network like structure [46], the peak at 1108cm^{-1} is related to large angle Si-O-Si bonds in a cage like structure and the peak at 1056cm^{-1} is from the stretching of smaller Si-O-Si bonds in a network like structure. The peak at 1277cm^{-1} is attributed to Si-CH_3 stretching, and the small absorption band at 2977cm^{-1} is attributed to C-H stretching in the CH_3 group [46-48, 57].

The intensity of the peak assigned to large angle Si-O-Si bonds is twice the peak intensity of the small angle Si-O-Si bonds, which suggests that the basic chemical structure of the LKD low-*k* film mainly consists of the large angle Si-O-Si bonds [57]. After the plasma treatment process, the FTIR spectra of LKD film remain almost unchanged. The peak intensity of Si-CH_3 stretching has just been slightly reduced after different time plasma treatment. However, a rather weak absorption band at around 3400cm^{-1} was observed in the spectrum of LKD after 60s plasma treatment and it was thought due to Si-OH stretching vibration, probably caused by the Si-CH_3 bonds decomposition by the prolonged plasma bombardment on the surface of the LKD low-*k* film.

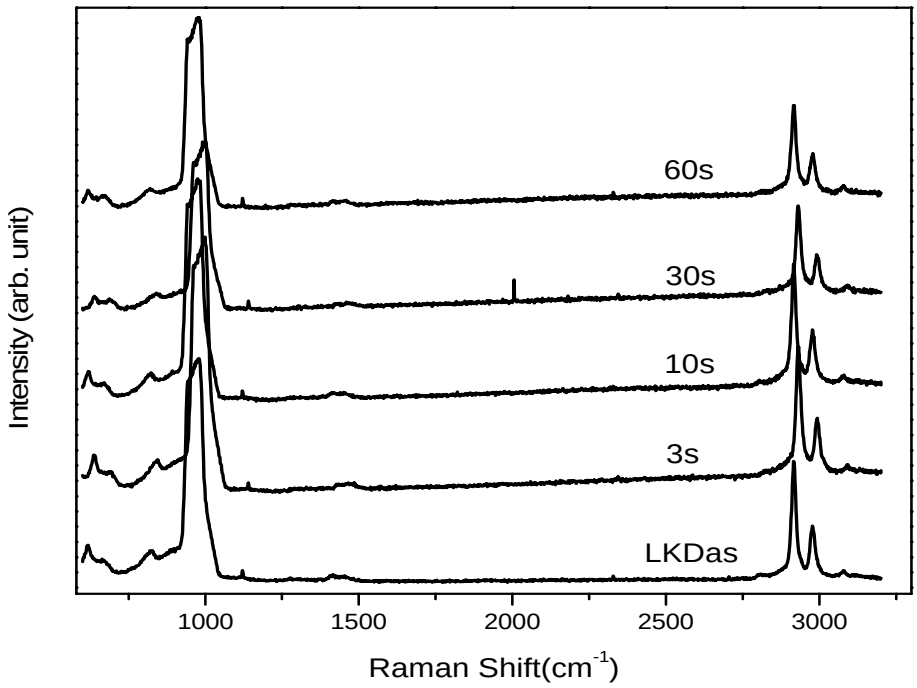

Figure 4.5. Raman spectra of as-received LKD and LKD after NH_3 plasma treatment for different times.

Being very sensitive to C-H stretching in the CH_3 group, Raman spectroscopy is employed to estimate the chemical composition of the LKD film after plasma treatment. In the spectra in figure 4.5, the two peaks at 2919cm^{-1} and 2979cm^{-1} are due to the C-H symmetric and asymmetric stretching vibrations respectively. As shown in the figure, the intensities of these two peaks slightly decreased after plasma treatment which suggests that slight carbon depletion happened after NH_3 plasma treatment.

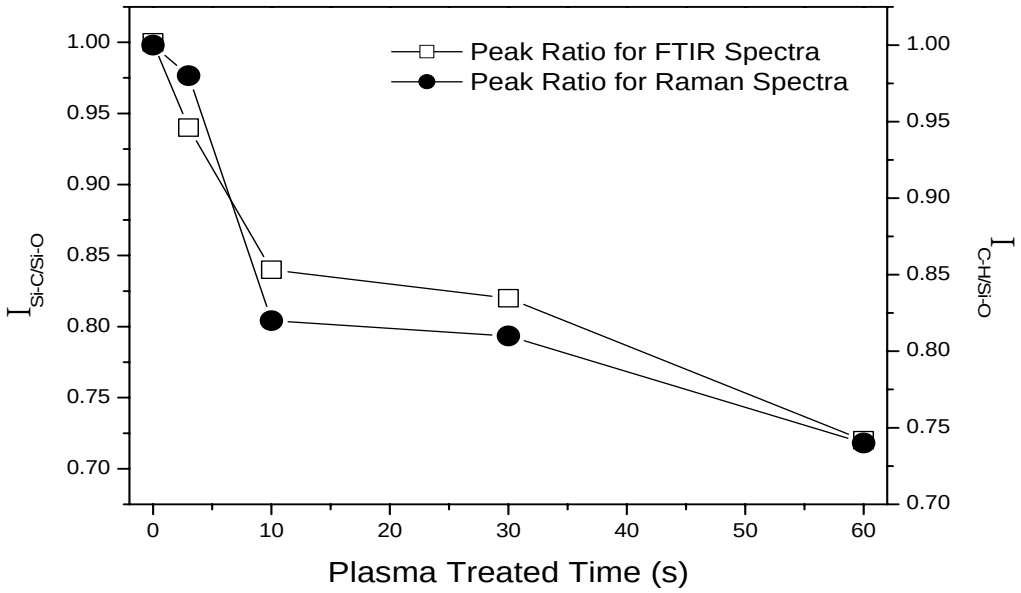

Figure 4.6. Si-C/Si-O peak ratios obtained from a series of FTIR spectra for as-cured LKD films receiving various time of plasma treatment. C-H/Si-O peak ratios obtained from a series of Raman spectra for as-cured LKD films after different time NH_3 plasma treatment. Note that the $I_{Si\text{-}C/Si\text{-}O}$ and $I_{C\text{-}H/Si\text{-}O}$ for as-cured films prior to any plasma treatments are used as standard and set at 1.

Referring to the FTIR and Raman spectra of the LKD samples after NH_3 plasma treatment, the ratio of the peak areas of Si-C/Si-O and C-H/Si-O has been seduced and

presented in figure 4.6. It is clearly shown in the figure that peak ratios of $I_{Si-C/Si-O}$ and $I_{C-H/Si-O}$ have been slightly reduced by less than 20% after 10s NH_3 plasma treatment and the ratios remained unchanged when plasma-treatment lasted for another 20s.

SIMS was also applied to characterize the change in chemical composition of the LKD5109 after NH_3 plasma treatment. Figure 4.7 (a) shows SIMS depth profile of the as-received LKD 5109, in which the CN and SiN (negative ions) signal intensity are nearly 100. Compared with the depth profiles shown in Figure 4.7a, the depth profiles of LKD samples after plasma treatment at (b) 30 s and (c) 60s show much higher CN and SiN signal intensities, with highest intensity on the film surfaces. The higher intensity of the CN and SiN signals at depth of about 250nm implies that the nitridation occurred not only on the surface, but also inside the porous film. This is due to the high ion flux and high diffusivity of chemically active radicals within the porous low-k film. The chemical structure in the deeper bulk regions can be altered through the reaction of these radicals with the matrix material during the plasma process. Similar to the observed C depletion in chapter 3, the carbon intensity also show a decrease on the LKD film surfaces after NH_3 plasma treatment, with the depletion widths of 60nm (for 30s plasma) and 90nm (for 60s plasma), respectively. The C depletion was caused by plasma bombardment on the surface of the porous films as well as by the chemical reaction of CH_3 with some chemically active radicals that diffused from the plasma into the low-k film. The observation of constant CN and SiN signal intensities within the C-depleted regions suggests that the C-depleted surface regions are in the form of SiN/SiOC≡N.

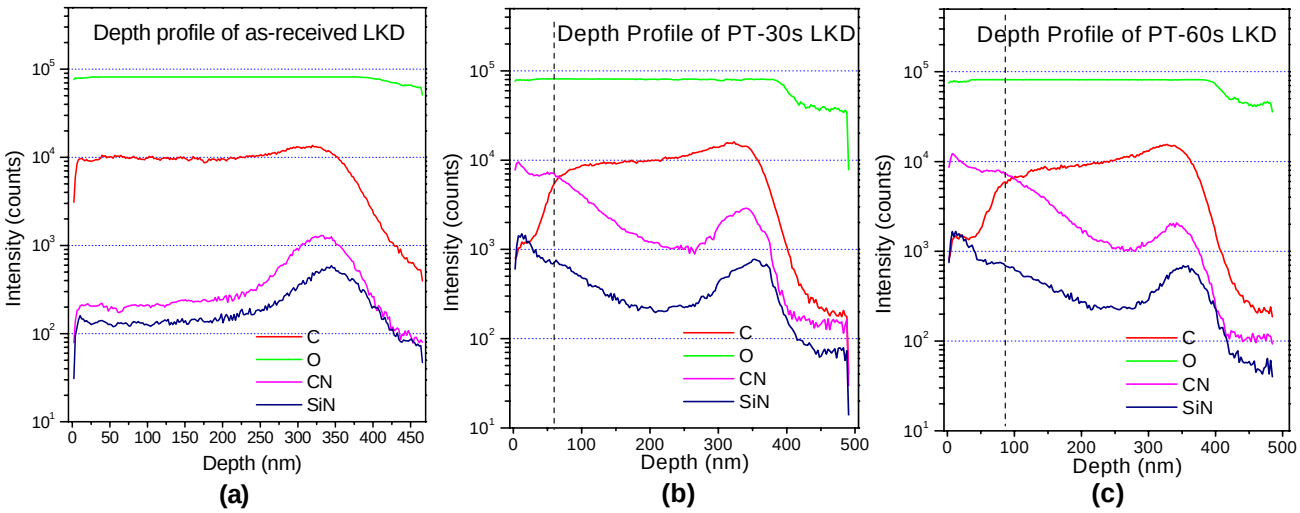

Figure 4.7. SIMS depth profiles of LKD films: (a) As-received LKD5109, (b) LKD after 30s NH_3 plasma treatment and (c) LKD after 60s NH3 plasma treatment.

Further evidence for the nitridation of the LKD film surface was also obtained from XPS analysis. To study profiles that are representative of the near surface regions, about 50Å thick surface layer was sputtered off from the plasma treated LKD films, which has the benefits of removing surface contaminations. Figure 4.8 shows the typical XPS spectra for N_{1S} in the NH_3 plasma treated LKD films, which confirms the presence of N on the surface [51].

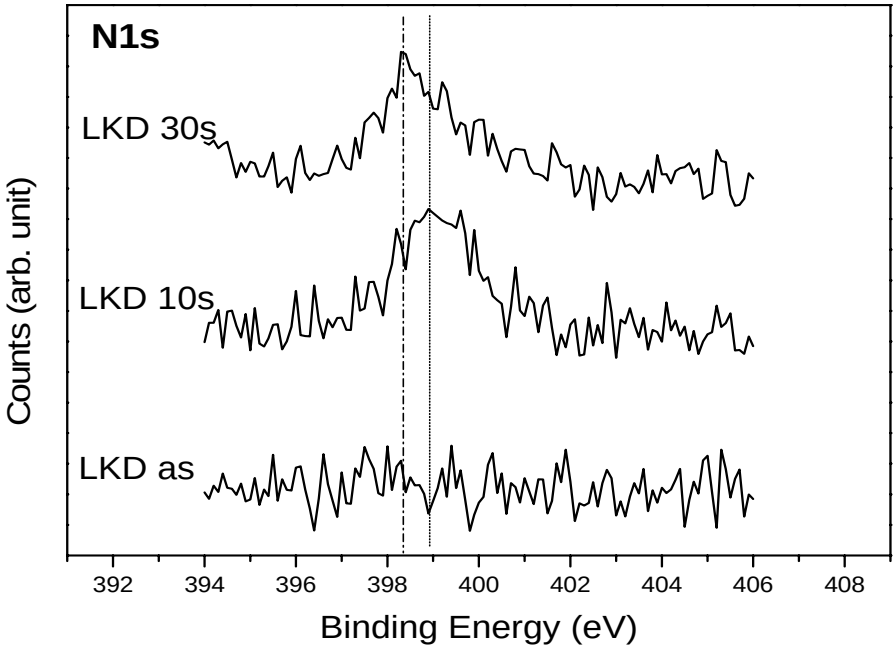

Figure 4.8. XPS spectra of N1s with and without NH_3 plasma treatment on LKD films.

4.3.3. Relative dielectric constant measurement

The dielectric constant of the LKD film was measured after a series of NH_3 plasma treatment to assess the processing compatibility of the low-frequency plasma treatment.

Capacitance-voltage (C-V) measurement has been used to characterize the *k* value of the LKD5109 before and after NH_3 plasma treatment. To eliminate system error, C-V measurement has been calibrated first using 1000Å thermal SiO_2 on Si substrate as the standard sample. As described in chapter 2, Au electrodes (with 200nm thickness) of 1 mm diameter were prepared on the surface of the standard SiO_2 together with the LKD films (including both plasma treated and non-plasma treated

films) using PVD sputtering deposition. To reduce the contact resistance, Au (200 nm thick) was also sputtered on the backside of Si to form backside Ohmic contact. Figure 4.9 shows the C-V curves of the standard SiO_2 sample with a *k* value of 3.9. 6 electrodes have been used to measure the accumulation capacitance and the mean value of the 6 measured capacitances has been used to calibrate the C-V measurement system.

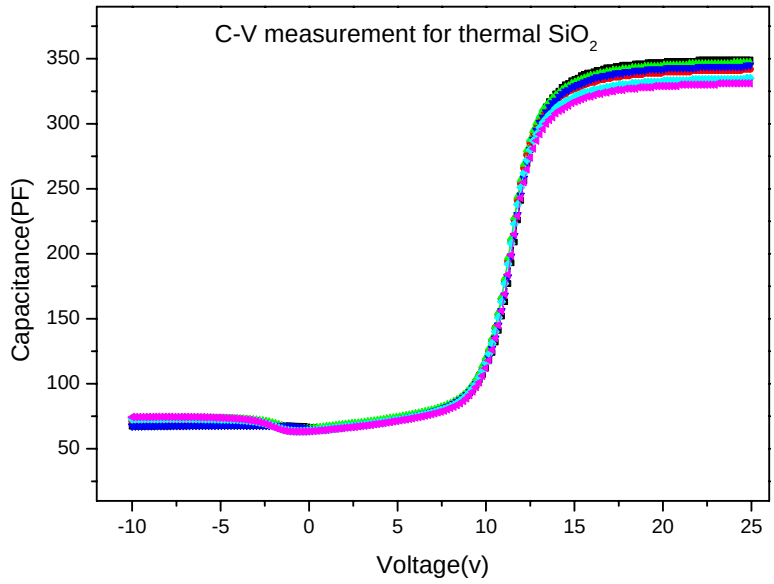

Figure 4.9. Capacitance-voltage curves of thermal SiO_2 for C-V measurement system calibration.

From the C-V curves, a mean accumulation capacitance C_{ox} of 341.5 PF is calculated. In this chapter ă is used as the correction factor for the C_{ox}. A correction factor value ă is obtained from $\breve{a} = \frac{A\varepsilon_0\varepsilon_r}{C_{ox}T_{ox}}$, where ε_r is the relative dielectric constant (k) of the SiO_2 at 300 K, **A** refers to the area of the electrode of the MIS structure and

T_{OX} represents thickness of the insulator. The factor ă is calculated to be 0.794 from ă = $A\varepsilon_0\varepsilon_r / (C_{ox}T_{ox}) = 8.854\times10^{-12}\times0.785\times10^{-6}\times3.9/(341.5\times10^{-12}\times1000\times10^{-10}) = 0.794$

Figure 4.10 shows the C-V curves measured on the plasma treated and non-plasma treated LKD films. Based on the theory of the C-V measurement, the Cox is equal to the accumulative capacitance of the MOS capacitor. As shown in the C-V curves, the accumulative capacitance is the maximum capacitance when the positive bias applied to the bias (P type Si). Three electrodes have been chosen to measure the C_{ox} for each sample and the relative dielectric constants of these films are calculated from the formula $\varepsilon_r = \frac{\tilde{a}_{ox} C_{ox} T_{ox}}{A\varepsilon_0}$. The dielectric constants of the different samples were illustrated in figure 4.11. As shown in this figure, the *k* value of the porous low-*k* films increased slightly after short time (less than 30s) NH_3 plasma treatment. However, the *k* value increased dramatically after 60s plasma treatment (increased to 2.83).

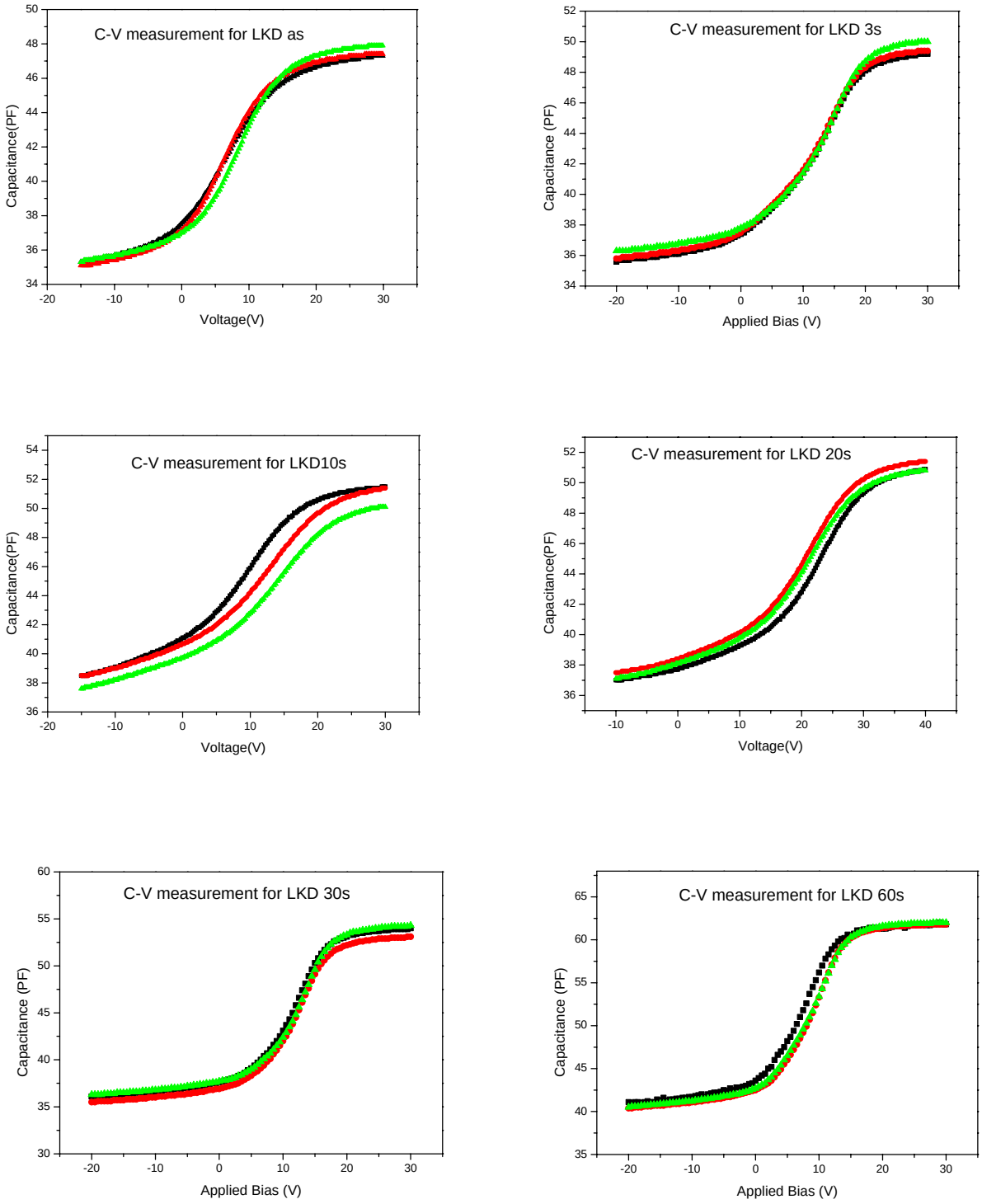

Figure 4.10. C-V curves of LKD thin films before and after plasma treatment.

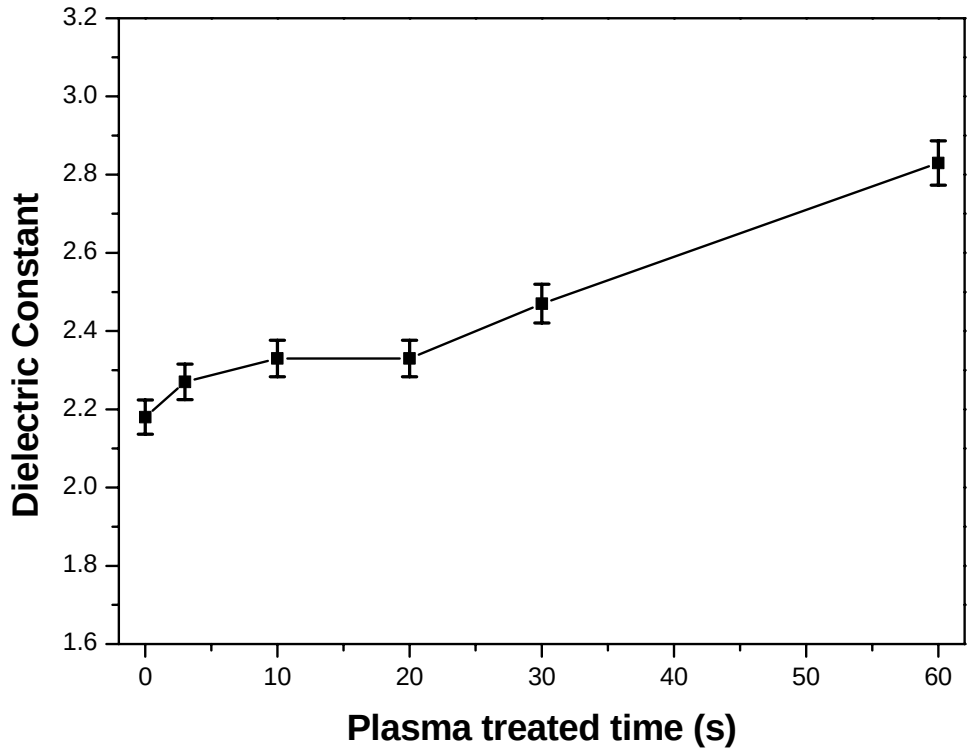

Figure 4.11. Relative dielectric constant of as-cured LKD film and LKD films subjected to different periods of plasma treatment time.

4.3.4. Evaluation of barrier performance of the plasma modified surface layer against Cu diffusion

I-V (current-voltage) measurement and SIMS have been used to evaluate the barrier performance of the plasma modified surface nitrided layer in the plasma-treated LKD films against copper diffusion.

By using PVD sputtering deposition, Cu has been deposited on the LKD films to form the Cu/LKD/Si structure. Leakage current density-voltage curves of the MIS stack have been measured with and without thermal stressing. Figure 4.12 shows the I-V curves of the LKD films with and without NH_3 plasma treatment before thermal

annealing. It is observed in figure 4.12 that the leakage current densities of the plasma-treated samples are lower than that of the as-received LKD low-*k* film. The leakage current densities of all the samples are still lower than 1×10^{-6} A/cm^2 at 40 V bias which means that dielectric breakdown didn't occur at electric field of 1MV/cm [50].

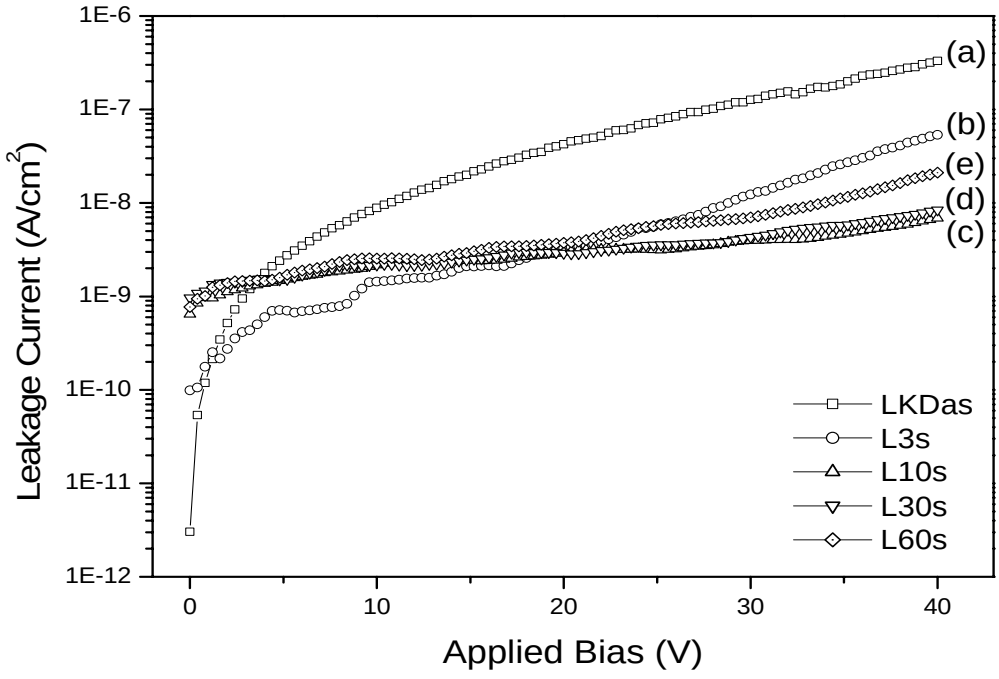

Fig 4.12. Leakage current density-voltage curves of Cu/LKD film/Si structure without thermal annealing, (a) to (e) representing the I-V curve of LKD as, PT 3s, PT 10s, PT 30s and PT 60s LKD, respectively (PT = plasma-treated).

Figure 4.13 illustrates the leakage current behavior of the NH_3 plasma-treated LKD films after subjecting to thermal stress at 400^{o}C. It is observed that the leakage current densities of the LKD samples after 30s PT or even longer did not change from that of the as-treated LKD samples. This suggests that the film surface nitridation had somehow suppressed copper diffusion. An increase of the leakage current densities of

short time (<10) PT samples is also represented in figure 4.13, which suggests that some Cu ions diffused into the porous film during the thermal stress process [58]. Compared to untreated film, an obvious reduction in leakage current density of approximately five orders of magnitude is observed for NH_3 plasma-treated samples (>30s). It is also shown in figure 4.13 that the current density decreased after prolonged NH_3 plasma treatment.

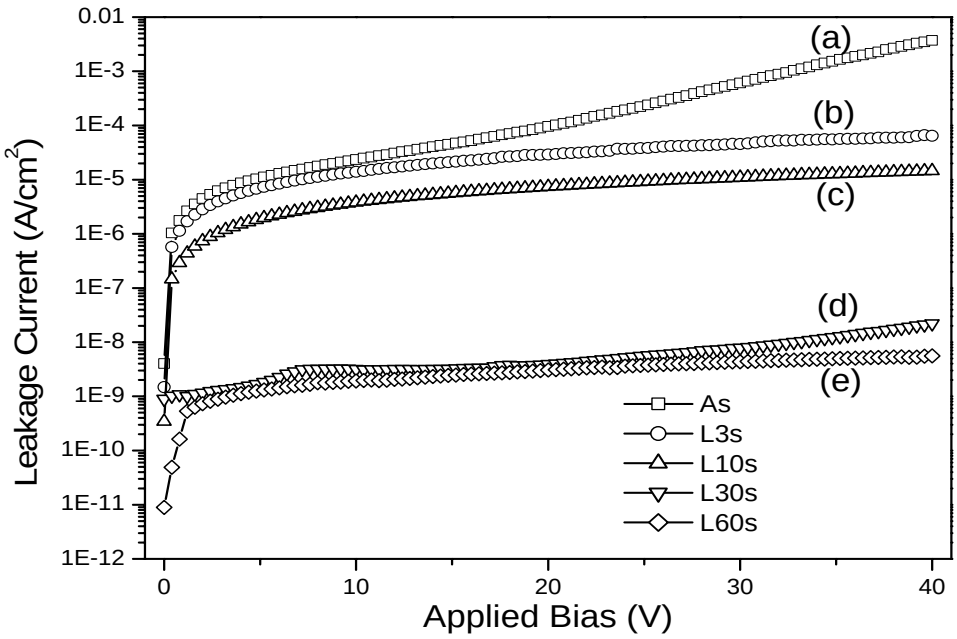

Fig 4.13. Leakage current density-voltage curves of Cu/LKD film/Si structure after 1 hour thermal annealing at 400^{o}C.

Based on the I-V data, we can conclude that NH_3 plasma treatment (>30s) on porous LKD samples appears to suppress the Cu diffusion in nanoporous films that were subjected to 400^{o}C stress for 1 hour as far as leakage current is concerned.

SIMS was also applied to evaluate the resistance of the PT LKD films against Cu penetration. Figure 4.14 represents the depth profiles of the Cu/As-received LKD/Si stack and the Cu/PT-60s LKD/Si stack after 1 hour thermal annealing at 400 ^{o}C in N_2 ambient. As shown in the figure, the Cu has diffused into the porous low-k film and even penetrated into the Si substrate. By contrast, the copper depth profile in the PT-60s LKD film decreases rapidly and shows shallower copper distribution, suggesting a substantially reduced Cu diffusion in plasma-treated film.

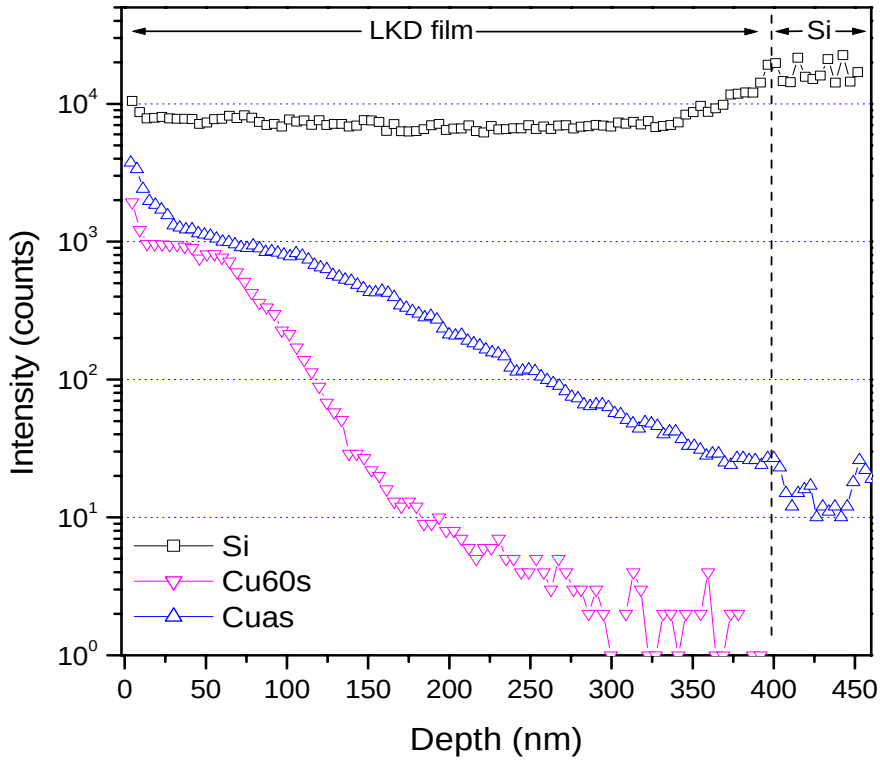

Figure 4.14. Secondary ion mass spectroscopy for as-cured LKD and LKD film after 60 s plasma treatment with Cu-electrode after being subjected to thermal stress at 400^{o}C for 1 hour

4.3.5 PALS Characterization

To evaluate the sealing performance of the PT process, 6 LKD films with varying amounts of plasma treatment and temperature are depth-profiled with 1, 3, and 5 keV positron beams. In Table 4.1, the depth-profiling PALS results are shown for an as-received 400 nm-thick control film of LKD-5109 with no plasma treatment. The long vacuum lifetimes of nearly 140 ns, and the large vacuum intensities, compared to the expected intensities from backscattering, indicate that the positronium atoms are freely diffusing into the vacuum through highly interconnected pores.

E (keV)	Mesopore Lifetime (ns)	Mesopore Intensity (%)	Ps Vacuum Lifetime (ns)	Ps Vacuum Intensity (%)	Ps Back Scattering (%)	Ps Total Formation (%)
1	28.0	1.8	130	29.8	7	25
2	17.2	1.6	133	28.5	3.5	26.5
3	16.5	2.3	135	25.7	2.5	25.5
5	19.3	1.7	138	19.2	1.8	19

Table 4.1 PALS Results for as-received 400 nm-thick LKD without PT process.

The varying mesopore lifetime with positron implant energy is another evidence that the mesopores in the LKD film is highly interconnected with a percolation length larger than the film thickness. To measure the true mesopore lifetime that can be correlated to the actual pore size, PALS measurements on Ta-capped LKD films were also performed and a mesopore lifetime of 51 ns (for both 5 nm and 20 nm Ta capping) that is independent of positron implant energy was obtained. From this lifetime value, it was estimated that the diameter of the cylindrical pores in the LKD film is about 2.8 nm.

It was found from PALS measurement that, unlike in the case of Zirkon LK2200 films, NH_3 plasma treatment does not completely seal surface pores for Ps out-diffusion as high Ps vacuum signal intensity as well as much shorter mesopore lifetimes (shorter than 51 ns observed in Ta capped films) were detected (see figures 4.15 and 4.16).

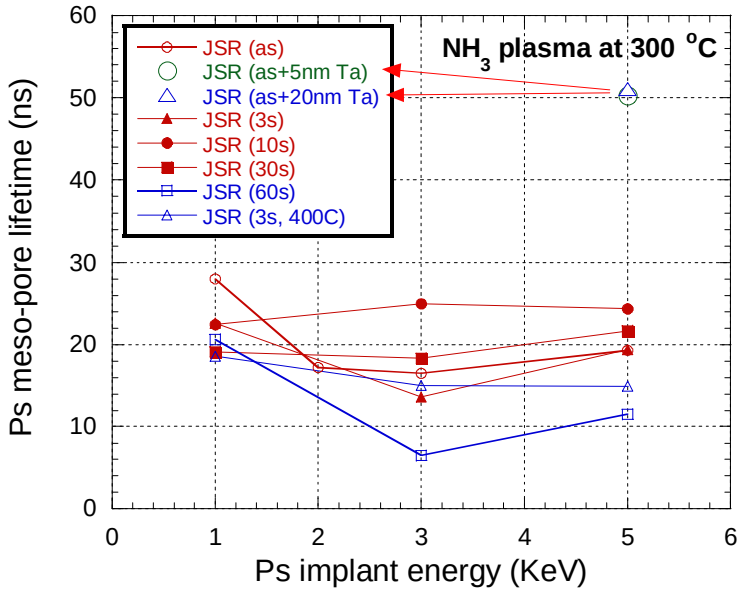

Figure 4.15. Ps mesopre lifetime vs. Ps implant energy in as-received and plasma-treated LKD films.

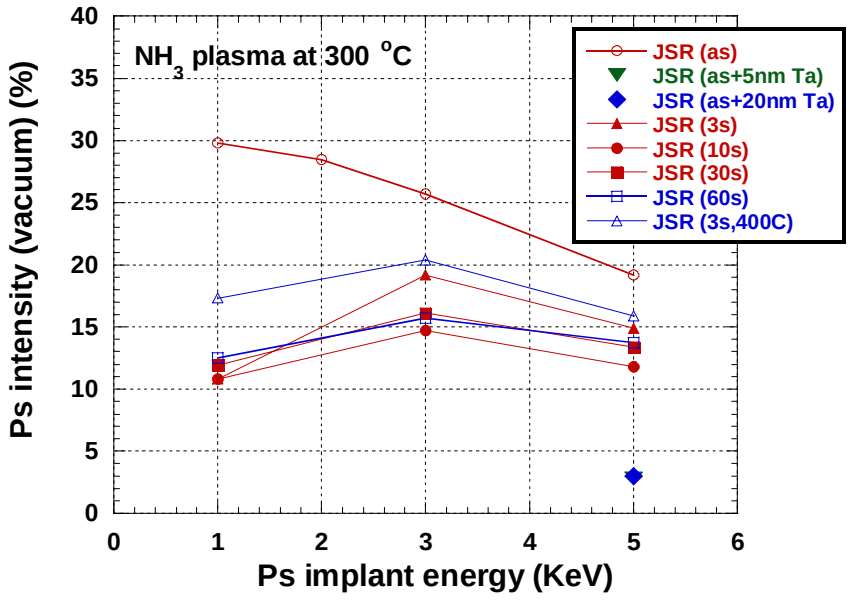

Figure 4.16. Ps vacuum signal intensity vs. Ps implant energy in as-received and plasma-treated LKD films.

Though the surface pores in the LKD films were not completely sealed by the NH_3 plasma treatment, it was revealed by PALS that substantial densification was indeed caused by the plasma treatment, thus explaining the previous observations made from I-V and SIMS measurement. To quantify the depth profile of the film densification and the closing of surface pores, the total amount of positronium (escaping and confined to pores, corrected for Ps backscattering) is compared between plasma-treated samples and the control film at each positron beam energy. It is noticed that for all the plasma-treated samples, the fraction of the densified pore decreases with the positron energy, and hence the implantation depth, is increased as shown in Fig 4.17. The plasma treatment appears to be most effective in collapsing pores roughly in the top 50-100 nm near the surface of the LKD films.

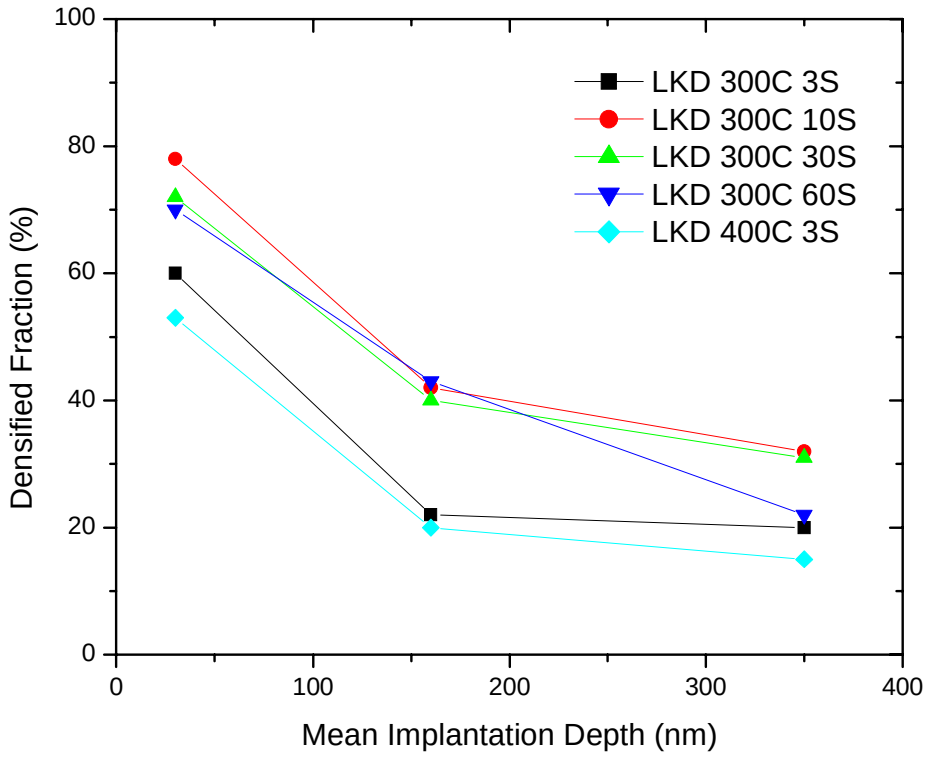

Figure 4.17. Fraction of densified pores as a function of positron implantation depth using energies of 1, 3 and 5 keV.

Using plasma treatments, a near-surface densification of open-pored LKD5109 films has been observed. However, no treatment conditions have been found that can seal the pores on the surface completely according to the PALS results.

4.4. Conclusion

Low-frequency NH_3 plasma treatment has been found to be effective in forming a thin densified nitride layer on LKD5109 and substantially enhanced its resistance to copper penetration.

However, results from the beam-PALS measurement suggests that NH_3 plasma treatment cannot completely seal the surface of the mesoporous LKD materials (as far as positronium out-diffusion is concerned), probably because of the highly interconnected porosity distribution of LKD5109. The unsealed structure will cause reliability issue in the back-end process. Judging from the results of the chemical and electrical characterization, the *k* value of the porous LKD film property is increased after NH_3 plasma treatment. Therefore, low-frequency NH_3 plasma treatment is not an attractive method to enhance the processing capability of LKD5109 low-*k* material.

CHAPTER 5

EVALUATION of PECVD DEPOSITED BORON NITRIDE as COPPER DIFFUSION BARRIER on POROUS LOW-*k* MATERIAL LKD5109

5.1. Introduction

Identifying a copper diffusion barrier on the nanoporous substrate is critical for the damascene fabrication process. In this study, we have evaluated the compatibility of plasma-deposited amorphous Boron Nitride film as copper diffusion barrier on LKD-5109 (from JSR, k = 2.2) [59]. LKD-5109 is a kind of MSQ (methylsilsesquioxane) based porous low dielectric constant material. The relative dielectric constant (k) of this film is about 2.2. Using postronium annihilation lifetime spectroscopy (PALS), the porosity and mean interconnected pore size were estimated to be about 30% and 2.7 nm. The thermal conductivity and specific gravity are 0.235 $W \cdot m^{-1} \cdot K^{-1}$ and 0.93 (with H_2O as the reference material).

Boron Nitride (BN) is a well known dielectric with high thermal conductivity, low thermal expansion, high electrical resistance and low dielectric constant and loss tangent, and with microwave transparency. The advantages of boron nitride are the mechanical, thermal and chemical stability so integration into IC manufacturing

process is possible. Although the dielectric constants of the films have been reported [49, 50], there are few studies on the incorporation of BN as a low-*k* material. Previously, Sugino and coworkers prepared amorphous BCN films on silicon at 650 °C using nitrogen and boron trichloride and reported a *k* value of 2.2 [62]. In other studies, they intentionally introduced methane as the carbon dopant and synthesized BCN films at 390°C and reported similarly low k values for the BCN films because amorphous regions formed in the *h*-BN film [63, 64]. In this work, we prepared BN films on nanoporous LKD films using the precursor borazine at 400°C. No carbon was intentionally introduced in order to study the intrinsic properties of the BN films. Both Microwave Plasma CVD (2.45 GHz) and Radio-frequency plasma atom beam deposition (13.56 MHz) were applied for the BN deposition in order to evaluate the compatibility of the two plasma processes with the nanoporous films. Growth parameters were optimized to minimize boron implantation and carbon depletion within the nanoporous substrate, which were found to have deleterious effects on the dielectric properties.

5.2. Experimental section

LKD5109 was spin-coated on p-doped Si (100) substrate. After 60 seconds of prebaking at 80^{o}C, the wafer was soft-baked for 60 seconds at 200 ^{o}C and was cured for 30 min at 420^{o}C (N2 ambient). A 400nm LKD film was obtained finally.

The microwave plasma-enhanced chemical vapor deposition (MWPECVD) process was carried out in a commercial reactor (AsTex). The substrate heating was

controlled by a RF-induction heater stage with water cooling, using the following substrate temperatures: 250 ^{o}C, 300 ^{o}C, 400 ^{o}C and 500 ^{o}C. The growth parameters used were typically: Microwave Plasma Power: 400 watts, Pressure: 20 Torr, flow rates of borazine, H_2 and N_2 were 5.0 sccm, 20sccm and 40sccm, respectively. Both porous low-*k* material (LKD5109, 400nm on Si 100) and silicon (100) wafer were used as the substrates.

A low pressure CVD route using a 13.56 MHz remote-discharged radiofrequency plasma beam source (Oxford Applied Research) was also applied to deposit *h*-BN on LKD. The remote-discharged atom beam source allows predominantly neutrals to effuse from a capillary dosing plate onto the sample, affording minimal ion beam damage of the sample. Due to the considerably lower pressure of the deposition, the gas feed was entirely borazine without the need to use carrier or diluting gas. Parameters: RF plasma power: 300 W, chamber pressure: 2.0×10^{-4} torr, substrate temperature: 400^{o}C.

The chemical composition of the BN on low-*k* material was characterized by FTIR and Raman spectroscopy. 1 mm^2 Au electrodes were electron beam-deposited onto the BN films to form a metal/insulator/semiconductor (MIS) structure of Au/BN/LKD/Si, as shown in figure 5.1. Capacitance-voltage (C-V) measurement was used to estimate the effective dielectric constant of the BN on low-k material and Si substrate. Standard 100 nm thermal SiO_2 was used for equipment calibration. The thickness of the BN was measured using surface profiler (KLA-Tencor) following depth profiling in secondary ion mass spectrometry (SIMS) and cross-section SEM.

SIMS was used to measure the changes in the elemental depth profile of boron and carbon after BN deposition.

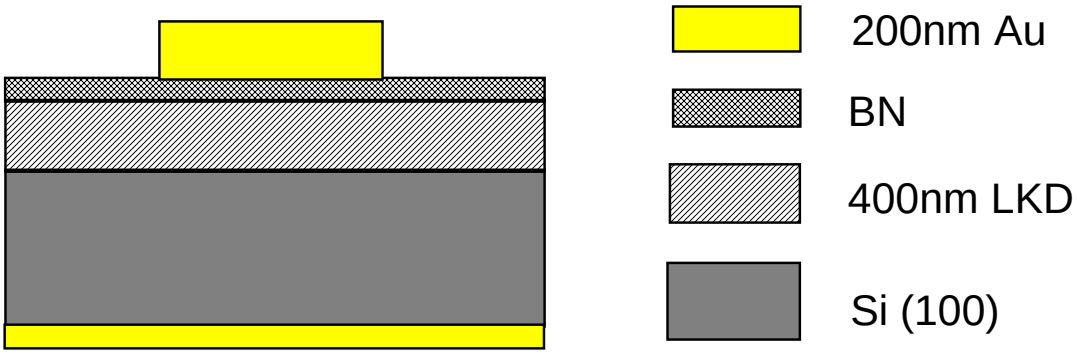

Figure 5.1. Metal-Insulator-Semiconductor structure for C-V measurement.

To evaluate the diffusion barrier against copper, 150 nm Cu was deposited on the BN by sputtering and the composite film was annealed at 400 ^{o}C for 1 hour in N_2 ambient. Time-of-flight SIMS (Tof-SIMS) was employed to estimate the barrier performance of the BN against copper diffusion.

BN thin films have been patterned for trench delineation to demonstrate the compatibility in damascene integration schemes. Photo resist (AZ5214) with a thickness of 1.4 μm was spun coated on BN films, followed by hard-contact photolithography for 15 s and photo resist development in AZ developer (diluted 2 times by deionized water) for 60 s. By using reactive ion etch system, BN films were etched and thereafter were put in acetone for about 5-minute ultrasonic clean process, which was to strip photo resist and clean etching residue.

5.3. Results and Discussion

The adhesion properties of BN deposited on the LKD film at 250^{o}C and 300^{o}C are quite poor due to the absorption of water and O_2 at the interface, so deposition at a higher substrate temperature is required. Prior to that, we applied FTIR and C-V studies to investigate the high temperature limits for the processing of LKD to identify an appropriate temperature window for the deposition of BN. As indicated by the FTIR and CV results, at temperatures below 600^{o}C, the bonding in the films remains relatively stable. Therefore so long as the processing temperatures are maintained below 500^{o}C, the bonding in the LKD film can withstand the thermal stress.

5.3.1. Structural and compositional characterization

First, we consider the BN films deposited by microwave plasma enhanced chemical vapor deposition (MWPECVD) on LKD at 400 ºC. The changes in bonding of the LKD after BN deposition are investigated by Raman and FTIR spectroscopies. According to figure 5.2, the Raman spectrum of LKD as-received featured two strong absorption peaks at 2916cm^{-1} and 2976cm^{-1} which are attributed to C-H stretching in CH_3. The decay in the intensities of these two peaks after plasma treatment, possibly due to etching, has been observed to signify a change in the physical properties, i.e. an increase in the dielectric constant of the films, which is undesirable. Therefore the correct deposition conditions have to be identified to prevent a depletion of the C-H signals.

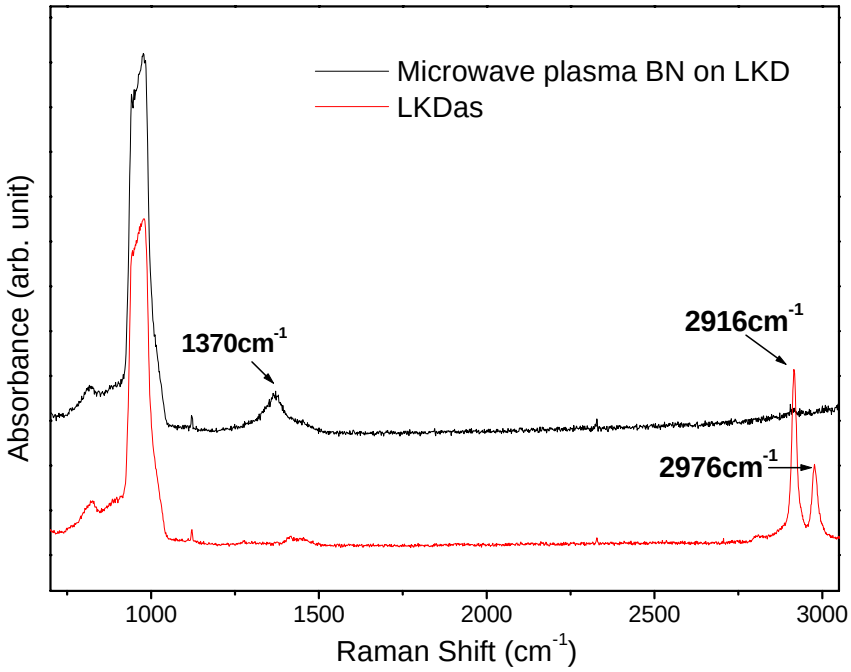

Figure 5.2. Raman spectrum of as-received LKD film and the low-k film after microwave CVD BN deposited on it at 400°C.

After BN deposition using MWPECVD, a new peak at 1370 cm^{-1} assignable to the E2g phonon modes of hexagonal BN (*h*-BN) can be seen, as shown in Fig 5.2. We found that the conditions inherent in the MWPECVD system are not suitable for the processing of the LKD films, ion damage and sputtering inevitably results in a depletion of the C-H related after BN deposition, as shown by the Raman data in Figure 5.2. Therefore we attempted the deposition using the remote discharged RF atom beam source in high vacuum conditions. We found that the RF atom beam deposition only caused a partial reduction in these C-H signals, indicating a smaller degree of collateral damage.

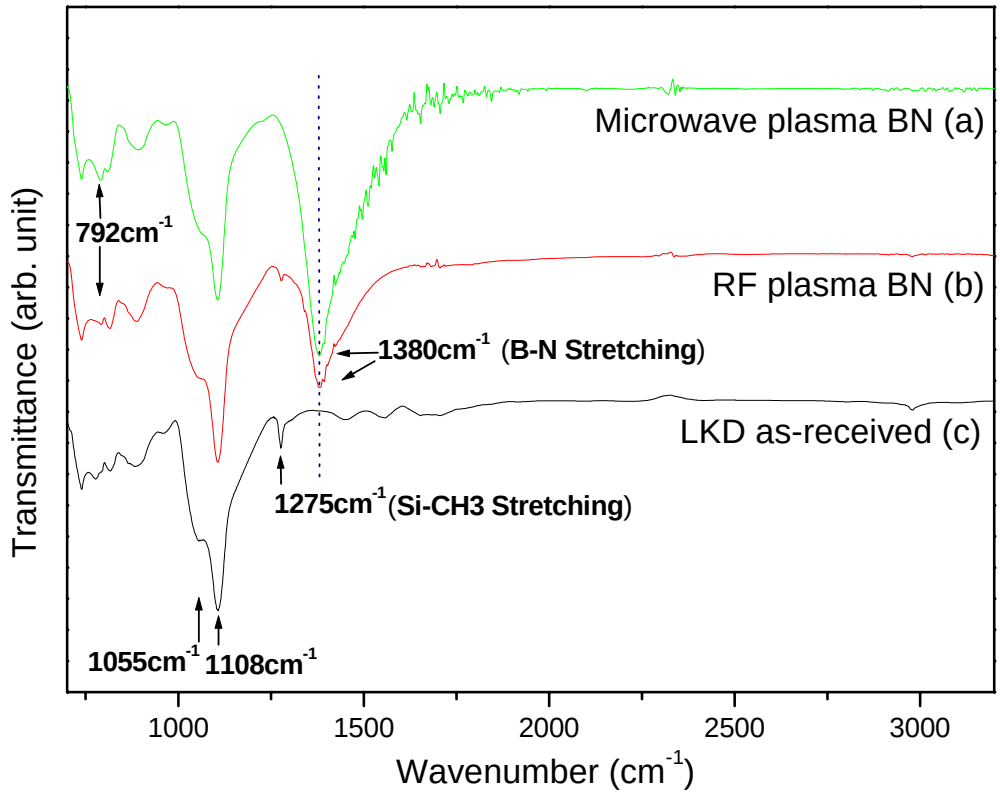

Figure 5.3. FTIR spectrum of as-received LKD, microwave plasma CVD deposited BN on low-*k* film and RF plasma deposited BN on low-k material at 400^{o}C.

Another method to evaluate the degree of plasma-induced damage can be judged from the transmission FTIR study of the films shown in Fig. 5.3. The hexagonal B-N stretching featured a strong absorption band at 1380cm^{-1} and the B-N-B bending mode featured a weaker band at 792cm^{-1} [66]. The peak at 1275cm^{-1} is attributed to Si-CH_3 stretching [56], the peak at 1108cm^{-1} is assigned to large angle Si-O-Si bonds in a cage structure and the peak at 1055cm^{-1} is assigned to the stretching of smaller Si-O-Si bonds in a network structure [55, 56]. The peak at 1275 cm^{-1} due to Si-CH3 stretching on the LKD film is entirely attenuated after MWPECVD treatment in Fig 5.3 (a), but is slightly reduced for samples treated by the RF atom beam source in Fig 5.3 (b).

SIMS was applied to investigate the changes in elemental profile following the plasma deposition of BN on the LKD. The SIMS depth profiles are plotted in figure 5.4, 5.5 and 5.6 for as-received LKD film, BN films grown by MWPECVD and RF atom beam deposition, respectively.

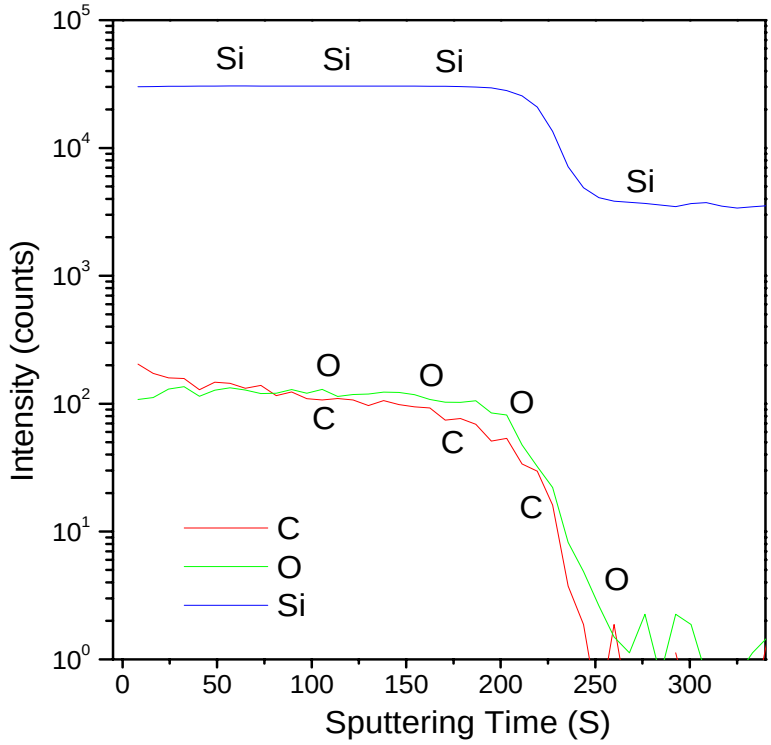

Figure 5.4. SIMS depth profile of as-received LKD film.

According to figure 5.5 and 5.6, BN layers are observable on the surface of LKD films with small amount of O atoms incorporated into this BN layer, which may be induced by the apparatus without load-lock system. The carbon depletion occurred during the BN deposition process in MWPECVD. Comparing the SIMS depth profiles, we can see that the carbon concentration of LKD film was totally depleted after BN growth using MWPECVD for about 4 mins. The high energy microwave plasma probably bombarded not only the surface of LKD film but also the material several

hundred nanometers beneath after diffused through the pores on the surface and thus probably decomposed most of the Si-CH_3 bonds in porous films, inducing the serious carbon depletion.

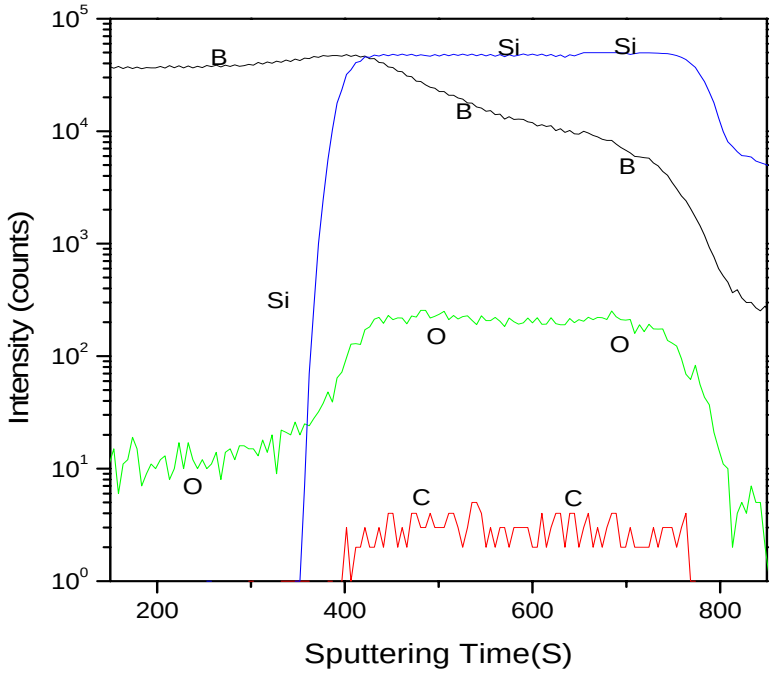

Figure 5.5. SIMS depth profile of microwave plasma CVD deposited BN on LKD film at 400°C.

In addition, there is observable boron diffusion into the nanoporous films. Boron incorporation could occur by implantation through open pores in the nanoporous films. The concentration of boron in the LKD film after MWPECVD treatment, compared to RF plasma beam treatment, is at least an order higher. This suggests that boron implantation in the nanoporous matrix occurs for the MWPECVD system due to its higher density of energetic ions. In contrast, the RF atom beam source supplies predominantly neutral fluxes with low incident energies, thus processes due to ion

implantation and ion beam-induced damage are reduced.

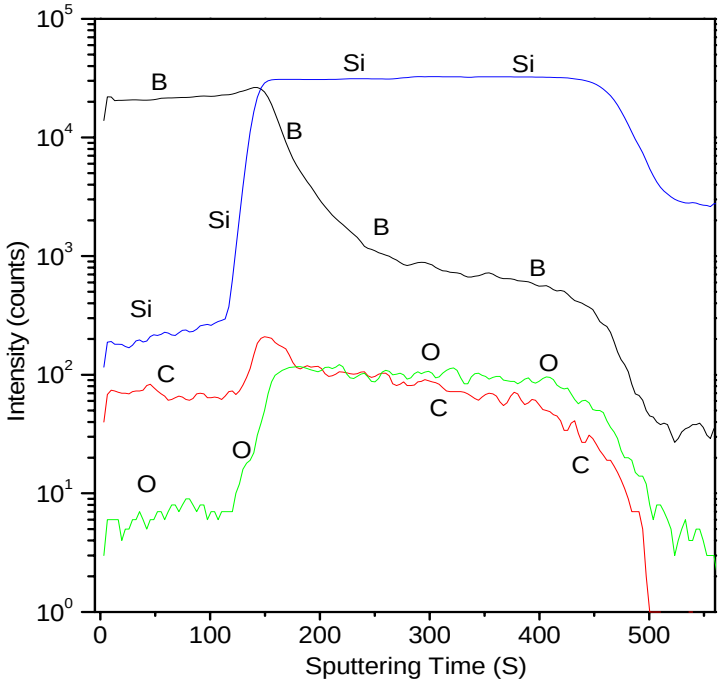

Figure 5.6. SIMS depth profile of RF plasma CVD deposited BN on LKD film at 400°C.

5.3.2. Electrical Measurement

The dielectric constants of metal-insulator-semiconductor structure fabricated from MWPECVD-deposited BN on p-type Si (100), MWPECVD-deposited BN on LKD film and RF plasma-deposited BN on LKD film are shown in Fig. 5.7. The effective *k* value is obtained from $\varepsilon_r = C_{OX}T_{OX}/A\ \varepsilon_0$, where ε_r is the relative dielectric constant (k) at 300 K, A refers to the area of the electrode of the MIS structure and T_{OX} represents thickness of the insulator. Effective *k* values of the three films are shown in Figure 5.7. The *k* values of MWPECVD-deposited BN on Si is 2.2,

MWPECVD-deposited BN on LKD is 5.0 and RF atom beam-deposited BN on LKD is 2.4. Although the *k* value of MW-deposited BN film was measured to be only 2.2 on silicon, when the BN film was integrated with LKD using MWPECVD, ion damage of the nanoporous structure resulted in an increase of the *k* value to 5. FTIR and Raman data suggested that the growth process at 500 °C probably damaged the basic porous structure of the low-*k* material. BN deposition with the RF atom beam source clearly has the benefit of introducing minimal damage to the nanoporous films and maintaining an overall low *k* value for the BN/nanoporous stack. The increase in the overall *k* value of the film for the MWPECVD process could be attributed to several reasons. One is the higher degree of etching of carbon in the nanoporous film by the higher concentration of atomic hydrogen in the plasma. The presence of CH3 in the SSQ-based nanoporous matrix is partly responsible for imparting hydrophobicities and lowering the dielectric constant of the material, and its removal by hydrogen etching creates dangling bonds which may be replaced by polar Si-OH bonds, this increases the dielectric constant [32]. High density ions in the MWPECVD system also cause boron implanation in the nanoporous films, and collapsing of the porous structures leading to structural damage.

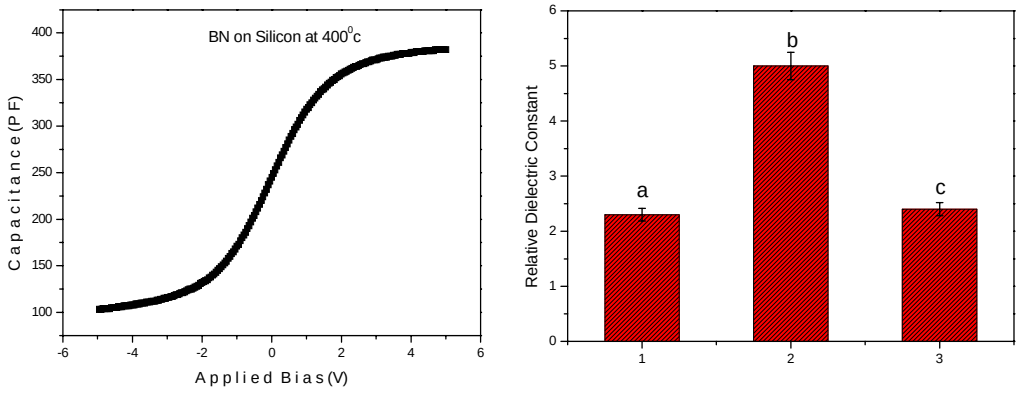

Figure 5.7. I*:* C-V curve of MPCVD BN on Si. II*:* Relative dielectric constants: a. MPCVD deposited BN on p type Si (100), b. MPCVD deposited BN on LKD film and c. RF-CVD deposited BN on LKD film.

5.3.3. Barrier Performance against Cu diffusion

To evaluate the diffusion barrier properties of BN, the multi-layered Cu/BN/LKD/Si stack was subjected to 1 hour thermal stress at 400°C. After thermal annealing, copper layer was etched by 26% $(NH_4)_2S_2O_8$ solution in advance so as to avoid the knock-on effect during SIMS characterization. The thickness of the BN was 50.0 nm. From the SIMS depth profile of the composite stack after thermal stressing, we can conclude that Cu diffusion into the porous low-k material is blocked although it has diffused into the BN with a thickness of about 13.0nm. The blockage of the diffusion may be due to amorphous structure of BN film and the presence of a 20 nm densified surface layer on the porous material, as illustrated in figure 5.9. The densification of the MSQ based nanoporous material after plasma treatment has been reported previously [32，53].

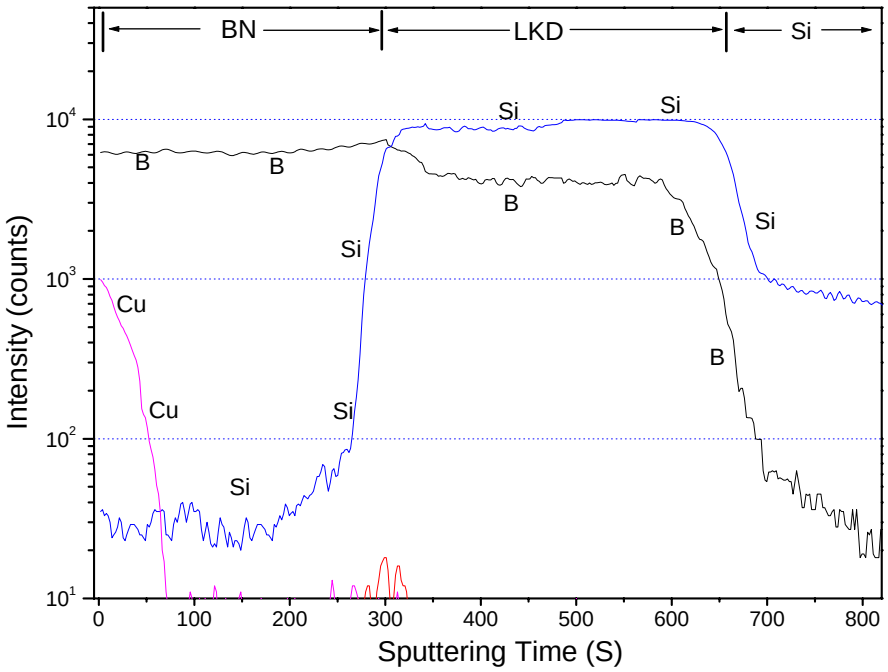

Figure 5.8. SIMS depth profile of Cu/MPCVD-BN/LKD/Si structure annealing at 400°C in N_2 ambient for 1 hour.

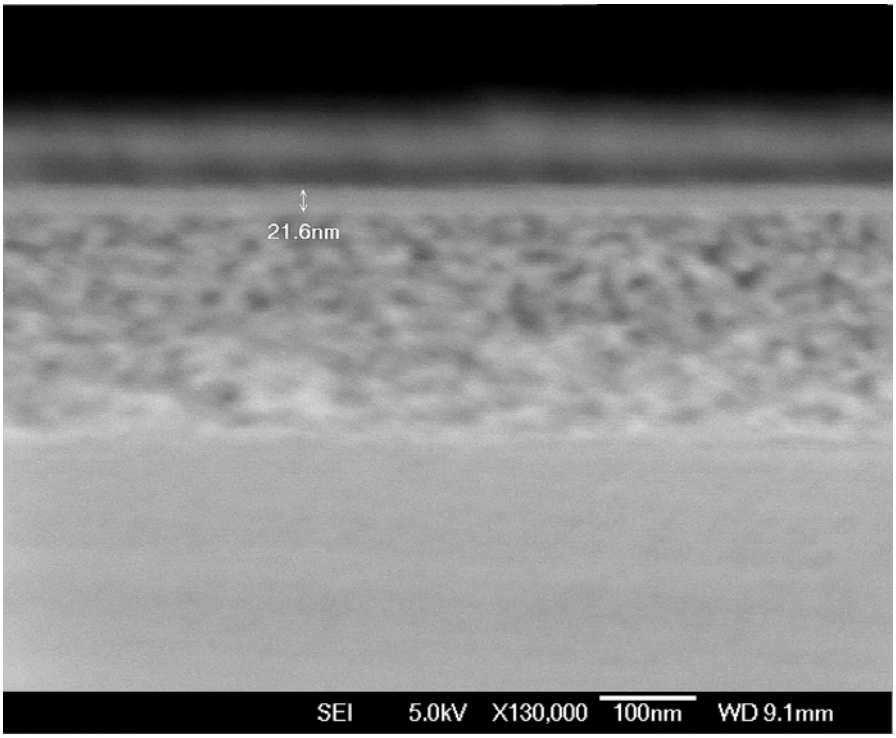

Figure 5.9. XSEM of MPCVD deposited BN on LKD at 400°C

5.3.4. BN trench patterning

To examine the process integration of the BN-nanoporous composite, we have performed trench patterning on the RF-deposited BN films and the MW-deposited $BC_{0.4}N$ films using standard photolithography steps with Argon-CF_4 as the etching gas. An etch rate of about 100 nm/min could be achieved. Figure 5.10 shows the microscope image of the BN film surface after photo resist development. As illustrated in the image, photo resist has been developed with an accurate trench width of 2 μm.

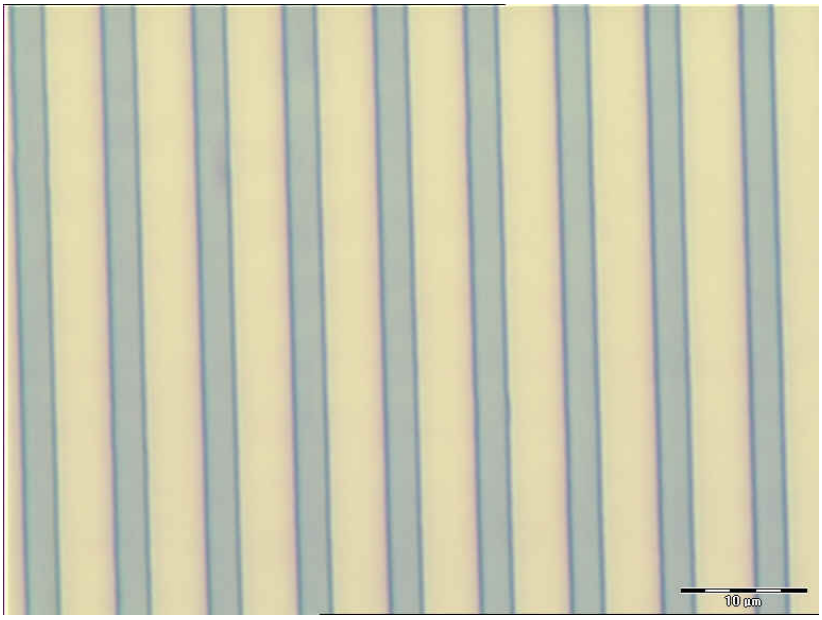

Figure 5.10. Microscope image of the surface after photo resist development.

As shown in figure 5.11, the photo resist on the thin BN film has been well developed with a thickness of about 1.4 μm. After photolithography and photo resist development, the photo resist has a very good critical dimension, with the same trench width as that of the mask. After RIE dry etching and photo resist stripping, cross-section SEM of BN film was illustrated in figure 5.12. The thin BN films have

been successfully etched and cleaned with no obvious polymer residue after the whole process, which demonstrated the BN film's compatibility in back-end of line process.

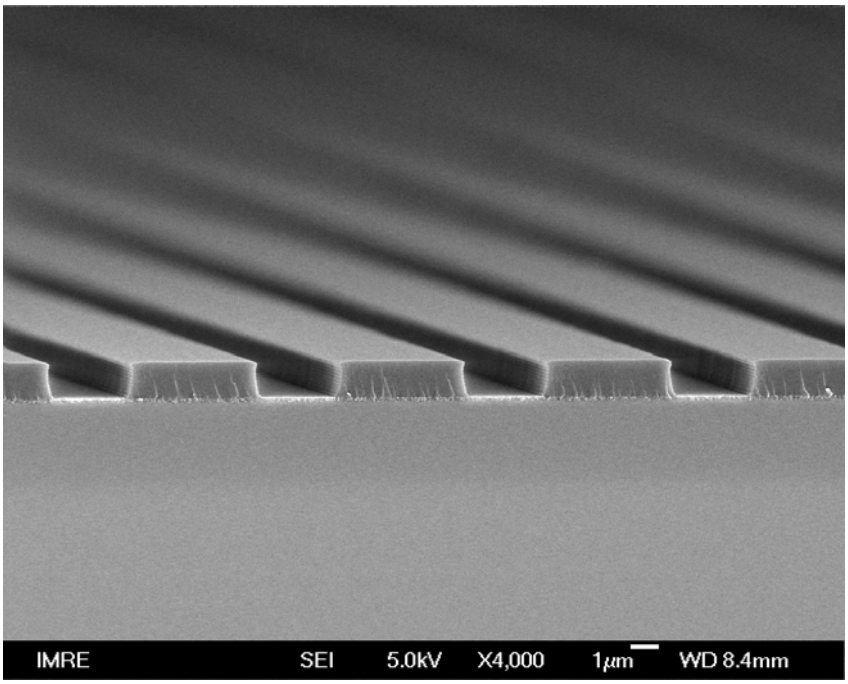

Figure 5.11. XSEM of photo resist developed on BN film.

Figure 5.12 and 5.13 also show successful trench formation on the BN film with clean vertical side wall and the absence of residual polymer resist, indicating that the BN-based material is suitable for back-end processing.

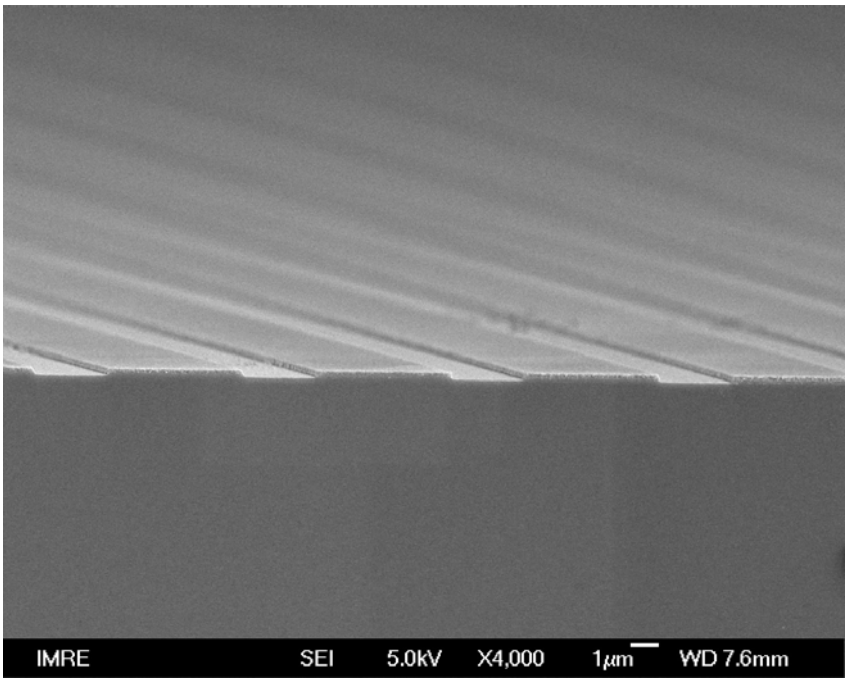

Figure 5.12. Low-Magnification XSEM of patterned BN film after photo resist stripping and residue cleaning.

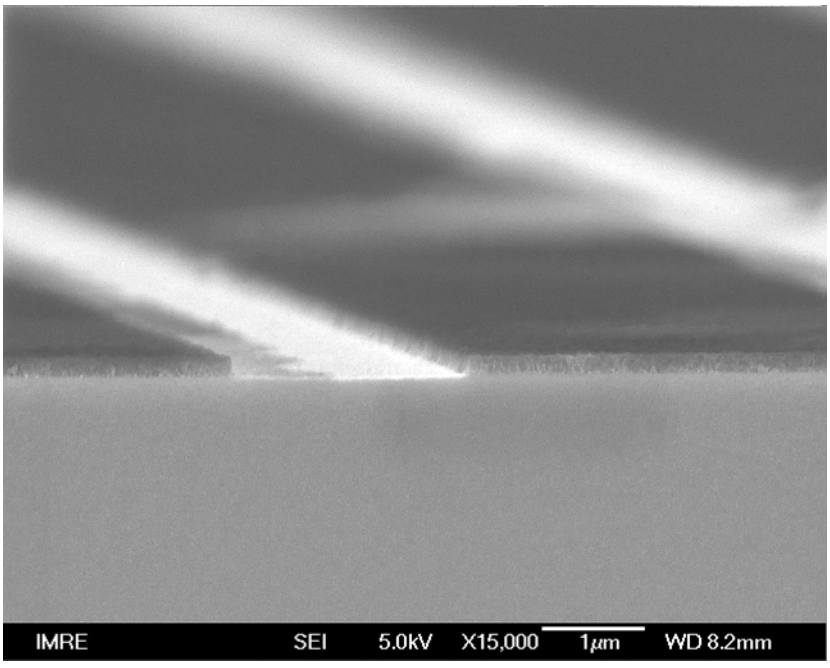

Figure 5.13. High-magnification XSEM of patterned BN film after photo resist stripping and residue cleaning.

5.4. Conclusion

We found that plasma-deposited *h*-BN films using borazine as the gas source has intrinsically low dielectric constant values (carbon impurity <1%) of between 2.2-2.4 depending on the type of plasma deposition process. The RF plasma beam-deposited *h*-BN films grown at a substrate temperature of 400 °C can integrate well with the nanoporous LKD film to form a dielectric stack with overall *k* value of 2.4. Thermal stress experiment carried out by annealing the Cu/BN/LKD/Si stack at 400 °C for one hour indicates that copper diffusion occurs in the BN film (50 nm thick), although its diffusion into the LKD is blocked. Microwave plasma deposition is not compatible with the process integration on nanoporous LKD due to the ion beam-induced damage of LKD. However, microwave plasma-deposited *h*-BN films were found to have a low *k* value of 2.2 suggesting that the *h*-BN films, or its composite, may function independently as low-*k* material.

CHAPTER 6
CONCLUSION and FUTURE WORK

In this work, both plasma treatment and thin dielectric barrier deposition have been carried out on MSQ-based porous low-*k* films to resolve some key issues in the low-*k* materials and copper damascene integration.

Two kinds of low-*k* films, Zirkon LK2200 and LKD5109, were treated by low frequency NH_3 plasma in order to form a densified surface nitridation layer. The porous low-*k* film, Zirkon LK2200, has been successfully sealed by ammonia plasma treatment with a densified skin layer of 35 nm formed on the surface after 10s of plasma treatment, which could act effectively as copper diffusion layer. The low-frequency NH_3 plasma treatment has also been found to be effective in forming a thin nitride layer on LKD5109 and substantially enhanced its resistance to copper penetration. However, beam-PALS measurement results showed that the plasma treatment can't completely seal the surface of LKD5109, which was probably due to the highly interconnected porosity distribution in the film. The unsealed structure will cause reliability issue in the back-end process. Since the plasma treatment limited capability in sealing the LKD5109 and the low-*k* property degradation after processing, low-frequency NH_3 plasma treatment is not a good method to enhance the processing capability of LKD5109 low-*k* material.

BN film was deposited on LKD5109 so as to act as dielectric barrier against Cu penetration. With an intrinsic dielectric constant of about 2.2-2.4, the RF plasma beam-deposited BN films can integrate well with the nanoporous LKD film to form a dielectric stack with overall *k* value of 2.4. Thermal stress experiment showed that copper diffusion occurs in the BN film (50 nm thick), although its diffusion into the LKD is blocked. Microwave plasma deposition is not compatible with the process integration on nanoporous LKD due to the ion beam-induced damage of the material. However, microwave plasma-deposited *h*-BN films were found to have a low *k* value of 2.2 suggesting that the *h*-BN films, or its composite (BCN), may function independently as low-*k* material.

In the future work, the sealing efficiency of NH_3 plasma treatment on patterned Zirkon LK2200 should be verified firstly. Especially we need to check the treatment performance on the sidewall of the dielectric trench and via by using beam-PALS. Secondly, the microwave plasma-deposited BN/BCN film processing compatibility with Cu should be checked to see whether or not it can be an attractive candidate as ultra low-*k* material.

NOMENCLATURE:

Low-*k* film: Low Dielectric Constant film

PT: Plasma Treatment

RC delay: Resistance Capacitance Delay

MSQ: Methyl-silsesquioxane

CVD: Chemical Vapor Deposition

PVD: Physical Vapor Deposition

DRAM: Dynamic Random Access Memory (DRAM) which is the most common kind of random access memory for personal computers and workstations

MPU: Micro Processor Unit

CMP: Chemical-Mechanical Polishing

RIE: Reactive Ion Etching

ARC: Anti-reflective Coating

PR: Photo Resist

MIS: Metal-Insulator-Silicon structure

ESL: Etch Stop Layer

Hard Mask: The layer with high mechanical integrity to protect under layer from polishing

BIBLIOGRAPHY

1. J. D. Plummer, M. D. Deal and P. B. Griffin., *Silicon VLSI Technology*, edited by Alice Dworkin, Rose Kernan and Marcia Horton., Prentice Hall, New Jersey, 1 (2000)

2. K. Maex, M.R. Baklanov, D. Shamiryan, F. lacopi, S. H. Brongersma, Z. S. Yanovitskaya., *J. Appl. Phys*., Vol. 93, No. 11, 8794 (2003)

3. *International Technology Roadmap for Semiconductors* (ITRS) of 2002

4. L. Peters., "Industry Divides on Low-k Dielectric Choices", *Semiconductor International* (2001)

5. L. Peters., IMEC Explores Interconnect, Reliability Issues Beyond 65 nm, Nov. Issue, *Semiconductor International* (2002)

6. F. Iacopi., C. Zistl., C. Jehoul., Zs. Tokei., Q.T. Le., A. Das., C. Sullivan., G. Prokopowicz., D. Gronbeck., M. Gallagher., J. Calvert., K. Maex., *Microelectron. Eng*., Vol. 64, 351 (2002)

7. T. Sugino., Y. Etou., T. Tai., H. Mori., *Appl. Phys. Lett*., Vol. 80, No. 4, 649 (2002)

8. W. W. Lee and P.S. Ho, *MRS Bulletin*, Oct., 19 (1997)

9. M. Morgan, E.T. Ryan, J.-H. Zhao, C. Hu, T. Cho and P.S. Ho, *Annu. Rev. Mater. Sci*., 30, 645 (2000)

10. B. Zhao and M. Brongo, *Mat. Res. Soc. Sypm. Proc.,* **565***,* 137 (1999)

11. J. Rouquerol, D. Avnir, C.W. Fairbridge, D.H. Everett, J.H. Haynes, N. Pernicone, J.D.F.Ramsay, K.S.W.Sing, and K.K. Unger, *Pure Appl. Chem.* 66, 1739 (1994)

12. J. Proost, E. Kondoh, G. Vereecke, M. Heyns, and K. Maex, *J. Vac. Sci. Technol. B* 16, 2091 (1998)

13. J. Proost, M. Baklanov, K. Maex, and L. Delaey, *J. Vac. Sci. Technol. B* 18, 303 (2000)

14. F. Iacopi, Zs. Tokei, M. Stucchi, S. Brongersma, D. Vanhaeren, and K. Maex,

Microelectron. Eng. 65, 123 (2003)

15. T. Furusawa, D. Ryazaki, R. Yoneyama, Y. Homma, and K. Hinode, *J. Electrochem. Soc.* 148, F175 (2001)

16. S. S. Han and B. S. Baez, *J. of. Electrochem. Soc.* 148 (4), F67 (2001)

17. S. Backaran, J. Liu, K. Domansky, N. Kohler, X. H. Li, C. Colye, G. E. Fryxell, S. Thevuthasan, R. E. Williford, *Adv. Mater.* 12, No. 4 (2000)

18. Grill, D. Edelstein, and V. Patel, *Advanced Metallization Conference 2001* (Material Research Society, Pittsburgh, PA, 2002)

19. K. Buchanan, K. Beekmann, K. Giles, J. C. Yeoh, and H. Donohue, *Advanced Metallization Conference,* Montreal, Canada, 2001

20. G. L. Link, in *Polymer Science*, edited by A. D. Jenkins (1972), p. 1283.

21. J. J. Waeterloos, Zs. Tokei, F. Iacopi, R. Caluwaerts, H. Struyf, I. Vos, and K. Maex, SEMATECH Workshop, San Francisco, CA, (2002)

22. T. Ramos, K. Roderick, A. Maskara and D. M. Smith; *Advanced Metallization and Interconnect Systems for ULSI Applications in 1996 Mater. Res. Soc., Pittsburgh,* 455 (1997 b)

23. M.-H. Jo, J.-K. Hong, H.-H. Park, J.-J. Kim and S.-H. Hyun, *Microelectronic Engineering,* **33**, 343 (1997)

24. T. A. Deis, C. Saha, E. Moyer, K. Chung, Y. Liu, M. Spaulding, J. Albaugh, W. Chen and J. Bremmer, *Mat. Res. Soc. Sypm. Proc.,* **612**. D5.18 (2000)

25. A. T. Kohl, R. Mimna, R. Shick, L. Rhodes, Z. L. Wang and P. A. Kohl, *Electrochem. Solid ST, 2,2,77 (1999)*

26. K. R. Carter, *Mat. Res. Soc. Sypm. Proc.,* **467**, 87 (1997)

27. J. L. Hedrick, R.D. Miller, C.J. Hawker, K.R. Carter, W. Volksen, D. Y. Yoon and, M. Trollsas, *Adv. Mater.*, **10**, 13, 1049 (1998)

28. H. Fan, H.R. Bentley, K.R. Kathan, P. Clem, Y. Lu and C.J. Brinker, *J. Non-Cryst. Solids*. **285**, 79 (2001)

29. J. L. Hedrick, T.P. Russel, M. Sanchez, R. DiPietro, S. Swanson, D. Jerome, R. Mecerreyes, *Macromolecules*, **29**, 3642 (1996)

30. A. Ore, Univ. Bergen Arbok, *Naturv. Rekke*, 9 (1949)

31. O. E. Mogensen, *J. Chem. Phys.*, 60, 998 (1974)

32. J. N. Sun, D. W. Gidley, Y. Hu, and W. E. Frieze, E. T. Ryan, *Appl. Phys. Lett*. Vol 81, No. 8, 1447 (2002)

33. J. N. Sun, D. W. Gidley, T. L. Dull, W. E. Frieze, A. F. Yee, E. T. Ryan, S. Lin and J. Wetzel, *J. Appl. Phys.* Vol 89, No. 9, 5138 (2001)

34. P. J. Schultz and K. G. Lynn, *Rev. Mod. Phys.,* **60**, 701 (1988)

35. S. R. Wilson, J. T. Clarence and J. L. Freeman, NOYES PUBLICATIONS, *Handbook of Multilevel Metallization for Integrated Circuits* p.8 (1993)

36. G. C. Schwartz, K.V. Srikrishman and A. Bross, *Handbook of Semiconductor Interconnection Technology*, IBM Microelectronics, published by Marcel Dekker, Inc, p.302 (1998)

37. S. Wolf, *Silicon Processing for the VLSI Era.*, 672-673 (2002)

38. R. H. Havemann and J. A. Hutchby, *Proceedings of The IEEE*, vol. 89, No. 5, May, 591 (2001)

39. B. J. Gordon, *Solid State Technology*, Jan, 57 (1993)

40. D. K. Schroder, Arizona State University, *Semiconductor Material and Device Characterization,* A Wiley-Interscience Publication, p.347 (1998)

41. L. Xie, G. B. DeMaggio, W. E. Frieze, J. DeVries, D.W. Gidley, H.A. Hristov and, A. F. Yee, *Phys. Rev. Lett.,* **74***,* 4947 (1995a)

42. F. Iacopi, Zs. Tokei, Q. T. Le, D. Shamiryan, T. Conard, B. Brijs, U. Kreissig, M. V. Hove and K. Maex, *J. Appl. Phys.* Vol. 92, No. 3, 1548 (2002)

43. H. J. Lee et al., *J. Electrochem. Soc.* Vol. 148, Issue 10, F195 (2001)

44. E. T. Ryan, J. Martin, K. Junker, J. J. Lee, T. Guenther, J. Wetzel, S. Lin, D. W. Gidley, and J. Sun, *Proceeding Of IITC*, 27 (2002)

45. D. W. Gidley, W. E. Frieze, A. F. Yee, T. L. Dull, H.-M. Ho, and E. T. Ryan, *Phys. Rev. B,* 60, R5157 (1999)

46. Y-H Kim, M. S. Hwang, H. J. Kim, J. Y. Kim and Young Lee, *J. Appl. Phys,* vol.

90, 3367 (2001)

47. A. Grill and D. A. Neumayer, *J. Appl. Phys*, vol. 94, 6697 (2003)

48. C. T. Chen and B. S. Chiou, *J. Mater. Science.* 139 (2004)

49. T. Thamm, W. Baumann, D. Dietrich, N. Meyer, S. StoE and G. Marx, *Phys. Chem. Chem. Phys*., vol. 3, 5150 (2001)

50. P. T. Liu, T. C. Chang, Y. L. Yang, Y. F. Cheng, S. M. Sze, *IEEE TRANSACTIONS ON ELECTRON DEVICES,* vol. 47, NO. 9, SEPTEMBER, 1733 (2000)

51. H. S. Sim, Y. T. Kim and H. Jeon, *Jpn. J. Appl. Phys,* vol. 41, 3658 (2002)

52. K. M. Chang, I. C. Deng, Y. P. Tsai, C. Y. Wen, S. J. Yeh, S. W. Wang, and J. Y. Wang., *J. Electrochem. Soc.* 147 (6), 2332 (2000)

53. E. T. Ryan, J. Martin, K. Junker, J. Wetzel, D. W. Gidley and J. N. Sun, *J. Mater. Res.*, Vol. 16, No. 12, 3335 (2001)

54. K. Mosig , T. Jacobs , K. Brennan , M. Rasco , J. Wolf , R. Augur, *Micro Engineering*, vol. 64, 11 (2002)

55. M. G. Albrecht and C. Blanchette, *J. Electrochem. Soc.* 145, 4019 (1998)

56. T. R. Crompton, *The Chemistry of Organic Silicon Compounds*, edited by S. Patai and Z. Rappoport (Wiley, New York), pp. 416-421 (1989)

57. L.-H. Lee, W.-C. Chen, W.-C. Liu, *J. of Polymer Science Part A: Polymer Chemistry,* vol. 40, 1560 (2002)

58. Z.-C. Wu, C.-C. Chiang, W.-H. Wu, M.-C. Chen, S.-M. Jeng, L.-J. Li, S.-M. Jang, C.-H. Yu, and M.-S. Liang, *IEEE ELECTRON DEVICE LETTERS,* vol. 22, No. 6, JUNE 263 (2001)

59. A. Das. *Microelectronic Engineering* 64 (2002) 25

60. S. V. Nguyen, T. Nguyen, H. Treichel, O. Spindler, *J. Electrochem. Soc.* 141，1633 (1994)

61. W. F. Kane, S. A. Cohen, J. P. Hummel, B. Luther, D. B. Beach, *J. Electrochem. Soc.* 144, 658 (1997)

62. T. Sugino, T. Tai, Y. Etou, *Diam. Related. Mater.* 10, 1375 (2001)

63. T. Tai, T. Sugiyama, T. Sugino, *Diam. Related. Mater.* 12, 1117 (2003)

64. T. Sugiyama, T. Tai, A. Okamoto, M Yoshitake, T. Sugino, *Diam. Related. Mater.* 12, 1113 (2003)

65. M. J. Loboda, C. M. Grove, and R. F. Schneider, *J. Electrochem. Soc.* 145, 2861 (1998)

66. T. Sugino and H. Hieda, *Diamond and Related Materials* 9, 1233 (2000)